



DI Julian Pilz, BSc

**Plasma-Enhanced Atomic Layer Deposition and
Vapor Phase Infiltration of ZnO:
From Fundamental Growth Characteristics to
Piezoelectric Films**

DOCTORAL THESIS

to achieve the university degree of
Doktor der technischen Wissenschaften

submitted to

Graz University of Technology

Supervisor

Assoc. Prof. Dr. Anna Maria Coclite

Institute of Solid State Physics

AFFIDAVIT

I declare that I have authored this thesis independently, that I have not used other than the declared sources/resources, and that I have explicitly indicated all material which has been quoted either literally or by content from the sources used. The text document uploaded to TUGRAZonline is identical to the present doctoral thesis.

Date

Signature

Plasma-Enhanced Atomic Layer Deposition and Vapor Phase Infiltration of ZnO: From Fundamental Growth Characteristics to Piezoelectric Films

ABSTRACT

In this thesis, the growth of the semiconducting material ZnO by two methods - plasma-enhanced atomic layer deposition and vapor phase infiltration - is investigated. As ZnO is utilized in diverse applications such as UV-protection, gas sensors, or piezoelectrics, precise knowledge about the characteristics of the growth process is needed to obtain the desired properties for a specific application. Plasma-enhanced atomic layer deposition (PE-ALD) is a thin film technique which can deposit uniform and conformal films with high thickness control at low temperatures. The presented studies show that PE-ALD is able to deposit ZnO with small amount of impurities as low as room temperature. Furthermore, by variation of the substrate temperature, ideal temperature regions for specific applications and the relationship between growth and resulting properties could be identified. In the beginning of the deposition, deviations from the ideal growth occur, which are identified as substrate-enhanced island growth. The formation of crystallites is found to occur after this initial growth period. The obtained knowledge about these growth characteristics is furthermore applied to piezoelectric devices. The piezoresponse of ZnO, sandwiched between electrodes, is hereby studied on both flexible and rigid substrates with a combination of macroscopic and scanning probe techniques. Vapor phase infiltration (VPI) is a technique for transforming polymers into hybrid organic/inorganic materials. It often uses the same precursors as ALD but instead of growing a thin film on a substrate, the polymer free volume is infiltrated with the precursors. In the thesis, the successful infiltration of ZnO into polyisoprene is presented. Polyisoprene is an elastomeric polymer, a class of polymers which has not been widely studied as a substrate for VPI. The infiltration kinetics and the chemical mechanisms of this system are presented and it is shown that pre-heating of the polymer largely affects these due to changes in thickness and chemical structure. Concluding, the thesis gives fundamental insights into the growth characteristics for a future application of ZnO thin films or polymer/ZnO hybrids in diverse fields as well as a demonstration of ZnO in a piezoelectric device.

Plasmagestützte Atomlagenabscheidung und Gasphaseninfiltration von ZnO: von grundlegenden Wachstumscharakteristika zu piezoelektrischen Filmen

KURZFASSUNG

In dieser Arbeit wird das Wachstum des halbleitenden Materials ZnO anhand von zwei Methoden - plasmagestützte Atomlagenabscheidung und Gasphaseninfiltration - untersucht. Da ZnO in verschiedenen Anwendungen wie UV-Schutz, Gassensoren, oder als piezoelektrisches Element genutzt wird, ist ein genaues Wissen über die Charakteristika des Wachstumsprozess nötig um die erwünschten Eigenschaften für eine spezifische Anwendung zu erreichen. Plasmagestützte Atomlagenabscheidung (PE-ALD) ist eine Dünnschichttechnik die uniforme und konforme Filme mit genauer Dickenkontrolle bei niedriger Temperatur abscheiden kann. Die vorgelegten Studien zeigen, dass PE-ALD ZnO mit wenig Verunreinigungen sogar bei Raumtemperatur abscheiden kann. Darüber hinaus wird gezeigt, dass eine Variation der Substrattemperatur es ermöglicht, ideale Temperaturzonen für spezifische Anwendungen sowie das Verhältnis zwischen Wachstum und resultieren Eigenschaften zu identifizieren. Am Beginn der Abscheidung weicht das Wachstum vom idealen Verhalten ab, dieses anfängliche Verhalten wurde als substratbeschleunigtes Inselwachstum identifiziert. Kristallite formieren sich nach diesem anfänglichen Wachstum. Das erlangte Wissen über die Wachstumscharakteristika werden darüber hinaus für piezoelektrische Einheiten angewendet. Hierbei wird das piezoelektrische Ansprechverhalten von ZnO (auf flexiblen und starren Substraten und zwischen zwei Elektroden übereinandergeschichtet) mithilfe von makroskopischen und Rastersondentechniken untersucht. Gasphaseninfiltration (VPI) ist eine Technik zur Transformation von Polymeren in organisch/anorganische Materialien. Es benutzt oft die gleichen Ausgangsstoffe wie ALD, aber, anstatt eine Dünnschicht auf einem Substrat abzuschneiden, wird hier das freie Volumen des Polymers mit den Ausgangsstoffen infiltriert. In dieser Arbeit wird die erfolgreiche Infiltration von ZnO in Polyisopren präsentiert. Polyisopren ist ein Elastomer, und diese Klasse von Polymeren ist bisher noch nicht weitgehend untersucht worden als Substrat für VPI. Die Kinetiken und chemischen Mechanismen der Infiltration dieses Systems werden präsentiert und es wird gezeigt, dass Erhitzen des

Polymers vor der Infiltration einen Einfluss auf diese hat wegen Änderungen in der Dicke und der chemischen Struktur des Polymers. Zusammenfassend gibt die Arbeit grundsätzliche Einblicke in die Wachstumscharakteristika für zukünftige Anwendungen von ZnO-Dünnschichten und Polymer/ZnO-Hybride in diversen Bereichen und eine Demonstration wie ZnO in einem piezoelektrischen Element eingesetzt wird.

Contents

| | | |
|----------|--|----------|
| 1 | INTRODUCTION | I |
| I | Fundamentals and Methods | 5 |
| 2 | FUNDAMENTALS | 7 |
| 2.1 | General aspects of thin film technology | 7 |
| 2.2 | Atomic layer deposition | 9 |
| 2.2.1 | Principles | 9 |
| 2.2.2 | Growth per cycle | 10 |
| 2.2.3 | Adsorption | 13 |
| 2.2.4 | Growth modes | 16 |
| 2.2.5 | Plasma-enhanced atomic layer deposition | 18 |
| 2.2.6 | Materials | 21 |
| 2.2.7 | Properties and applications of ALD | 21 |
| 2.3 | Vapor phase infiltration | 24 |
| 2.3.1 | Principles | 24 |
| 2.3.2 | Properties affecting process kinetics | 29 |
| 2.3.3 | Applications for VPI | 31 |
| 2.4 | Properties and applications of ZnO | 32 |
| 2.4.1 | Growth | 33 |
| 2.4.2 | Electrical and optical properties | 33 |
| 2.4.3 | Piezoelectric properties | 34 |
| 3 | EXPERIMENTAL SETUP | 37 |
| 3.1 | Reactor design for plasma-enhanced atomic layer deposition | 37 |
| 3.2 | Reactor design for vapor phase infiltration | 38 |
| 3.3 | Universal software for the real-time control of sequential processing techniques | 40 |
| 3.3.1 | Preface | 40 |
| 3.3.2 | Introduction | 40 |
| 3.3.3 | Concept, Setup, and Graphical User Interface | 42 |
| 3.3.4 | Arduino Firmware | 46 |
| 3.3.5 | Summary and Conclusions | 49 |
| 3.3.6 | Acknowledgments | 49 |

| | | |
|--|--|-----------|
| 4 | THIN FILM ANALYSIS | 53 |
| 4.1 | Spectroscopic ellipsometry | 53 |
| 4.2 | X-ray diffraction | 55 |
| 4.2.1 | Grazing incidence X-ray diffraction | 55 |
| 4.3 | X-ray reflectivity | 56 |
| 4.4 | Piezoelectric characterization | 57 |
| 4.4.1 | Piezoresponse force microscopy | 57 |
| 4.4.2 | Macroscopic characterization | 59 |
| II Plasma-Enhanced Atomic Layer Deposition of ZnO | | 61 |
| 5 | TUNING OF MATERIAL PROPERTIES OF ZnO THIN FILMS GROWN BY PLASMA- ENHANCED ATOMIC LAYER DEPOSITION AT ROOM TEMPERATURE | 63 |
| 5.1 | Preface | 63 |
| 5.2 | Abstract | 64 |
| 5.3 | Introduction | 64 |
| 5.4 | Experiment | 66 |
| 5.5 | Results and Discussion | 68 |
| 5.5.1 | Determination of saturation regimes | 68 |
| 5.5.2 | Tuning of structural and optical properties by RF-power | 74 |
| 5.6 | Summary and Conclusions | 77 |
| 5.7 | Acknowledgments | 78 |
| 5.8 | Supporting Information | 78 |
| 6 | ZnO THIN FILMS GROWN BY PLASMA-ENHANCED ATOMIC LAYER DEPOSI- TION: MATERIAL PROPERTIES WITHIN AND OUTSIDE THE “ATOMIC LAYER DEPOSITION WINDOW” | 81 |
| 6.1 | Preface | 81 |
| 6.2 | Abstract | 82 |
| 6.3 | Introduction | 82 |
| 6.4 | Experiment | 84 |
| 6.5 | Results and Discussion | 86 |
| 6.6 | Conclusion | 95 |
| 6.7 | Acknowledgments | 96 |
| 6.8 | Supporting Information | 96 |
| 7 | INITIAL GROWTH AND CRYSTALLIZATION ONSET OF PLASMA ENHANCED- ATOMIC LAYER DEPOSITED ZnO | 99 |
| 7.1 | Preface | 99 |
| 7.2 | Abstract | 100 |

| | | |
|------------|--|------------|
| 7.3 | Introduction | 100 |
| 7.4 | Experiment | 102 |
| 7.5 | Results and Discussion | 104 |
| 7.5.1 | Thickness and Morphology | 104 |
| 7.5.2 | Development of Crystallites | 110 |
| 7.5.3 | Crystallization at High Temperature | 113 |
| 7.6 | Conclusions | 114 |
| 7.7 | Acknowledgments | 114 |
| 8 | PIEZOELECTRIC PROPERTIES OF ZINC OXIDE THIN FILMS GROWN BY PLASMA- ENHANCED ATOMIC LAYER DEPOSITION | 115 |
| 8.1 | Preface | 115 |
| 8.2 | Abstract | 116 |
| 8.3 | Introduction | 116 |
| 8.4 | Results | 117 |
| 8.5 | Conclusion | 122 |
| 8.6 | Experimental | 122 |
| 8.7 | Acknowledgements | 123 |
| III | Vapor Phase Infiltration of ZnO | 125 |
| 9 | VAPOR PHASE INFILTRATION OF ZnO INTO THIN FILMS OF CIS-POLYISOPRENE (NATURAL RUBBER) | 127 |
| 9.1 | Preface | 127 |
| 9.2 | Abstract | 127 |
| 9.3 | Introduction | 128 |
| 9.4 | Experimental | 130 |
| 9.5 | Results and discussion | 131 |
| 9.5.1 | Demonstration of DEZ + H ₂ O VPI in cis-polyisoprene | 131 |
| 9.5.2 | Pre-heating of polyisoprene films | 132 |
| 9.5.3 | Quantifying inorganic loading | 133 |
| 9.5.4 | Kinetics of Zinc Oxide infiltration into cis-polyisoprene | 135 |
| 9.5.5 | Entrapment of DEZ precursor in cis-polyisoprene | 137 |
| 9.5.6 | Dissolution of ZnO-polyisoprene hybrid films | 142 |
| 9.6 | Conclusions | 143 |
| 9.7 | Acknowledgements | 145 |
| 9.8 | Supporting Information | 146 |
| 9.8.1 | Diffusion kinetics | 146 |
| 10 | CONCLUSIONS AND OUTLOOK | 149 |

Acknowledgments

I am grateful for these three years of PhD studies, for the mix of experimental work, analytical thinking, writing, and presentations, for all the people I met along the way, and for lunches at Cafe Zapo.

I want to thank my supervisor Anna Maria Coclite for her support and open doors throughout this thesis, for guidance and enabling personal development in many areas, and for providing such an enjoyable work atmosphere in the group. I am grateful for sharing the office with Katrin Unger, Marianne Kräuter, Richard Berger, (Habibi) Taher Abu Ali, and for the former group members Paul Christian, Martin Tazreiter, and Alberto (Bertl) Perrotta for great collaborations, their help in experimental work, and for good conversations and chocolate salami. And I am especially thankful for my great friend and Kollegen Fabian Muralter for all this fun time together. I also want to thank other people from the Institute of Solid State Physics, Roland Resel and his group for X-ray discussions, Günther Leising for discussions on optical measurements, and Harald Kerschbaumer and Martin Kornschober for their great help in the lab. Furthermore, the collaborations with colleagues from Montanuniversität Leoben, especially Markus Kratzer, and Joanneum Research are greatly acknowledged.

I am also very thankful that Mark Losego hosted me for half a year in his lab at Georgia Tech and his great hospitality, from showing me over the top Halloween decoration to Thanksgiving turkey. Jamie Wooding, Emily McGuinness, Yi Li, Shawn Gregory, Simon Willis, Shuaib Balogun and all undergraduates gave me a warm welcome and were very helpful in all the lab-work and also friends off-campus. I am grateful for the great time in the US and the funding by the Marshallplan foundation.

And I am thankful for my parents and family for all their support and love.

Soli Deo Gloria.

1

Introduction

Zinc oxide (ZnO) is a semiconducting material with electrical, optical, and piezoelectric properties which are interesting for a plethora of applications. For example, its industrial usage spans from vulcanizing activators in rubber manufacturing, wound healing, UV-absorbing, and non-toxic additives in the cosmetics and medical industry, to catalysts in the chemical industry.¹ Emerging applications utilize ZnO in gas sensors, transparent conductive oxides, or piezoelectric nanogenerators.^{2,3} Especially for these emerging applications, the growth of ZnO has to be finely optimized to achieve the desired properties.

Within this thesis, the growth of ZnO by two techniques is investigated - atomic layer deposition and vapor phase infiltration. Atomic layer deposition (ALD) is a vapor-phase technique to produce uniform and conformal thin films on a substrate.⁴ Due to its self-limiting and sequential process to introduce reactants, the thickness is digitally controlled by deposition cycles, with a growth per cycle in the Å/cycle range. This allows for an extraordinary thickness control. These process characteristics of ALD are utilized e.g. in the microelectronics industry for the deposition of gate oxides.⁵ In the experiments of this thesis, plasma-enhanced atomic layer deposition (PE-ALD) is applied, a variant of ALD in which reactive plasma species are used as the co-reactant.⁶ The use of plasma in the process allows for enhanced properties and lower deposition temperatures. Vapor phase infiltration (VPI) is also a vapor-phase technique which often applies the same reactants as ALD.⁷ However, its purpose is fundamentally different to ALD. While ALD deposits a thin film on a substrate, VPI intends to infiltrate a polymeric substrate with reactants and transform it into an or-

ganic/inorganic hybrid material. The hybrid material often shows enhanced properties (e.g. mechanical stability) without losing the inherent properties of the polymer such as flexibility. This thesis aims to shed light on the fundamental process characteristics of ZnO deposition by these two techniques and investigate how different process parameters affect the material properties.

The thesis is divided into three parts. In part I, the fundamentals of atomic layer deposition and vapor phase infiltration are presented in detail and some of the ZnO properties are discussed. A description of the reactors for ALD and VPI and of the software to control the ALD process is given. The part concludes with the fundamentals of some of the characterization techniques used to analyze the ZnO films.

Part II deals with different studies on plasma-enhanced atomic layer deposition of ZnO. First, the growth of ZnO at room temperature is investigated. Such a low deposition temperature is especially interesting for thermo-sensitive substrates. In the study, the ALD growth is first optimized with respect to reactant doses and purge times and the ZnO films are analyzed with respect to their composition, and crystalline and optical properties. Furthermore, the effect of the plasma power on these properties is investigated. The next study deals with the effect of substrate temperature on the growth characteristics and properties of ZnO. Crystalline, optical, electrical, and structural properties of ZnO are investigated and linked to regions where the temperature dependence of the growth per cycle shows distinct features. The first cycles of an ALD process often show deviations from the steady-state regime, in which the growth per cycle is constant with the number of deposition cycles. Knowledge about this initial growth regime is fundamental for the application of ultrathin films. In the study, the thickness and morphology of the ZnO films is monitored with respect to the number of cycles to identify growth regimes and synchrotron radiation experiments are used to identify the onset of crystallization. In the last study of part II, the piezoelectric properties of ZnO thin films are investigated. The influence of the substrate (rigid or flexible) and the deposition temperature are parameters in the study and the piezoelectric characterization is performed by macroscopic and scanning probe techniques. Furthermore, the link between the piezoelectric response and the crystalline orientation is presented. These studies on PE-ALD of ZnO give new insights into low-temperature growth, temperature-dependent and cycle-dependent growth regimes, and piezoelectric properties of these films.

Part III deals with the vapor phase infiltration of ZnO into cis-polyisoprene. Polyisoprene presents an important class of elastomeric polymers which have not been widely investigated for that purpose. The kinetics and chemical mechanisms of the infiltration are presented

and the dissolution stability of the hybrid material tested as an example for the enhanced properties of the polymer after infiltration.

Part I

Fundamentals and Methods

2

Fundamentals

2.1 GENERAL ASPECTS OF THIN FILM TECHNOLOGY

Thin films of materials on bulk materials (i.e. substrates) have diverse functionalities which are not easily achievable merely in the substrate.⁸ As such, thin films can serve as reflective coatings (e.g. mirrors), as electrical insulating layers, as corrosion protection, as wear-resistant coatings, and many more. In these applications, the optical, electrical, chemical, and mechanical properties of certain materials are utilized. In contrast to thick film technology (e.g. painting or silk screening), where the building blocks are nano- or microparticles, the building blocks are individual molecules in thin film technology. Thin film processes thus allow for enhanced control and quality of the material.

A thin film process consists of the following sequential steps:⁸

1. *Providing the source material*: the source, from which the thin film is formed, may be a solid, liquid, vapor, or gas. Solid sources need to be vaporized in order to transport the material to the substrate. This can be done by heat, electrons, ions, etc.
2. *Transport*: the transport of the source material dictates the uniformity of arriving species on the substrate. The transport is influenced by the transport medium which can be a high/ultrahigh vacuum, a fluid, or a plasma. While molecules in a vacuum travel in straight lines from the source to the substrate, collisions appear when molecules travel through a fluid. The uniformity of the source molecules transported through a vacuum is thus governed by the geometry whereas it depends on gas flow patterns and

diffusion through other gas species when the transport happens in a fluid. Plasmas as a transport medium can provide energy for processes at low temperatures.

3. *Deposition*: the actual deposition of the material onto the substrate depends on the substrate condition, the reactivity of the source material and the energy input. The condition of the substrate surface includes the roughness, number of reactive groups, crystallographic parameters, and eventual surface contaminants. The probability that an arriving molecule reacts with the surface is called sticking coefficient. For conformal coating, a low sticking coefficient is desired. The energy input to the substrate is often-times provided through heat and it affects the reactivity of the arriving molecules and the structure and composition of the resulting thin film. Other energy inputs include photons and positive ion bombardment (typically present in plasmas).
4. (*Annealing*): annealing is an optional step in which material properties are modified *after* the deposition by typically thermal treatments.
5. *Analysis*: in the last step, the properties of the obtained thin film are analyzed. In case the desired properties have not been achieved by the process, parameters of the source, transport, and deposition have to be adopted to meet the requirements.

Thin film processes can be generally categorized into *physical* and *chemical vapor deposition* (PVD and CVD). These processes differ in the source and the transport and deposition mechanisms.^{8,9} In PVD, the source is typically a solid which is vaporized by heat or energetic beams of electrons, photons or ions. The transport often happens in a reduced pressure environment and there is a lack of chemical reactions in the gas phase or at the substrate surface. Typical examples of PVD processes are evaporation, laser ablation, or sputtering. In CVD, gases or vapors are used as a source and the transport happens typically in a fluid-regime. Reactions can happen in the gas phase (homogeneous) or on the substrate surface (heterogeneous). CVD processes can be further classified with respect to their reaction mechanisms. Sub-classes of CVD include thermal CVD, plasma-enhanced CVD, and initiated CVD.^{9,10}

The investigated processes in this thesis, atomic layer deposition (ALD) and vapor phase infiltration (VPI), are closely related to CVD. The characteristics of ALD rely however on the *sequential* introduction of precursors in contrast to a *continuous* introduction of precursors in CVD.⁴ VPI on the other hand uses similar process schemes as ALD, however does not result in a thin film grown *on* a surface but an introduction of material *into* the bulk of the substrate. Leng and Losego⁷ thus proposed a taxonomy in which CVD, ALD, and VPI are the main classes of *chemical vapor processing* techniques, with the respective sub-classes differing in their processing conditions (e.g. plasma-enhanced).

2.2 ATOMIC LAYER DEPOSITION

Atomic layer deposition (ALD) is a thin film deposition technique whose basic principles were proposed in the Soviet Union as early as the 1950s and 1960s.¹¹ The implementation as a deposition technique was developed in Finland in the 1970s by Suntola et al. The main purpose at that time was to deposit high quality films for electroluminescent displays and, due to the fact that the films were deposited in an epitaxial manner, the technique was called atomic layer epitaxy. The interest in the technique both by research and industry increased in the 1990s and 2000s as the semiconductor industry was aiming to scale down devices and needed a technique to deposit thin, conformal films with accurate control of film thickness and composition. Today, the use of ALD in, e.g., the deposition of gate dielectrics is an industry standard and the application space of ALD and its derivatives expanded to other areas.

2.2.1 PRINCIPLES

Atomic layer deposition (ALD) is a vapor based technique which relies on the repetition of self-limiting surface reactions. In the simplest case, e.g. binary compounds such as Al_2O_3 or ZnO , this is done by exposing the substrate to two reactants (often called precursor and co-reactant). To assure an ALD behavior, the reactant molecules must react only with surface species produced by the other reactant and not with itself, the other reactant, or by-products in the gas phase. To avoid reactions of the two reactants in the gas phase, purging steps are introduced in-between the reactant exposures. This is typically done by pumping the reaction chamber and flushing with inert gases such as Ar or N_2 . Figure 2.1 shows a simplified sketch of an ALD cycle for a ZnO process. In this sketch, diethylzinc (DEZ, $\text{Zn}(\text{C}_2\text{H}_5)_2$) and water (H_2O) are used as the precursor and co-reactant, respectively. Furthermore, the substrate surface is assumed to be fully hydroxylated.

Starting from the top left image, the substrate is exposed to DEZ. The DEZ molecules react with the surface hydroxy groups and after completion (i.e. there are no more active surface groups), DEZ and the by-products from the reaction with the hydroxy groups are purged with an inert gas. Once the reactor is empty, the new surface species are exposed to water and again, after all the reactions are complete, water and the by-products are removed from the reactor through purging. By performing the depicted 4 steps, which we call an ALD cycle, we thus formed a monolayer (ML) of ZnO with the same surface species as in the beginning. Thus we can repeat this cycle until the desired thickness of the film is achieved.

The complete chemical reaction of this ALD cycle is¹²

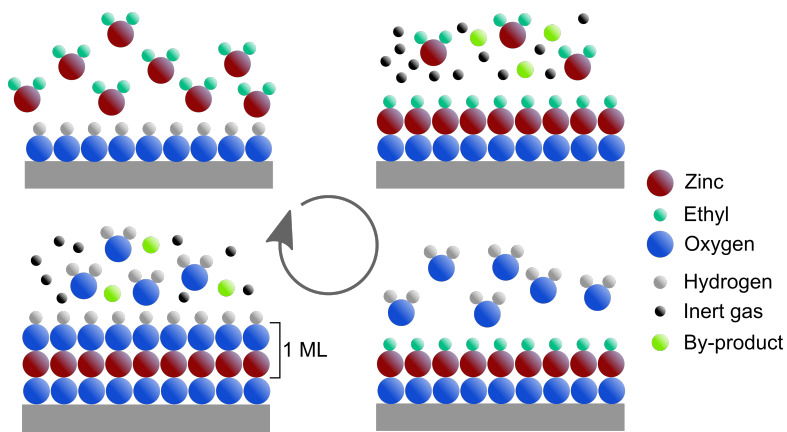
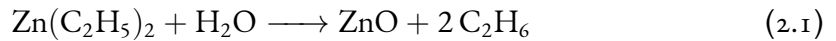
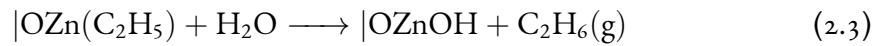
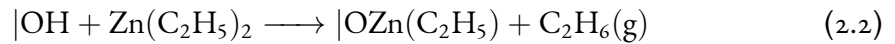


Figure 2.1: Schematics of an atomic layer deposition cycle of ZnO.



This reaction can be further separated into two half-reactions, occurring during the respective reactant steps



where $|\dots$ denotes a surface species. As mentioned, these half-reactions are separated by purging steps in which the by-products (in this case ethane, C_2H_6) and reactants are removed.

2.2.2 GROWTH PER CYCLE

After introducing the basic mechanisms of ALD, we will now deal with the concept of the growth per cycle (GPC). This parameter is arguably the most important one when talking about ALD growth. It is defined as the thickness increase of the deposited film when applying one ALD cycle. It can thus be directly obtained by *in-situ* thickness measurements (e.g. spectroscopic ellipsometry), or, assuming a constant growth, by *ex-situ* thickness measurements and normalization to the applied number of cycles. Note that in Figure 2.1 the GPC was depicted to be exactly one monolayer. Practically, the GPC will however be less than a monolayer due to effects such as steric hindrance (i.e. adsorbates block active groups on the surface). A monolayer can thus be considered the theoretical maximum of the GPC.

The defining characteristic of ALD is *self-limitation*. I.e., all steps within an ALD cycle have to reach saturation with respect to the deposited amount. For example, dosing more and more precursor must not lead to boundless growth. To check if the precursor dose leads to a self-limiting growth, the precursor dose is varied while high co-reactant doses and long purge times are used. The same procedure, i.e. varying of one of the steps while holding the others constant, is repeated for all steps. This allows for confirmation of self-limiting behavior and also an optimization of the processing times. Figure 2.2 shows a sketch of the GPC as a function of varying reactant doses and purge times. Too short reactant doses lead to a decreased GPC as not enough reactant molecules are available to bind to all active surface groups. On the other hand, too short purge times lead to an increased GPC as the reactants are allowed to react in the gas phase, thus the growth is not merely facilitated by surface reactions. For a self-limiting ALD process, therefore all four steps have to be operated in the saturated regimes, i.e. the flat part of the curve in which the GPC is independent of dose or purge time.

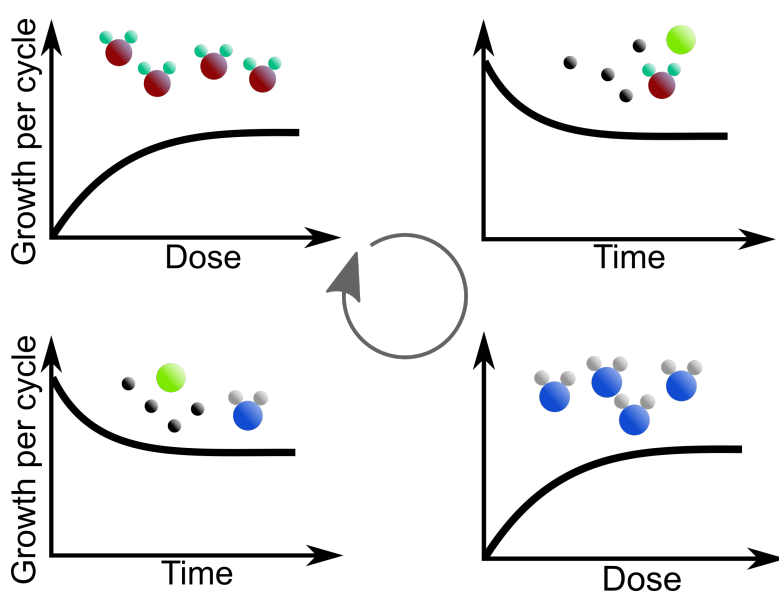


Figure 2.2: Growth per cycle as a function of reactant doses and purge times.

TEMPERATURE DEPENDENCE

The GPC typically varies with temperature.^{4,13} This behavior may be either caused by effects leading to non-ALD growth or effects leading to variation of the GPC while maintaining the self-limiting requirements of ALD and is sketched in Figure 2.3. At low temperatures, precursors may condense on the surface or the low temperature does not provide enough thermal

energy to drive the surface reactions. At high temperatures, the precursor may decompose and react without the co-reactant or the precursor may desorb from the surface without reacting. These effects lead to a non-ALD growth at the respective temperatures. At an intermediate temperature range, referred to as the *ALD window*, ideal ALD behavior can be achieved. However, the GPC may still vary with temperature. Decrease in GPC with temperature may be observed when the number of reactive sites decreases with increasing temperature. The GPC may increase with temperature when energy barriers of certain reactions are overcome, which might not be the case for lower temperatures. A constant GPC with temperature may occur when steric hindrance effects cause saturation, limiting the accessibility of reactive sites to a constant value. Furthermore, the GPC may go through a maximum and then decrease with increasing temperature, which can be caused by a combined effect of overcoming energy barriers for chemical reactions and decreasing number of reactive sites. Merely analyzing the temperature dependence of the GPC is thus not a valid method to judge whether a process is ALD at a certain temperature. An investigation on the saturation behavior of the steps of an ALD cycle is needed, ideally at different temperatures.

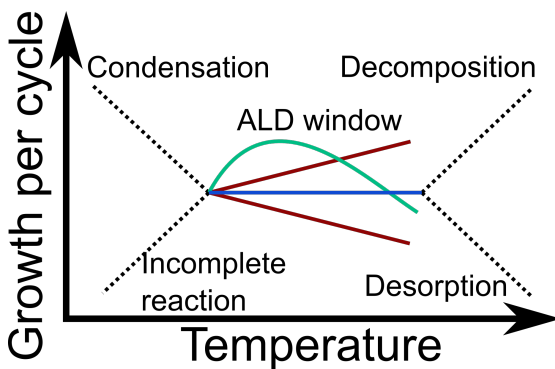


Figure 2.3: Variation of the growth per cycle with temperature. Colored regions refer to the ALD window, in which the process happens in a self-limiting way. Figure adapted from George⁴ and Puurunen¹³.

NUMBER OF CYCLES DEPENDENCE

During the deposition of a thin film by ALD, i.e. the repetition of an ALD cycle, the surface and, consequently, the number of available reactive sites are likely to change.^{14,13} First, the deposition happens only on the substrate surface. After a few cycles both the surface of the substrate and of the already deposited material are available for adsorption. And lastly, after complete coverage of the substrate with film, the surface consists only of the deposited film material. Due to these surface changes, the GPC may change in the *initial* stages, i.e.

initial number of cycles, of growth and is expected to settle to a constant value after a certain number of cycles (so-called *steady regime*). Puurunen et al.¹⁴ have classified the initial behavior of the GPC into four groups, a sketch of the GPC as a function of the number of cycles for the different groups is given in Figure 2.4. In *linear growth* (I), the GPC is constant over all cycles and the process works in the steady regime starting from the first cycle. This might be the case when the number of reactive sites is constant throughout the deposition. In *substrate-enhanced growth* (II), the GPC is higher in the beginning. This can occur when the number of reactive sites on the substrate surface is higher than on the deposited film. In *substrate-inhibited growth type 1 and type 2* (III and IV), the GPC is lower in the beginning than in the steady regime. This is the case when the number of reactive sites is higher on the deposited film compared to the substrate. In substrate-inhibited growth type 2, the GPC furthermore shows a maximum before settling to a constant value. This growth mode is often accompanied by island growth.

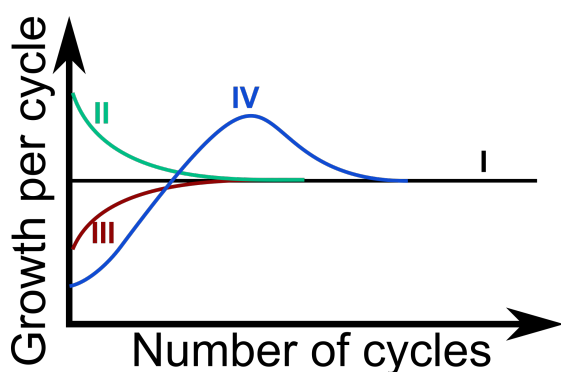


Figure 2.4: Variation of the growth per cycle with the number of cycles. (I) linear growth, (II) substrate-enhanced growth, (III) substrate-inhibited growth type 1, (IV) substrate-inhibited growth type 2. Figure adapted from Puurunen et al.¹⁴

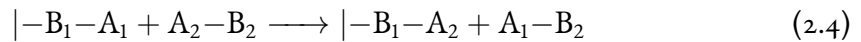
2.2.3 ADSORPTION

ALD relies on the self-limiting adsorption of precursor molecules. We will therefore go into more detail about the possible mechanisms of precursor adsorption.^{13,15} Generally, one can distinguish between physisorption and chemisorption of the reactant on the substrate. Physisorption relies on weak intermolecular forces such as van der Waals attraction and hydrogen bonding. Due to the weakness of the bonding, physisorbed precursors easily desorb from the substrate (e.g. in the purging step). Thus, physisorption is not the main mechanism of growth in ALD but might occur as an intermediate step before chemisorption.

In chemisorption, a chemical bond is formed between the precursor and the substrate. There exist several possible mechanisms of chemisorption in ALD.

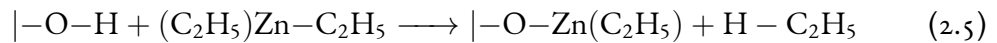
LIGAND EXCHANGE

In ligand exchange, two species exchange a ligand. For a general surface reaction ($|...|$ denotes a surface species), this can be written as:



where B_1 and B_2 are the ligands and A_1 and A_2 the (typically metal) center.

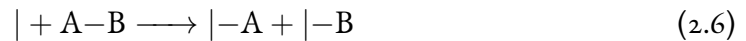
A typical example is the already discussed chemisorption of DEZ on a hydroxylated surface, releasing ethane as a volatile by-product:¹⁶



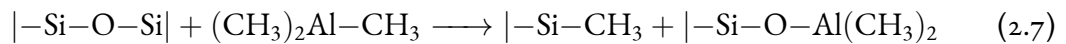
Also, if there are nearby active sites, the ligand exchange reaction can continue and result in multiple surface bonds.

DISSOCIATION

In dissociation, the precursor is split into fragments which subsequently bind to the surface:



This mechanism can often be observed for substrates with high surface energy, where adsorption decreases the surface energy. Another example is the chemisorption of trimethylaluminum onto siloxane bridges:¹⁷



in which an intra-substrate bond is broken.

ASSOCIATION

In association, the precursor binds to the surface, without bonds being broken.



While this mechanism appears to be similar to physisorption, the bond is built by an orbital overlap and thus may lead to surface saturation of the precursor and may be stable during the purging steps.

OXIDATION

Oxidation is a common process in ALD where strong oxidizers are used to remove organic ligands from precursors. Typically, the oxidant is incorporated in the films for non-noble metals, forming a metal oxide. For noble-metals, the partially oxidized surface created through the oxidant helps chemisorb the following metal precursor through oxidation of the ligands.

Figure 2.5 shows a summary sketch of the ligand exchange, dissociation, and association mechanisms.

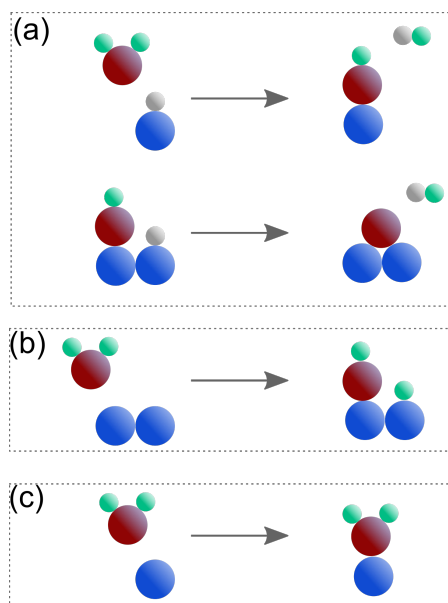


Figure 2.5: Sketch of the chemisorption mechanisms (a) ligand exchange (with a subsequent second bond), (b) dissociation, and (c) association. Figure adapted from Puurunen¹³.

PRECURSOR SATURATION

It was already mentioned that a monolayer per cycle is rather a maximum than a practically achievable growth per cycle in ALD. The saturation of the surface with the precursor is

hereby limited by two factors:¹³ *steric hindrance of ligands* and *limited number of reactive surface sites*. Steric hindrance of ligands leads to a blocking of active surface sites. These surface sites are thus not available for chemisorption of the precursor. In the second case, although there would be enough space for precursors to chemisorb, there are no more available reactive sites. However, in both cases, the precursor dosing leads to saturation. The achievable coverage is therefore governed by one of the two factors, which is practically influenced by e.g. the substrate material and possible pretreatment or the size of the precursor. Also, different adsorption mechanisms lead to different adsorbed species (i.e. different number of remaining ligands). As the adsorption mechanisms may change for different substrate temperatures, the substrate temperature can influence the GPC. Furthermore, the number of reactive sites is often a function of temperature, resulting in a combined effect on the GPC.

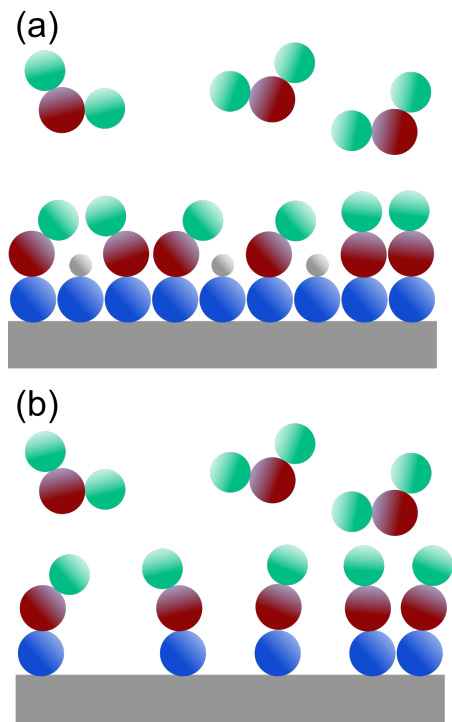


Figure 2.6: Sketch of precursor saturation mechanism by (a) steric hindrance of ligands, and (b) limited number of reactive surface sites. Figure adapted from Puurunen¹³.

2.2.4 GROWTH MODES

While the principle growth mode of ALD is usually described by layer-by-layer growth, different growth modes are possible.^{15,14} A schematic of these different modes is given in Figure

2.7.

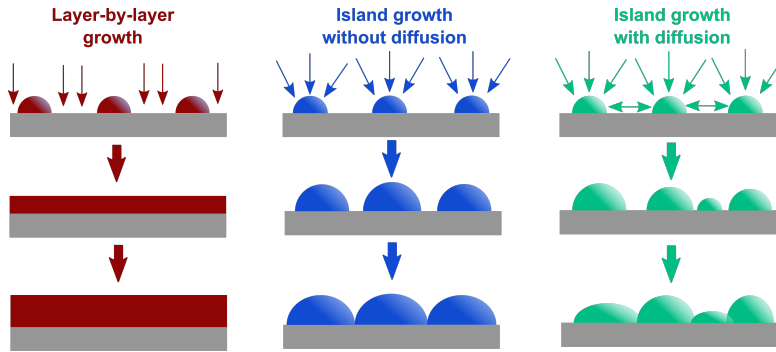


Figure 2.7: Sketch of the different growth modes which can occur in atomic layer deposition at different stages: layer-by-layer growth and island growth with and without diffusion. Figure adapted from Richey et al.¹⁵

Considering the case in which precursor adsorption is limited by steric hindrance (i.e. a vast number of reactive sites is available on the substrate) during the first ALD cycle, the subsequent deposition will proceed in a layer-by-layer fashion if the adsorption takes place preferentially in the gaps between deposited material (i.e. on the substrate). If, however, the precursor adsorbs preferentially on already deposited material, the deposition will proceed in an island growth fashion. This island growth can furthermore happen in the presence of surface diffusion of the islands/nanoparticles. Without diffusion, the island size will generally increase linearly (with ideally one monolayer per cycle on the surface of the island). When diffusion occurs, chemisorbed species move around the surface which may lead to collision and cluster formation. This will subsequently result in a polydisperse island size distribution. The surface diffusion of different species can be treated with a localized-hopping model, for which the diffusion coefficient (D) for a single atom or molecule can be written as:

$$D = D_0 e^{\frac{H_m}{kT}} \quad (2.9)$$

where D_0 is a diffusion constant, H_m the energy barrier for migration, k the Boltzmann constant, and T the temperature. For a nearest neighbor model $H_m = -\varepsilon_{mo}$, with ε_{mo} being the bond energy between adsorbed metal atom and surface. It thus follows that weak adsorbate-surface bonds and high temperatures promote high diffusivities.

Another phenomenon is Ostwald ripening, in which atomic or molecular species are transported from small nanoparticles to large ones. This happens due to a minimization of chemical potential, i.e. single atoms tend to attach to nanoparticles and large nanoparticles grow at the expense of small nanoparticles. The transport is facilitated either through surface dif-

fusion of single atoms or gas phase diffusion of volatile species. Similarly, nanoparticles as a whole can, due to minimization of their chemical potential, diffuse and coalesce (i.e. sinter).¹⁸ In this ALD growth mode, i.e. island growth with diffusion, the resulting particle distribution can be tuned by process parameters, such as the substrate temperature, the co-reactant, or the substrate material (or treatment of it). This is essential for applications such as catalysis, in which a high surface area of catalyst, i.e. a large number of small nanoparticles, is often preferred.¹⁸

2.2.5 PLASMA-ENHANCED ATOMIC LAYER DEPOSITION

A variant of atomic layer deposition is plasma-enhanced atomic layer deposition (PE-ALD). In this process, the energy for driving the ALD surface reactions is provided through reactive plasma species instead of (or additionally to) thermal energy.

PLASMA BASICS

According to the International Union of Pure and Applied Chemistry,¹⁹ a plasma is

A gas which is at least partly ionized and contains particles of various types, viz. electrons, atoms, ions and molecules. The plasma as a whole is electrically neutral.

For processing exploitations of plasmas, they are typically created through electric fields which accelerate free electrons.⁶ Through this gain in kinetic energy, the electrons are able to ionize, dissociate, and excite gas species through collisions. The electron temperature (which is a measure for the kinetic energy) in processing plasmas is typically orders of magnitude higher ($T_e \approx 3.5 \cdot 10^4 K$) than the gas temperature ($T_{gas} = 300 - 500 K$), thus one talks about cold plasmas. The species created through these electronic collisions, namely reactive neutrals (i.e. radicals), ions, and photons, can furthermore undergo additional gas-phase reactions, leading to the equilibrium condition in which the electron density equals the ion density. Collisions also lead to excitations of atoms and molecules. After returning from the excited state to the ground state, an optical spectrum is emitted, which gives the plasma its characteristic color, depending on the gas species. In optical emission spectroscopy, analysis of the spectrum gives valuable information on the created species.^{20,21} When the created plasma species arrive at the substrate surface, they can induce surface reactions, which is exploited for the use in deposition techniques. As the ionization degree in processing plasma remains rather low (typically $10^{-6} - 10^{-3}$), it is mainly radicals which drive the surface reactions. However, as ions are accelerated through the plasma sheath (i.e. positive space charge

layer at the interface between plasma and substrate which develops because of the deviating thermal energies of ions and electrons), this ion bombardment can provide additional energy to the substrate, can however also lead to damage in the layer.²²

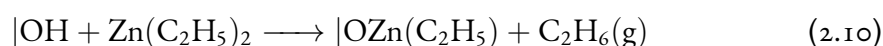
PLASMA AS A CO-REACTANT IN ATOMIC LAYER DEPOSITION

Using reactive plasma species as a co-reactant in ALD can offer several advantages compared to thermal ALD:⁶

1. *Reduced substrate temperature:* as the plasma provides a source of highly reactive species, less thermal energy is needed to drive the ALD surface reactions. This is especially important when dealing with temperature sensitive substrates such as polymers. However, careful tuning of plasma parameters is necessary to not damage the polymer by plasma species such as UV-photons or strong oxidizers.²³
2. *Improved material properties:* in many processes, the use of plasma can lead to films with enhanced density, electronic properties, and less impurities.
3. *Enhanced precursor application space:* for precursors that do not react with e.g. water at even high substrate temperatures, more reactive co-reactants are needed. The use of plasma as a co-reactant therefor widens the applications space of possible ALD precursors.
4. *Increased growth rate and shorter processing times:* PE-ALD processes often show an increased growth rate compared to thermal ALD. Furthermore, low temperature thermal processes with water often demand long purging times, which can be significantly reduced by using plasma.
5. *Tuning material properties:* through different reactor setups, the plasma and the interaction of plasma species with the substrate can be tuned to obtain the desired properties.²⁴ This offers generally additional versatility for tuning material properties compared to thermal ALD (in which the substrate temperature is the main tuning parameter).

Figure 2.8 shows a simplified sketch of a PE-ALD cycle for a ZnO process. Compared to Figure 2.1, the first half cycle remains the same while the H₂O precursor is exchanged for an O₂-plasma.

Similarly to thermal ALD of ZnO, the half-reactions of PE-ALD, applying DEZ and O₂-plasma, can be written as²⁵



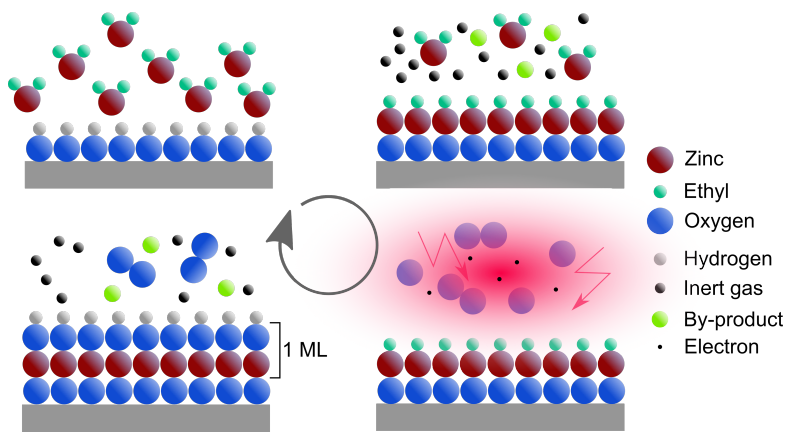


Figure 2.8: Schematics of a plasma-enhanced atomic layer deposition cycle of ZnO.



in which $|\dots$ denotes a surface species. The reactions were monitored by mass spectroscopy and optical emission spectroscopy.²⁵ We see that in the case of PE-ALD oxygen radicals drive the surface reaction and also the by-products from the second half-cycle are different to the ones from thermal ALD.

REACTOR TYPES

Several reactor types are available for PE-ALD. They differ mainly on the fact how the plasma is created and which plasma species take part in the surface reactions.^{6,23}

1. *Direct plasma*: in a direct plasma configuration, the substrate is directly placed within the main plasma zone. Usually, the substrate is placed on the grounded electrode within a capacitively-coupled plasma configuration, where the plasma is created between two parallel electrodes. The gases are often introduced through the powered electrode, which is often in the form of a showerhead. In direct plasma configurations, the flux of radicals and ions can be very high, allowing conformal and fast deposition. However, accelerated ions and high-energy photons may damage the films. This reactor type is used for the experiments in this thesis.
2. *Remote plasma*: in a remote plasma configuration, the substrate is not placed on parts creating the plasma (such as one of the electrodes) but the plasma is created remotely. The plasma may however still be present above the substrate and the ion and electron

density may be greater than zero. One of the advantages of this configuration is the ability to tune the plasma and substrate conditions independently. The remote plasma can be generated inductively-coupled (through a dielectric tube and a coil), with a hollow cathode, or with microwave electron cyclotron resonance.

3. *Radical-enhanced*: in a radical-enhanced configuration, the plasma is placed relatively far away from the substrate. Through surface collisions on the way to the substrate, most ions and electrons are lost and only radicals arrive at the substrate. However, also the radical flux may be substantially reduced. The difference between remote and radical-enhanced configurations is rather vague, and a configuration may be closer to one or the other. The general expression used for both configurations is remote plasma.

2.2.6 MATERIALS

A large number of materials and material combinations can be deposited by ALD. The possibilities range from pure metals²⁶, binary compounds such as metal oxides or nitrides,^{27,13} and doped, ternary, and quaternary compounds.²⁸ A database for published ALD processes, hosted by Eindhoven University of Technology, can be found online²⁹ and a snapshot is shown in Figure 2.9.

2.2.7 PROPERTIES AND APPLICATIONS OF ALD

UNIFORMITY, CONFORMALITY, AND THICKNESS CONTROL

The inherent growth mechanisms of ALD, i.e. self-limited surface reactions, allow for depositing *uniform* and *conformal* films.³⁰ Uniform films have the same thickness (and properties) everywhere on a planar substrate (such as a Si-wafer). Conformal films cover a 3D structure with the same thickness everywhere. Figure 2.10 shows ideal and non-ideal examples of film deposition on a planar and a 3D structure. As opposed to ALD, film growth in other techniques such as physical vapor deposition (e.g. evaporation or sputtering) happens through line-of-sight.³¹ This means that the growth depends on the provided gas flux. Areas which are close to the source of the flux will thus show increased growth rates and thicknesses compared to regions which are not in line-of-sight to the source. While this problem may be avoided for planar substrates by moving them far away from the source, this is generally not possible for 3D-structures which have regions outside the line-of-sight of the flux or which

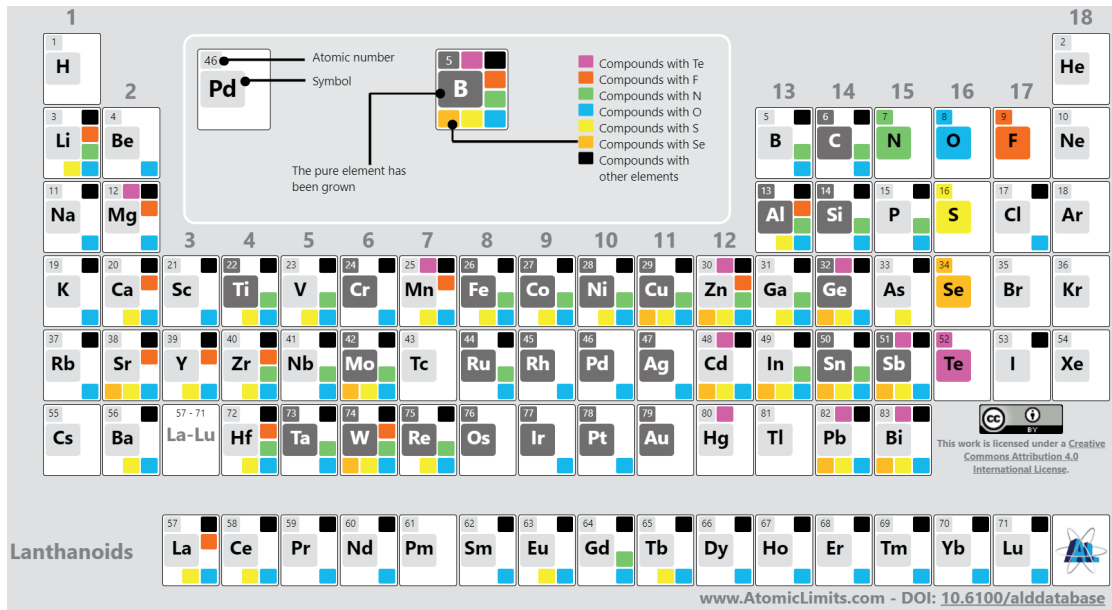


Figure 2.9: Table of elements which can be deposited by atomic layer deposition. Image reprinted from Ref.²⁹ (accessed on May 4th, 2020)

become inaccessible during the deposition through clogging of the entrance of e.g. narrow trenches.

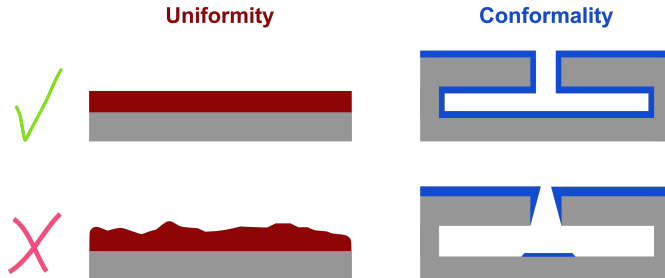


Figure 2.10: Schematics of ideal and non-ideal coatings regarding uniformity on a planar substrate and conformality on a 3D-substrate.

Another important property of ALD processes is the *precise thickness control*.³² This is again a consequence of the self-limitation of the surface reactions - the thickness can in principle be *discretely* controlled with a resolution equivalent to the GPC (i.e. in the Å/cycle range). This is different to flux-controlled techniques such as physical or chemical vapor deposition, in which the film growth happens *continuously* with time.

These inherent properties of ALD growth are exploited in a plethora of applications - some examples are presented now.

MICROELECTRONICS

In 1965, Gordon E. Moore predicted that the number of transistors per integrated circuit chip will double every two years. This prediction, widely known as *Moore's law*, was proven right in the last decades through miniaturization of device structures, accomplished by fabrication and materials improvements.³³ ALD came into play for upholding Moore's law in 2007, when Intel started to use a gate oxide with high dielectric constant based on ALD grown hafnium oxide.³⁴ Since then, the fabrication has moved to more complicated structures such as FinFETs,³⁵ in which conformal coating of 3D-structures is essential.⁵ Further scaling down of structures might introduce additional technologies in the process, such as *atomic layer etching*, the counterpart of atomic layer deposition in which (sub-)monolayers of material are sequentially removed instead of deposited.³⁶

ENCAPSULATION OF ORGANIC ELECTRONICS

Organic electronics such as organic light emitting diodes (OLEDs) suffer from long-term stability due to degradation in the presence of atmospheric water and oxygen. To extend the lifetime of such devices, a thin and dense encapsulation layer needs to be applied to lower the water vapor transmission rates to the active parts of the device.³⁷ ALD has been shown to be a suitable technique for the application of such encapsulation layers and often metal oxide films such as Al_2O_3 are used for that purpose. As the encapsulation layer can be made very thin, the flexibility of the device is unchanged and furthermore the conformality of ALD allows preserving of potential nano structuring of the active material. Further improvements can be achieved by growing hybrid organic/inorganic encapsulation layers by *molecular layer deposition*, a variant of ALD in which organic and inorganic layers are alternated in a self-limited way.³⁸

COATING OF NANOPARTICLES

The conformal coating of small objects such as nanoparticles is of interest for many applications.³⁹ Using ALD, ultrathin and conformal films can be applied on nanoobjects without altering their basic properties.⁴⁰ For the coating of nanoparticles, often fluidized bed reactors are used.⁴¹ These are designed in order to move the particles around, exposing the whole surface to the ALD precursors and to prevent agglomeration. Due to high combined surface area of the particles compared to a planar substrate, significantly larger amounts of precursors and reaction times have to be used for conformal coating. The ALD coating can serve

as a gas diffusion barrier to prevent polymer degradation, as a surface passivation layer to prevent photocatalytic activity of particles in a suspension (e.g. pigment TiO_2 in paint), or as a stabilizer of battery cathode materials.³⁹

2.3 VAPOR PHASE INFILTRATION

Vapor phase infiltration is a technique which emerged from the application of atomic layer deposition on polymers.⁴² In 2005, Wilson et al.⁴³ investigated the growth of ALD Al_2O_3 (using trimethylaluminum (TMA) and water) on polymer films such as poly(methyl methacrylate) (PMMA) and polystyrene (PS). The mass uptake of the polymers from the same amount of precursor showed very different behavior for the respective polymers for the initial number of cycles. PMMA showed large precursor uptake upon TMA dosing but subsequent loss of most of the precursor molecules after dosing (corresponding to precursor sorption and desorption). For PS, the initial uptake was smaller but did not decrease. After several ALD cycles, the growth was found to be similar on both polymers. The authors concluded that in certain polymers, the ALD precursors can sorb, diffuse, and become entrapped in the near-surface of the polymer. After coalescence of Al_2O_3 clusters in the near-surface region, further diffusion is blocked and the dense Al_2O_3 grows on the surface. While researchers at that time were mostly interested in ALD layers *on* a polymer surface (e.g. for gas diffusion barriers), the results showed that the same ALD precursor can penetrate *into* the bulk of the polymer and potentially modify bulk properties, a phenomenon which is not observed on dense metal or metal oxide substrates. This caused the rise of the technique *vapor phase infiltration*^{*}, which will be dealt with in the following sections.

2.3.1 PRINCIPLES

Vapor phase infiltration (VPI) and atomic layer deposition (ALD) share similar processing schemes, i.e. sequential delivery of precursor and co-reactant, and the same precursor chemistry (e.g. metalorganics). However, the interaction of the precursor with the substrate is fundamentally different. In VPI, the precursors diffuse into the bulk of the substrate while in ALD the precursors react with functional groups on the surface of the substrate. Because of these varying mechanisms, the reactants are often introduced differently in ALD and VPI.^{7,42} Figure 2.11 illustrates these differences by plotting the relative partial pressures of the reac-

^{*}In the literature, different names have been used for this technique such as sequential infiltration synthesis or multiple pulsed infiltration.⁷ In this thesis only the term vapor phase infiltration is used for clarity.

tants and purge gas during ALD and VPI cycles. In ALD, the reactants are sequentially introduced and temporally separated. Usually, a constant inert gas stream is present which purges the reactor from unreacted precursors and by-products. The precursor and co-reactant exposures are often only in the range of milliseconds or seconds due to the fast reaction with reactive surface groups. In VPI, the reactants are introduced into the reactor and held in a static environment (e.g. by closing the connection to the vacuum pump). This hold step allows diffusion and entrapment into the bulk of the polymer which potentially (depending on diffusivity of the precursor and thickness/size of the polymer) may require minutes or hours to reach saturation. Different processing schemes exist for VPI:⁷ in semi-static mode sequential infiltration synthesis (SIS), the reactor is evacuated to base pressure before introducing the purging gas (shown in Figure 2.11). In flow mode SIS or multiple pulsed infiltration, the chamber is not evacuated before purging, similar to typical ALD processes. In sequential vapor infiltration, the same precursor is introduced multiple times before introducing the co-reactant. This may be useful for studying saturation limits.

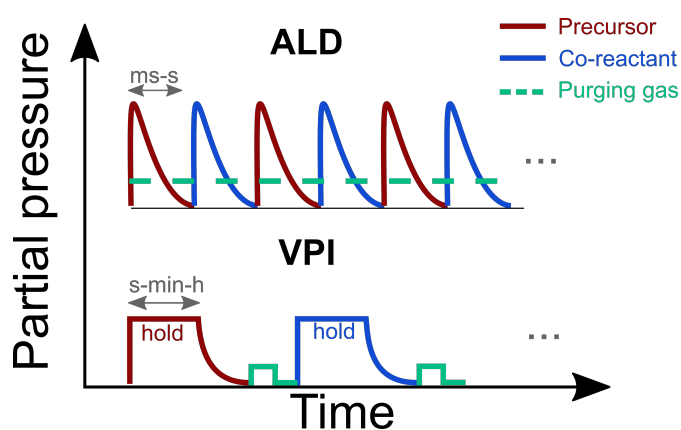


Figure 2.11: Schematics of the relative partial pressures of reactants and purging gas during ALD and VPI (semi-static mode). Figure adapted from Leng et al.⁷ and Waldman et al.⁴²

There are three key steps for the interactions of precursors with the polymer substrate in VPI: (1) *sorption* of the precursor into the polymer, (2) *diffusion* of the precursor in the polymer matrix, and (3) *entrapment* of the precursor within the polymer (by e.g. reaction with functional groups).⁷ These steps are depicted in Figure 2.12 and are explained in more detail.

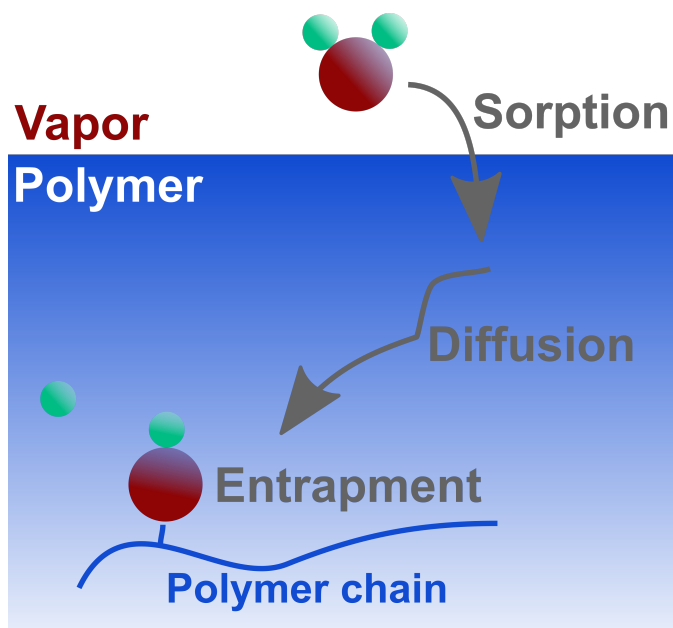


Figure 2.12: Schematics of the key steps in the interaction of precursor and polymer in VPI: sorption, diffusion, and entrapment. Figure adapted from Leng et al.⁷

SORPTION

In VPI, the first step is sorption (dissolution), in which gas molecules enter the polymer.⁷ For this to happen, the precursor must be soluble in the polymer. Henry's law can be used to describe pure dissolution:

$$C = S \cdot p \quad (2.12)$$

in which C is the concentration of gas molecules in the polymer, S the solubility coefficient, and p the partial pressure of the sorbing gas. The solubility coefficient S furthermore scales with the temperature T according to a van't Hoff equation:

$$S = S_0 \exp\left(-\frac{\Delta H_S}{kT}\right) \quad (2.13)$$

where S_0 is a constant, k the Boltzmann constant, and ΔH_S the partial molar enthalpy of sorption. By measuring the equilibrium solubility coefficients (e.g. gravimetrically) at different temperatures, ΔH_S can be extracted for a specific precursor-polymer couple.

DIFFUSION

Once a precursor molecule enters the polymer, it is called penetrant. Diffusion refers to the transport of penetrants within the polymer. Diffusion can be divided into four categories:⁷ (1) viscous flow, (2) Knudsen diffusion, (3) molecular sieving, and (4) solution-diffusion. Depending on the ratio of the pore size of the polymer structure and the mean free path of the penetrants, one or the other mechanism prevails. In VPI, solution-diffusion usually best describes the diffusion mechanism and is driven by a chemical potential gradient due to the concentration gradient of penetrant molecules. Fick's second law describes the change of penetrant concentration C with space and time (t):^{44,42}

$$\frac{\partial C}{\partial t} = D\nabla^2 C \quad (2.14)$$

where D is the diffusion coefficient.

In the one-dimensional case, e.g. the diffusion into a polymer thin film, the equation can be written as:

$$\frac{\partial C}{\partial t} = D \frac{\partial^2 C}{\partial x^2} \quad (2.15)$$

where x is the distance into the film.

Applying the boundary conditions for a thin film on an impermeable substrate with a constant precursor concentration (C_{max}) at the polymer surface, Fick's second law yields:⁴⁴

$$C(x, t) = C_{max} \left(1 - \sum_{n=0}^{\infty} \frac{2}{\lambda_n^2} \sin \left(\frac{\lambda_n x}{L} \right) \exp \left(-\frac{D\lambda_n^2 t}{L^2} \right) \right) \quad (2.16)$$

where

$$\lambda_n = \frac{(2n+1)\pi}{2}, \quad n = 0, 1, 2, \dots \quad (2.17)$$

and L is the film thickness. By integrating the solution one can obtain the total mass uptake at a specific time (M_t), which can be normalized to the mass uptake at infinite time (M_∞ , i.e. when the film is fully infiltrated):

$$\frac{M_t}{M_\infty} = 1 - \sum_{n=0}^{\infty} \frac{2}{\lambda_n^2} \exp \left(-\frac{D\lambda_n^2 t}{L^2} \right) \quad (2.18)$$

Plotting this equation as function of \sqrt{t} , the diffusion coefficient can be extracted from

the initial linear slope:

$$\frac{M_t}{M_\infty} = \frac{2}{L} \left(\frac{D}{\pi} \right)^{\frac{1}{2}} \quad (2.19)$$

Therefore, by measuring the mass uptake as a function of time *in-situ* or *ex-situ* by e.g. gravimetry, the diffusion coefficient can be extracted.

Furthermore, diffusion is a thermally activated process, thus it follows a van't Hoff equation:

$$D = D_0 \exp \left(-\frac{\Delta H_D}{kT} \right) \quad (2.20)$$

where D_0 represents the frequency of attempts for a single diffusional hop of the penetrant and ΔH_D the activation energy for diffusion. By extracting diffusion coefficients at different temperatures and plotting $\ln(D)$ as a function of $1/T$ (Arrhenius plot), ΔH_D and D_0 can be obtained from a linear fit.

ENTRAPMENT

After sorption and diffusion of the precursor in the polymer, there are several mechanisms by which the precursor may be entrapped.⁷ If polymer functional groups are available and the precursor-polymer combination is moderately reactive, the penetrant can diffuse (through a substantial amount of polymer) and become entrapped via a *chemical reaction*. The inorganic moiety will thus not be removed by a subsequent purge step as it is permanently bound.

If the polymer-precursor combination is not reactive toward one another the precursor may be *physically* entrapped, however, no chemical bond is formed. Upon applying a long purge, the precursor will diffuse and desorb out of the polymer (i.e. leaving it inert). If, however, only a short or no purge is performed after the precursor physical entrapment and a co-reactant is dosed, the reacted complex might become permanently entrapped due to the increased steric hindrance. In this case, infiltration is not limited and affected by the number of reactive groups but only the kinetics of in- and out-diffusion of precursor and co-reactant and the respective reaction rates.

If the polymer contains highly reactive groups for the precursor, the reactions may mainly occur at the surface, creating a dense barrier layer. This barrier layer blocks further sorption and diffusion of precursor into the bulk of the polymer. I.e., this process cannot be considered a form of VPI but rather ALD.

2.3.2 PROPERTIES AFFECTING PROCESS KINETICS

Four key properties of the polymer-precursor combination have large influence on the process kinetics of VPI: size and shape of the precursor, free volume of the polymer, tortuosity of the free volume, and reactivity of the precursor.⁷

SIZE AND SHAPE OF THE PRECURSOR/PENETRANT

The size and shape of the penetrant affects its diffusivity in polymers. Berens and Hopfenberg⁴⁵ found that the diffusivity of spherical-shaped molecules (in amorphous polymers below T_g) decreases exponentially with increasing molecule diameter. Molecules with non-spherical shape such as CO_2 showed higher diffusivity than expected from their mean size, suggesting that such penetrants move primarily with their long axes parallel to diffusion paths. Potential dissociation of precursor molecules (i.e. decrease in size) upon sorption into the polymer may also affect the resulting diffusivity.⁷

POLYMER FREE VOLUME

The free volume of a polymer is a consequence of a not close-packing of chains due to entropic and bonding constraints.⁷ This gives the material a porosity on the atomic scale which does not occur in close-packed crystalline solids. In Figure 2.13, the specific volume (volume per mass) of an amorphous polymer below and above its glass transition temperature (T_g) is plotted. The specific free volume can be split into two components: the polymer chain volume (red) and the free volume (yellow). The polymer chain volume increases monotonically with temperature due to thermal vibrations. The free volume remains constant below T_g , increases however rapidly above T_g . The fractional (with respect to total specific volume) free volume of a polymer above T_g can be written as

$$v_f = v_{fT_g} + \Delta\alpha(T - T_g) \quad (2.21)$$

where v_{fT_g} is the fractional free volume at T_g , and $\Delta\alpha$ is the difference of the thermal expansion coefficient above and below T_g .

The free volume (below T_g) is furthermore dependent on the processing history. As such, higher free volume can be achieved at lower temperature by e.g. a fast cool-down (quenching) from the rubbery state.

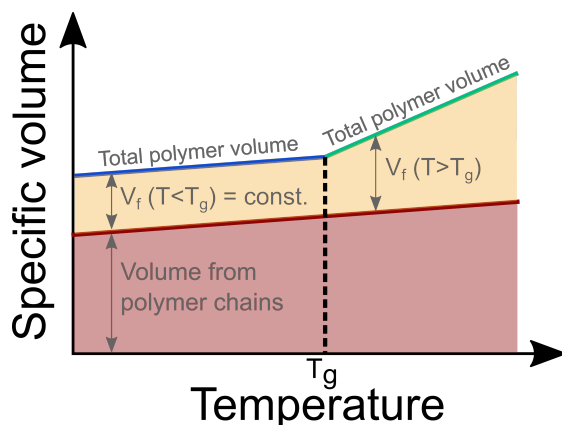


Figure 2.13: Schematic plot of the specific volume of a polymer as a function of the temperature. Figure adapted from Leng et al.⁷

TORTUOSITY

The penetrant can rarely move straight through the free volume but has to move in curved pathways to circumvent chains which are in its way.⁷ This tortuosity effectively reduces the diffusivity and may be increased by adding bulky side groups to the polymer chains.

PRECURSOR-POLYMER REACTIVITY

The reactivity of the precursor toward polymer functional groups is another factor which strongly influences the process kinetics.⁷ For inert polymers, lacking strong functional groups, the kinetics can be considered purely diffusional. For polymers with more reactive groups, the kinetics depend both on diffusion and reaction rates. Binding of the precursor to the polymer will change the chemical structure and also factors such as the free volume or the tortuosity which may disrupt subsequent penetrant diffusion. The reaction rates are hereby temperature dependent, i.e. they increase with increasing substrate temperature and reactions are likely to take place near the surface. This reacted and therefore denser surface layer can act as barrier layer preventing further diffusion. Thus, for modestly reactive polymers, the kinetics at low temperature are diffusion controlled while at high temperatures they are reaction controlled. In an intermediate temperature regime, the process is controlled by both diffusion and reaction kinetics, which makes it more difficult to interpret experimental data.

2.3.3 APPLICATIONS FOR VPI

The infiltration of organic materials with inorganics creates organic/inorganic hybrid materials with unique properties.^{7,46,47} The infiltration can either aim on enhancing polymer properties (mechanical, optical, electrical, etc.) or the polymer is used as a template which is later removed to obtain a nanostructured or porous inorganic. While VPI has not yet had a wide industrial use unlike ALD, many interesting application spaces have been discovered, of which some examples are shown here.

MECHANICAL STRENGTHENING

The first demonstration of enhanced properties using infiltration by Lee et al. was published in 2009.⁴⁸ In this study, spider silk was infiltrated with several metals using metalorganic precursors and water. The infiltrated fibers showed largely enhanced toughness due to breakage of hydrogen bonds and replacement with covalent bonds formed by the infiltrated species. The enhanced mechanical properties could not be reproduced by depositing an ALD coating on the silk but are a consequence of a bulk modification.

CHEMICAL STABILITY

McGuiness et al. investigated the infiltration of organic solvent separation membranes.⁴⁹ These membranes often show a weak chemical stability in strong solvents and dissolve. Infiltrating polymer of intrinsic microporosity-1 (PIM-1) fibers with TMA and water resulted in largely enhanced dissolution stability in solvents such as tetrahydrofuran. The separation performance of the infiltrated membranes was furthermore increased compared to the pristine membrane. Investigation of the infiltration process showed that the TMA does not form a chemical bond with PIM-1 but a semi-stable adduct and after the water dose and further cycles an intertwined structure is formed between the PIM-1 chains and the metalorganic which gives the infiltrated membrane its stability. In another study by McGuiness et al.,⁴⁹ the stability of AlO_x /poly(methyl methacrylate) hybrid thin films was tested. The study showed that the process temperature has a large impact on the hybrid material's structure. At low process temperatures, the inorganic is physically entrapped and entangled with the polymer chains. For high process temperatures, the inorganic chemically binds to the polymer. This leads to different dissolution behavior in different solvents, whereas films processed at high temperatures were stable in all investigated solvents while films processed at low temperatures only in some. Furthermore, the infiltration of a bulk object (1x2x0.25 inch) was investigated,

and it was shown that infiltration into a depth of only $0.5 \mu\text{m}$ was sufficient to prevent dissolution. The exposure time to the precursor was 17 hours in this experiment.

MATERIAL PATTERNING BY BLOCK COPOLYMER TEMPLATES

Block copolymers (BCP) represent an interesting substrate for subsequent infiltration. In a block copolymer, the polymer chain consists of alternating blocks of different types of polymers. Self-assembly of BCPs can lead to different nanostructures like spheres, cylinders, and lamellae.⁵⁰ The size and shape of the formed structure is governed by composition and chain architecture and can therefore be tuned. VPI can be used to selectively infiltrate one of the blocks, whereas, after removal of the polymer template, the remaining inorganic structure replicates the structure of the BCP. The most widely studied BCP for this purpose is polystyrene-*block*-poly(methyl methacrylate) (PS-*b*-PMMA). By infiltrating this BCP with TMA, the precursor reacts only with functional groups in the PMMA block, leaving the PS block inert.⁵¹ By removing the polymer template thermally or with plasma, the inorganic resembles the PMMA blocks. A schematic of this process is shown in Figure 2.14. Different inorganic material structures can be produced in that way, whereas often a TMA priming step needs to be introduced for less reactive precursors.⁵²

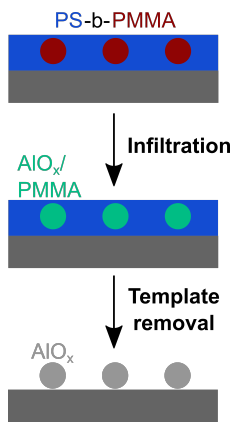


Figure 2.14: Schematic of the infiltration of aluminum oxide into PS-*b*-PMMA and subsequent removal of the polymer template. Figure adapted from Peng et al.⁵²

2.4 PROPERTIES AND APPLICATIONS OF ZnO

Zinc oxide is a II-VI semiconductor with a wide band gap ($E_g \approx 3.3 \text{ eV}$ at room temperature).^{2,53} It crystallizes in the hexagonal wurtzite structure and shows relatively strong ionic

binding. It has a density of about 5.6 g/cm^3 and shows a large exciton binding energy (60 meV). Several 100,000 tons of ZnO are used per year as e.g. additives in concrete or in rubber tires. Due to its non-toxicity it is also used in the pharmaceutical and food industry.

2.4.1 GROWTH

Growth of *bulk* ZnO can be facilitated by methods such as *vapor phase transport*,² in which zinc oxide or zinc metal is evaporated and transported to a reaction chamber by an inert gas (where oxygen gas is added). The reactor consists of a quartz tube which is placed in an oven and the growth happens through controlling the temperature gradient. A further bulk growth technique is *hydrothermal growth*,⁵³ in which the growth happens on ZnO single crystal seeds and is fueled by a supersaturated solution.

For *thin film* growth of ZnO, *metal organic chemical vapor deposition* (MOCVD) can be used.² In MOCVD, a metalorganic (e.g. DEZ) and an oxidant are simultaneously introduced in a vacuum reactor and react at the substrate surface. When oxygen is used as co-reactant very low pressures have to be used in order to prevent gas phase reactions. At high temperatures, self-organization can occur which results in the growth of ZnO nanorods, which are interesting for a plethora of applications. In *molecular beam epitaxy* (MBE),² Zn is evaporated from effusion cells in an ultra-high vacuum reactor. At these low pressures, oxygen is not very reactive toward the Zn metal. Thus, it has to be activated through a plasma cell or another oxidant such as water is used. In *pulsed laser deposition* (PLD),² an excimer laser pulse is guided onto a ZnO target (e.g. sintered ZnO powder). The laser pulse flash evaporates the material and forms a plasma plume in the gas phase. The reactive species from the plasma plume then impinge on the substrate surface and redeposit. In this thesis, the growth of ZnO by (PE-)ALD is investigated, which offers several advantages to the mentioned techniques. An overview of the literature on (PE-)ALD of ZnO is given in the introductions of the experimental chapters in part II of this thesis.

2.4.2 ELECTRICAL AND OPTICAL PROPERTIES

As-grown ZnO is typically n-type.² The origin of this conductivity has been under debate and is likely to stem from intrinsic defects or unintentional doping with hydrogen. For the intrinsic defects, Zn-interstitial complexes are likely to play a role in the conduction mechanism.⁵⁴ The n-type doping can be controlled by metal dopants such as Al, Ga, or In. These compounds are interesting as a cheap (and non-toxic) alternative to the transparent conduc-

tive oxide indium tin oxide.² Furthermore, the surface conductivity of ZnO can be modified by adsorbed gas molecules, making ZnO a candidate for gas sensors for a plethora of gases.^{2,55} With its wide band gap, ZnO is transparent in the visible region of the optical spectrum. This is applied in transparent electronics, such as a already mentioned transparent conductive oxide. Furthermore, it is used as a UV-blocking additive in e.g. sunscreen.² The high exciton binding energy in ZnO allows excitonic emission in optically pumped lasers.⁵⁶

2.4.3 PIEZOELECTRIC PROPERTIES

In piezoelectric crystals, the application of stress produces an electrical polarization.⁵³ This can be written as:

$$P_i = e_{ijk}\epsilon_{jk} = d_{ijk}\sigma_{jk} \quad (2.22)$$

in which P_i is the produced polarization, e_{ijk} and d_{ijk} are the piezoelectric strain and stress coefficients, respectively, and ϵ_{jk} and σ_{jk} are the strain and stress, respectively. In the indirect piezoelectric effect, strain ϵ_{jk} is produced upon an application of an electric field E_k :

$$\epsilon_{ij} = d_{ijk}E_k \quad (2.23)$$

Due to crystal symmetry of the wurtzite structure, only 3 independent piezoelectric coefficients remain:

$$\begin{pmatrix} P_{xx} \\ P_{yy} \\ P_{zz} \end{pmatrix} = \begin{pmatrix} 0 & 0 & 0 & 0 & e_{15} & 0 \\ 0 & 0 & 0 & e_{15} & 0 & 0 \\ e_{31} & e_{31} & e_{33} & 0 & 0 & 0 \end{pmatrix} \begin{pmatrix} \epsilon_{xx} \\ \epsilon_{yy} \\ \epsilon_{zz} \\ \epsilon_{xy} \\ \epsilon_{yz} \\ \epsilon_{zx} \end{pmatrix} = \begin{pmatrix} 0 & 0 & 0 & 0 & d_{15} & 0 \\ 0 & 0 & 0 & d_{15} & 0 & 0 \\ d_{31} & d_{31} & d_{33} & 0 & 0 & 0 \end{pmatrix} \begin{pmatrix} \sigma_{xx} \\ \sigma_{yy} \\ \sigma_{zz} \\ \sigma_{xy} \\ \sigma_{yz} \\ \sigma_{zx} \end{pmatrix} \quad (2.24)$$

Two components, e_{31} and e_{33} , represent contributions to the polarization P_{zz} along the crystallographic c -axis:²

$$P_{zz} = e_{33}\epsilon_{zz} + e_{31}(\epsilon_{xx} + \epsilon_{yy}) \quad (2.25)$$

whereas $\epsilon_{zz} = (c - c_0)/c$ corresponds to a strain along the c -axis and $\epsilon_{xx,yy} = (a - a_0)/a_0$

strain in one of the basal planes, respectively. The third component of the piezoelectric tensor, e_{15} , describes polarization induced by shear strain and is often neglected for simplicity.

The piezoelectric properties of ZnO have been widely used in surface acoustic wave (SAW) devices.⁵⁴ In this, a voltage is applied to a piezoelectric material at the launching transducer to create a mechanical (acoustic) wave which travels through a material and is converted again to an electrical signal at a receiving transducer. Furthermore, the piezoelectric properties of ZnO, and especially nanostructures of ZnO, are exploited in the research field of nanogenerators, in which mechanical energy is converted to electrical energy to power small devices.³ This research field developed in 2006, when Wang et al. investigated the output voltage of bended ZnO nanowires⁵⁷ and has emerged to more complex device structures.⁵⁸

3

Experimental Setup

3.1 REACTOR DESIGN FOR PLASMA-ENHANCED ATOMIC LAYER DEPOSITION

Figure 3.1 shows a schematic of the setup of the PE-ALD reactor. The control of the gas valves happens fully automated, a detailed description of the software and the automation hardware is given in section 3.3. The flow of oxygen and argon is controlled through mass flow controllers (MFC). To prevent pressure spikes in the reactor due to the closure of a gas line with a valve (overpressure in front of the valve), by-pass lines are installed in the setup, which direct the flow directly into the rotary pump. I.e., there is a constant flow of oxygen and argon, either into the reactor or into the pump. Magnetic valves are used for this purpose. The delivery of the metalorganic precursor DEZ happens through an ultrafast (ms range) membrane valve. The valve is pneumatically actuated through a solenoid. The high vapor pressure of the precursor allows delivery at room temperature without the need of additional heating sources. The plasma is generated through a radio frequency (RF, 13.56 MHz) power generator and a matching network. The electric line is fed into the reactor through a coaxial connection and is connected to the showerhead electrode which serves as the top electrode. The substrates are placed on the heating stage on the grounded reactor bottom which serves as the bottom electrode. As the substrates are directly placed on one of the electrodes (in this case the grounded one), the configuration is called a direct plasma reactor.⁶ The temperature of the heating stage is controlled through a temperature controller and the temperature is measured through a thermocouple welded on top of the stage. Furthermore,

the reactor body as well as the precursor delivery line are heated on the atmosphere side to prevent condensation of precursors, water, etc. The pumping system consists of a turbomolecular pump and a rotary vane pump. To control the working pressure of the deposition, a butterfly valve controls the opening of the connection to the turbomolecular pump. The main purpose of the turbomolecular pump in this system is not to achieve ultrahigh vacuum but rather to allow fast pumping of the gas species. When no process is running, the reactor is only pumped through the rotary pump, with the turbomolecular pump being isolated by valves.

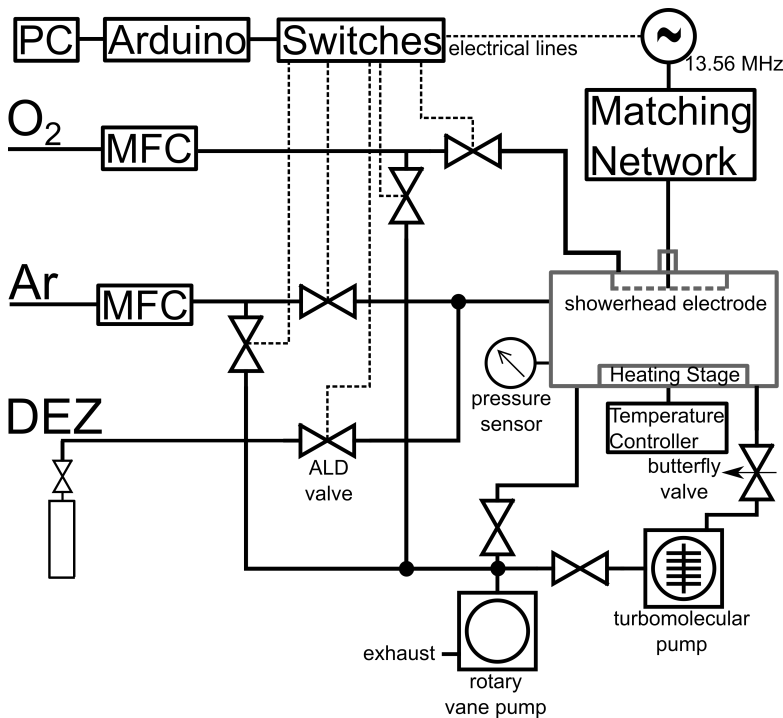


Figure 3.1: Schematic of the experimental setup for the PE-ALD process.

3.2 REACTOR DESIGN FOR VAPOR PHASE INFILTRATION

Figure 3.1 shows a schematic of the setup of the VPI reactor. The experiments were performed in the group of Prof. Mark D. Losego at the Georgia Institute of Technology, USA. The automation in this setup is facilitated through a LabView program.⁵⁹ Differently to the PE-ALD setup in which electric lines are installed to the solenoids of the individual gas valves, the program controls the pneumatic outputs of different channels by placing the solenoids

in a control box. From the control box, gas lines are connected to the ALD valves. Nitrogen serves as the pneumatic gas as well as the purging gas (controlled through a mass flow controller). In the VPI process, DEZ and water are used as precursors to infiltrate ZnO into the substrates. The pumping system consists of a rotary vane pump and filters for trapping unreacted precursors. During precursor exposure, the chamber is isolated from the pump to allow for ongoing diffusion of the precursor into the substrate. This is facilitated with a pneumatically controlled gate valve. The heating system, divided into individually heated zones, is merely on the atmosphere side of the chamber and the substrates are directly placed on the reactor bottom.

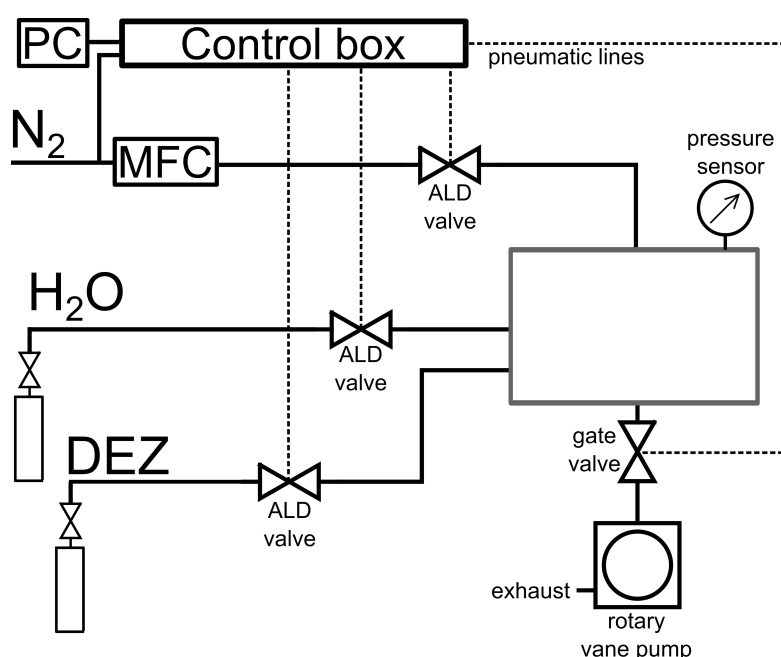



Figure 3.2: Schematic of the experimental setup for the VPI process.



3.3 UNIVERSAL SOFTWARE FOR THE REAL-TIME CONTROL OF SEQUENTIAL PROCESSING TECHNIQUES

3.3.1 PREFACE







Universal software for the real-time control of sequential processing techniques

Cite as: *J. Vac. Sci. Technol. A* **37**, 063201 (2019); <https://doi.org/10.1116/1.5125052>
Submitted: 20 August 2019 . Accepted: 19 September 2019 . Published Online: 22 October 2019

Julian Pilz , Martin Tazreiter, and Anna Maria Coclite 

COLLECTIONS

Paper published as part of the special topic on [Special Topic Collection on Atomic Layer Deposition \(ALD\)](#)
Note: This paper is part of the 2020 Special Topic Collection on Atomic Layer Deposition (ALD).

The work was conducted at Graz University of Technology. The author of the thesis wrote parts of the code, performed the signal analysis, and wrote the manuscript, Martin Tazreiter developed the concept of the software and wrote parts of the code, and Anna Maria Coclite supervised the work. All authors reviewed the manuscript. The following text and images are identical to the published work:

- Pilz, J.; Tazreiter, M.; Coclite, A. M. Universal Software for the Real-Time Control of Sequential Processing Techniques. *J. Vac. Sci. Technol. A* **2019**, 37 (6), 063201

3.3.2 INTRODUCTION

Sequential process control is essential for many thin film processing techniques such as atomic⁴ and molecular layer deposition³⁸ (ALD and MLD), molecular beam epitaxy,⁶⁰ and atomic layer etching.⁶¹ In these processes, valves or shutters are used to dose precursors in a vacuum reactor. The dosing has to happen in a fully automated and reproducible way and often has to be quite short (e.g., around ~10 ms for metalorganic precursors in ALD). Furthermore, novel

hybrid materials require exact control of the composition and grading of their various components to obtain the desired properties.⁶² Implementations of control programs for thin film deposition have been reported in the literature. Selvaraj and Takoudis⁶³ have reported on a program that is able to deliver four different precursors as well as oxidant and purging gases in a sequential fashion. The number of supercycles and the number of layers of a material within one supercycle can be chosen in the program. This makes it possible to deposit general sequences like $[[A]v [B]w [C]x [D]y]z$, where A, B, C, and D are the depositions of the individual materials; v, w, x, and y are the number of cycles of the specific materials; and z is the number of supercycles. The program has been implemented in labview. Piercy and Losego⁵⁹ have presented a more versatile program. Their tree-based approach offers the possibility to implement more complex structures such as graded laminates and sandwich structures. The program is not limited to the number of precursors and the order of complexity (the sequence above could be called a second order process as there is a loop over the supercycles and a loop over the individual materials) and has also been implemented in labview. In neither of the mentioned publications has a hardware integration (i.e., the transfer of sequence signals to valves, etc.) been presented. In this publication, we present both a graphical user interface (GUI) for the development of universal recipes for sequential processes and the firmware for the execution of such a recipe on an external microcontroller. The GUI was developed in python, an Arduino Uno was used as the microcontroller, and its firmware was written in C/C++ using the Arduino IDE. In our opinion, this approach has several advantages compared to the ones in the literature:

1. Only open-source software and hardware are used.
2. The cost for the necessary hardware control (Arduino + relay/MOSFET module) is low.
3. The Arduino platform offers many possibilities to expand the functionalities of the program such as sensor inputs.
4. The firmware on an external microcontroller offers real-time control of the process that is not straight-forward to implement for software running on a multithread operating system (Windows, Mac OS, Linux, ...).
5. The firmware works independently of the GUI. The microcontroller processes any recipe sent to it via a serial interface.
6. Recipes are created on a mere text basis. This offers a fast way to create, save, and load recipe files but could be more difficult to read than a more graphic representation.

In the following, the concept of the process control is introduced as well as the setup and the graphical user interface. Exemplary material structures are presented, which could be deposited using the program. Furthermore, the realization of the firmware is discussed. We believe that the presented software is useful for many research groups dealing with thin film processing techniques as it enables the development of versatile processes at low costs.

3.3.3 CONCEPT, SETUP, AND GRAPHICAL USER INTERFACE

The main concept of the program relies on the definition of a recipe through a sequence that comprises sequence steps and their repetition. Sequence steps are depicted as successive capital letters (starting from A) and consist of a combination of three basic commands that are as follows:

1. open o[Arduino port]
2. close c[Arduino port]
3. wait w[time in s]

Box brackets followed by a positive integer number n define a repetition, whereas n is the number of repetitions of the enclosed sequence steps. Examples of sequences:

- $[AB]2 = ABAB$
- $[[AB]2C]2 = ABABCABABC$

A full definition of a recipe including the commands of the sequence steps would, for example, be $[AB]2;A = o2, w0.5, c2;B = o3, w2, c3$. Here ports 2 and 3 are opened sequentially for 0.5 and 2 s, respectively, twice. Throughout the paper, an Arduino port being open or closed refers to a voltage of +5 V or 0 V at the port, respectively. Depending on the connection to the port (see Figure 3.3), this leads to the opening or closing of, e.g., a valve.

Figure 3.3 shows a sketch of the setup. The GUI runs on a PC and allows the user to develop, save, and load recipes. During the modification, the total duration of the recipe is automatically calculated. After developing a recipe with the right syntax, the user can execute the recipe. The software will then automatically connect to the Arduino and facilitate a serial connection. The sequence to be executed is sent via this serial connection to the Arduino, and the Arduino confirms the receipt of the sequence, decodes it (i.e., breaks up all the brackets via a recursive function), executes it [i.e., opens (+5 V) or closes (0 V) its ports], and sends a

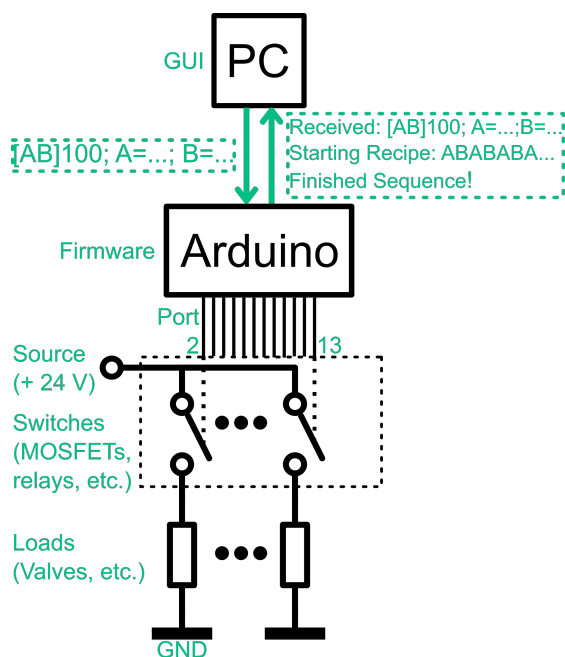


Figure 3.3: Sketch of the overall setup. Communication between the PC and the Arduino is facilitated with the GUI. The digital outputs of the Arduino are connected to switches, which switch the corresponding loads according to the recipe.

message to the PC upon starting a new sequence step. The firmware of the Arduino works independently of the GUI, i.e., any software can make a serial connection to the Arduino and send a recipe to be executed. The output ports of the Arduino are connected to any kind of (fast) switches such as relays or MOSFETs that connect or disconnect the loads to a power supply. Loads for deposition processes include ALD and general gas valves, plasma generators, and gate valves for in situ spectroscopic ellipsometry.⁶⁴

A flowchart with the main process steps upon execution of a recipe is shown in Figure 3.4. The user starts by editing or opening a recipe. The total duration is automatically calculated and displayed. The recipe is checked for syntax errors (such as unclosed brackets), and upon execution, a serial connection to the Arduino is opened. The recipe is sent to the Arduino and the Arduino confirms the start of the recipe. Every time a new sequence step is started, the letter corresponding to this sequence step is sent to the PC, and the current status of the recipe is updated. Upon completion of the recipe, the Arduino sends a message to PC, and the user can start a new recipe. The serial connection is terminated when the GUI is closed.

Figure 3.5 shows a snapshot of the GUI in the recipe mode, which was developed in Python. (1) It marks the status of the serial connection to the Arduino. It will turn from disconnected to connected upon starting a recipe (and change its background color, accordingly). (2) It

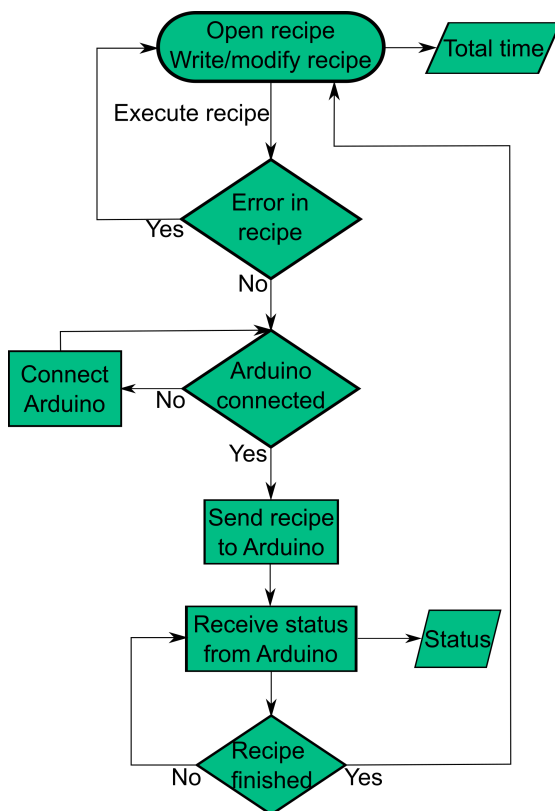


Figure 3.4: Flowchart of the main steps in the recipe mode of the GUI.

marks two textboxes including the strings sent to and received from the Arduino. (3) It marks three buttons for opening, saving, and executing a recipe. (4) It marks two textboxes to modify a recipe. In the upper one, the sequence is defined. In the lower textbox, the sequence steps are defined with the commands `open(o[Arduino port])`, `close(c[Arduino port])`, and `wait(w[time in s])`. The commands are separated by commas, and every sequence step has to be defined in a separate line. Comments can be written with `#[comment]`. (5) It marks the total time of the recipe, which is automatically calculated from the inputs in (4). When the recipe is started, the remaining time and the current status below the executed recipe are shown. The current sequence step is highlighted, and the counter besides a bracket shows how many times the sequence within this bracket has already been executed. Finally, at the bottom of the GUI at (6), a status bar shows information for the user such as errors in the recipe or connection problems to the Arduino.

Another feature of the program is the analysis mode, which can be selected in the tab bar. A screenshot is shown in Figure 3.6. It consists of buttons referring to the Arduino ports. By

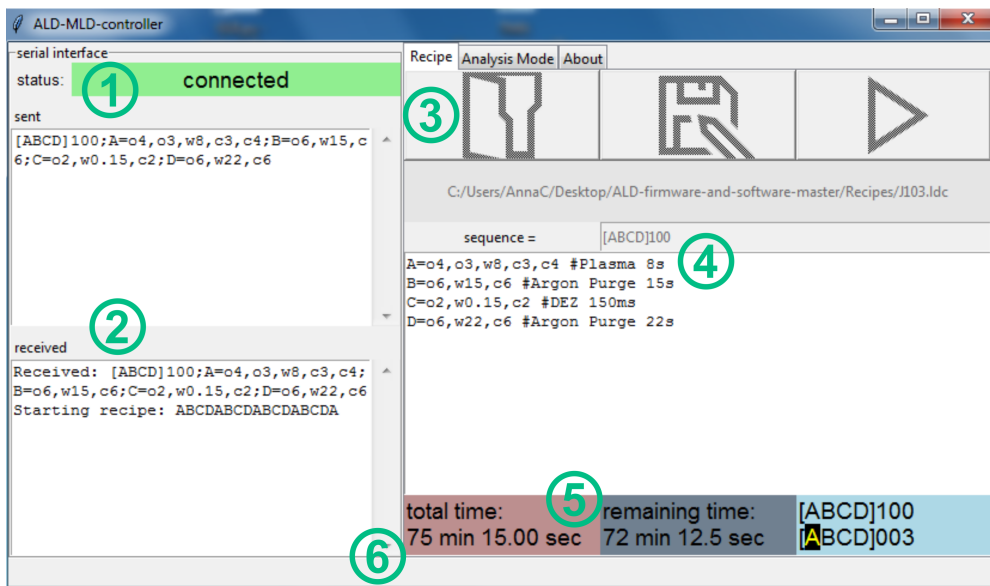


Figure 3.5: Overview of the GUI in the recipe mode. Numbered labels show (1) status of the serial connection to the Arduino (connected/disconnected), (2) commands sent to and received from the Arduino via a serial interface, (3) buttons to load, save, and execute a recipe file, (4) textboxes to define the recipe sequence and sequence components, (5) total and remaining time of the running recipe and current status within the recipe, and (6) a status bar.

clicking on a button, the specific Arduino port will be inverted, thus turning from open to closed or from closed to open. The serial connection to the Arduino is automatically facilitated upon clicking on a button. The buttons are deactivated when a recipe is started in the recipe mode to prevent communication issues.

After introducing the concept of the program, some exemplary processes are shown, which could be easily implemented. The program has already been successfully used for plasma-enhanced atomic layer deposition of ZnO^{65,66,67} and molecular layer deposition of zincone.⁶⁸ Table 3.1 shows possible processes that could also benefit from the versatile opportunities of the program. The underlying syntax for the definition of a sequence makes it possible to implement complex processes such as multilevel laminates in a short and readable way. The table was inspired by the publication of Piercy and Losego.⁵⁹

Furthermore, an exemplary recipe is given for 50 ALD cycles of Al₂O₃ applying trimethylaluminum (TMA) and water, and argon as the purging gas. Let us also assume that for every five cycles of the process, the thickness is measured with in situ spectroscopic ellipsometry⁶⁴ (by opening two gate valves in front of the source and the detector). We assume that the valves controlled by the Arduino outputs are connected in the following way: port 2/ALD valve TMA, port 3/ALD valve H₂O, port 4/ALD valve Ar, port 5, and port 6/gate valves

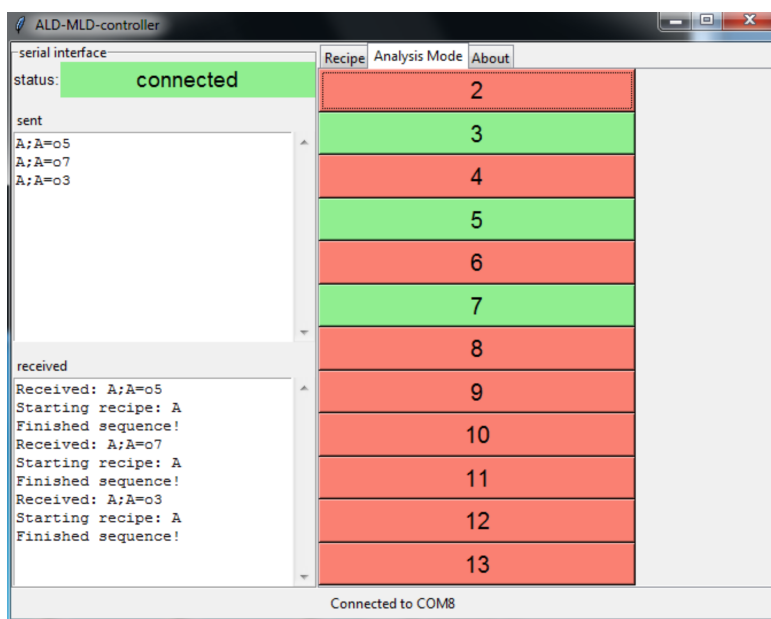


Figure 3.6: Overview of the GUI in the analysis mode. Number of the buttons refers to the output channels of the Arduino and background color to the state of the channel. During the execution of a recipe, the buttons are disabled.



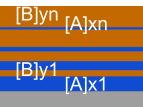
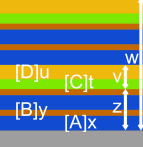
ellipsometry. The recipe then could look like that (assuming dose times of 0.01/10/0.1/20s for TMA/purge/H₂O/purge and measurement time of ellipsometry 10s):

```
sequence = [[ABCD]5E]10
A = 02,w0.01,c2 #TMA dose
B = 04,w10,c4 #Ar purge
C = 03,w0.1,c3 #H2O dose
D = 04,w20,c4 #Ar purge
E = 05,06,w10,c5,c6 #ellipsometry measurement
```

3.3.4 ARDUINO FIRMWARE

After introducing the concept and the implementation of the GUI, the implementation of the Arduino firmware is introduced. This is the part where the actual process control is facilitated. After a serial connection is facilitated with the Arduino, it waits to receive an input. Upon receiving a recipe string, it checks for the correctness of the sequence and the definition of the sequence steps. If everything is correct, an array consisting of the commands of the sequence steps is created and the evaluation of the sequence started. As the sequence should allow an arbitrary level of complexity (i.e., the number of loops over loops, defined in

Table 3.1: Examples of sequences for different material structures.

| Description | Sequence and sketch | Experimental example |
|---------------------------------|---|---|
| Single material | <p>1. [A]_x 2. [AB]_x 3. [ABCD]_x</p> <p>Depending on preferences, either of the three forms can be chosen. For 1, all dosing step and purge steps have to be included in the definition of A; for 2, the half cycles are splitted into two definitions; and for 3, all dosing and purging steps are separately defined. For better readability, form 1 is chosen for the following examples.</p>  | <p>Al₂O₃⁶⁹</p> <p>1. A = TMA dose + purge + water dose + purge 2. A = TMA dose + purge B = water dose + purge 3. A = TMA dose B = purge C = water dose D = purge</p> |
| Basic laminate of two materials | <p>[[A]_x[B]_y]_z</p>  | <p>Al doped ZnO⁷⁰ A = ZnO deposition B = Al₂O₃ deposition</p> |
| Graded laminate | <p>[[A]_{x1}[B]_{y1}]_{z1}[[A]_{x2}[B]_{y2}]_{z2}...[[A]_{xn}[B]_{yn}]_{zn}</p>  | <p>Graded laminates of Al₂O₃ and Ta₂O₅⁷¹ A = Al₂O₃ deposition B = Ta₂O₅ deposition</p> |
| Multilevel laminates | <p>[[[A]_x[B]_y]_z[[C]_t[D]_u]_v]_w</p>  | <p>(La_xSr_{1-x})MnO₃⁷²</p> |

the syntax by box brackets []), the evaluation of the sequence is implemented in a recursive fashion. The complexity of the sequence is hereby only limited by the memory of the microcontroller (which can be extended by switching to, e.g., an Arduino model with enhanced memory). A sketch of the evaluation is shown in Figure 3.7. There is a for-loop that runs over all characters within the sequence string. If the character is an opening bracket “[”, the program looks for the corresponding closing bracket “]” and the number following it (i.e., the number of iterations of the subsequence). A for-loop runs over the number of iterations and calls the recursive evaluation function again, now with the subsequence string (i.e., the string between the opening “[” and closing bracket “]”) as an argument. If the character currently investigated in the for-loop over the sequence string is a top level sequence step letter, i.e., not within brackets, the sequence step is executed and the character is sent via the serial

interface.

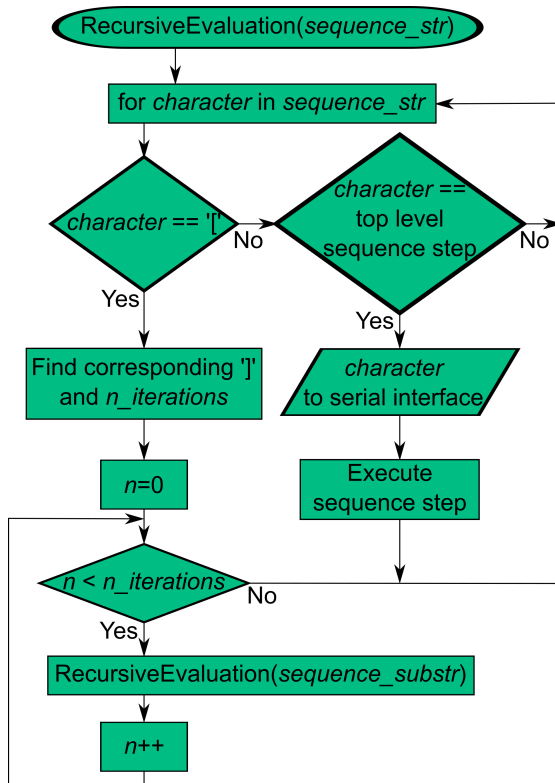


Figure 3.7: Flowchart of the recursive evaluation of a sequence.

Considering the exemplary sequence from above, `[[ABCD]5E]10`, the first character is “[”, therefore, the program, currently at recursion depth 0, calls ten times the function with the substring “[ABCD]5E”. At recursion depth 1, the first character is again “[” and the function is called five times with the substring “ABCD”. Now at recursion depth 2, all characters are top level sequence steps that are executed. After these five repetitions, the program continues at recursion depth 1 at the character “A” of “[ABCD]5E”, which is within brackets and, therefore, is not executed. The next top level character to be executed is “E”, after which the program continues at recursion depth 0 at the character “A” of `[[ABCD]5E]10`, which again is not top level.

This execution of the recipe with the microcontroller offers on the one hand independency from the software sending the recipe string via a serial connection (any rudimentary terminal software could be used to send recipes, and thus it is operating system independent). On the other hand, it allows quasi real-time execution of the sequence steps, often needed in the fast switching of valves in ALD processes. Figure 3.8 shows the switching of an output channel

of the Arduino in different time scales occurring in sequential processes. In Figures 3.8(a) and 3.8(b), a repetition of 1 ms and 100 s pulses is shown, respectively, demonstrating the possibility of the exact timing of very short and very long pulses. Figure 3.8(c), furthermore, shows 1 ms pulses with a 1 s delay in-between, and 3.8(d) shows a magnification of the 1 ms pulse.

Figure 3.9 shows the application of short pulses for switching an ALD valve (Swagelok ALD3) to introduce diethylzinc (DEZ) into a vacuum reactor. Figure 3.9(a) shows the pressure increase in the reactor (measured by an MKS Baratron 262B pressure gauge and readout by an external software) with different valve opening times, offering the possibility to introduce discriminable low doses of DEZ. Figure 3.9(b) shows that the lowest dose possible with the setup (5 ms valve opening) can be introduced repetitively, without fluctuations in the dose.

3.3.5 SUMMARY AND CONCLUSIONS

In this note, a GUI and firmware implementation of a control software for sequential processing techniques is presented. The GUI allows to create, modify, and save recipes, facilitates the communication with the processing hardware, and shows the current status of a running recipe. Recipes are based on the definition of a sequence including the repetition of sequence steps that are defined with combinations of three basic commands. The processing of recipes with the firmware in a recursive fashion allows an almost indefinite level of complexity of the recipes (only limited by the microcontroller memory) and a quasi real-time processing of such. Furthermore, only open-source software and hardware are used in this implementation. Thus, the versatility and low costs of our approach allow scientists to expand their research on creating complex material structures for a wide range of applications.

3.3.6 ACKNOWLEDGMENTS

This project has received funding from the European Research Council (ERC) under the European Union's Horizon 2020 research and innovation program (Grant Agreement No. 715403). The authors thank Peter Luidolt for his valuable inputs and suggestions.

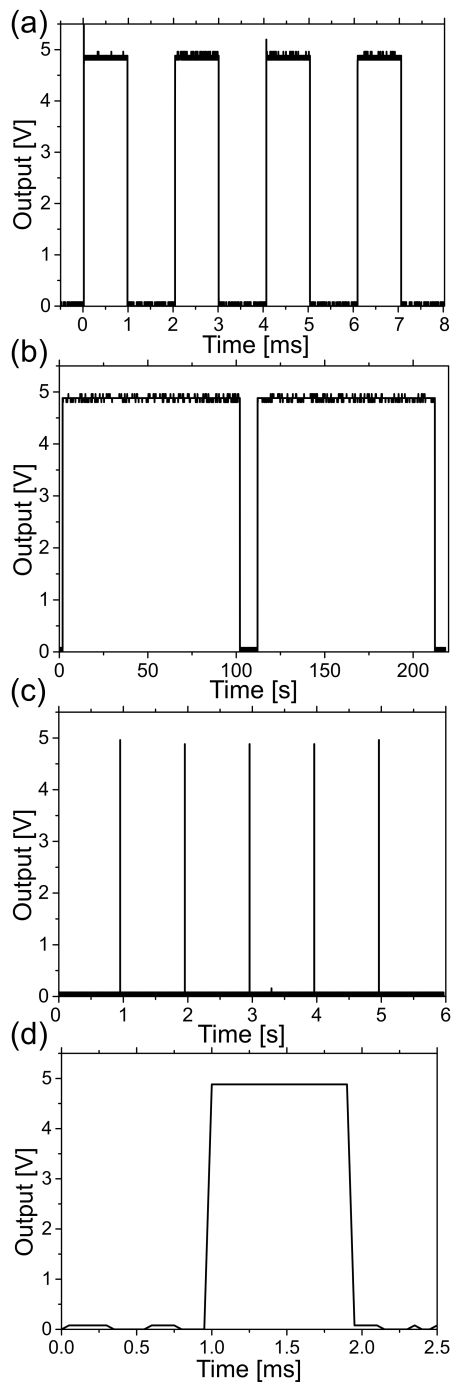


Figure 3.8: Output voltage of an Arduino channel upon receiving different sequences from the GUI. The sent sequences are (a) channel 1 ms open, 1 ms closed; (b) channel 100 s open, 10 s closed; and (c) channel 1 ms open, 1 s closed. (d) Shows a magnification of the 1 ms pulse in (c). Note that for performing several thousand repetitions of the sequence in (a), sending of the sequence step via the serial connection had to be deactivated in the firmware.

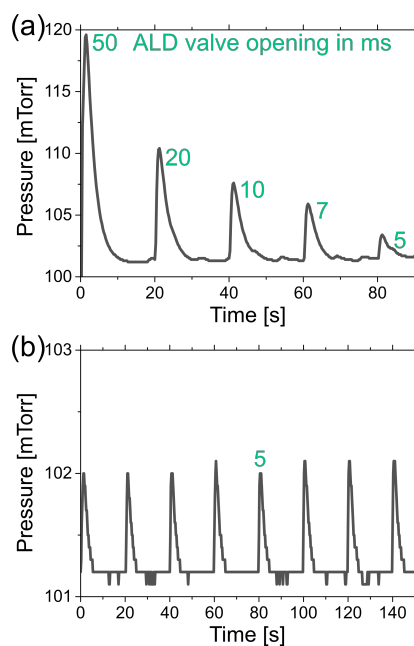


Figure 3.9: Pressure increase during dosing of DEZ every 20 s with (a) different ALD valve opening times and (b) 5 ms ALD valve opening time. A constant flow of 20 sccm Ar was present for all doses and constituted the baseline pressure of around 101 mTorr. 5 ms was the shortest possible opening time; for shorter signals, the ALD valve did not open and no pressure increase was observable. Considering a readout period of the pressure of 0.25 s, the differences in peak heights in (b) are negligible.

4

Thin Film Analysis

Analysis of the properties of the thin films is essential to confirm if a deposition was successful or if deposition parameters need to be changed to meet the specific purpose. This chapter gives an introduction to the most often used or special techniques for analyzing the thin films within this thesis.

4.1 SPECTROSCOPIC ELLIPSOMETRY

In spectroscopic ellipsometry (SE), the reflection of light from a sample and the consequential change of polarization of the light is utilized to obtain thickness and optical constants from a thin film.⁷³ The polarization of a light wave can be described by the superposition of electric field vectors oscillating within the plane of incidence (\mathbf{E}_p) and normal to it (\mathbf{E}_s) (i.e. p and s polarization, respectively). In SE, the incident light wave is linearly polarized, i.e. the phase difference between \mathbf{E}_p and \mathbf{E}_s is zero. Upon reflection from the sample, the polarization state, i.e. the amplitudes of \mathbf{E}_p and \mathbf{E}_s and their phase difference, change and the wave is elliptically polarized. This change of polarization is measured with SE as a function of wavelength and can be written as:

$$\rho = \tan(\psi) \exp(i\Delta) = \frac{r_p}{r_s} \quad (4.1)$$

where ψ is the amplitude ratio and Δ the phase difference of p and s components, and

$r_p = \frac{E_{rp}}{E_{ip}}$ and $r_s = \frac{E_{rs}}{E_{is}}$ the ratios of reflected to incident electric field components. The Fresnel equations relate these ratios to the optical constants of the media at which reflection occurs (n_i and n_t) and the incident (θ_i) and refracted (θ_t) angle:

$$r_p = \frac{E_{rp}}{E_{ip}} = \frac{n_t \cos \theta_i - n_i \cos \theta_t}{n_t \cos \theta_i + n_i \cos \theta_t} \quad (4.2)$$

$$r_s = \frac{E_{rs}}{E_{is}} = \frac{n_i \cos \theta_i - n_t \cos \theta_t}{n_i \cos \theta_i + n_t \cos \theta_t} \quad (4.3)$$

These equations also hold for the complex refractive index $N = n - ik$, where k is the extinction coefficient, and can be rewritten to eliminate θ_t by applying Snell's law ($n_i \sin \theta_i = n_t \sin \theta_t$). Thus, the measurement of ψ and Δ (and consequently r_p and r_s) in an SE measurement, contains information about the optical constants n and k . Furthermore, by considering interference effects of waves reflected from the surface and backside of a layer, information about the thickness can be gained. And all of these considerations can be applied to multi-layer systems, in which reflection and refraction has to be considered for every interface.

If the optical constants of a material are known, the thickness is easily obtained from an SE measurement (considering a transparent film or a thin absorbing film). In the case of unknown optical constants, a model, containing different fit parameters, has to be applied and the fit parameters are fitted to best describe the measurement. For films, which are transparent in at least parts of the measured spectrum, the Cauchy model can be applied:

$$n(\lambda) = A + \frac{B}{\lambda^2} + \frac{C}{\lambda^4}, \quad k = 0 \quad (4.4)$$

where n is the refractive index, A , B , and C are the fit parameters, λ is the wavelength of the light, and k is the extinction coefficient. For small absorptions near the bandgap, the model can be extended by the so-called Urbach tail

$$k(E) = D \exp((E - E_g)/E_u) \quad (4.5)$$

where k is the extinction coefficient, D is a fit parameter, E is the energy of the light, E_g is the bandgap energy, and E_u the Urbach energy (which is also often fitted). In this thesis, this is the mostly used model (with and without the Urbach extension) for extracting ZnO thickness and optical constants. Hereby, ZnO is deposited on an semi-infinite Si wafer with native oxide, whereas the optical constants of the Si and its native oxide are well known.

4.2 X-RAY DIFFRACTION

X-ray diffraction is used for the structural investigation of crystalline materials.⁷⁴ Diffraction occurs when the wavelength of the radiation, which impinges on a structure, is in the order of the periodicity of structural elements. For crystals and molecules, the interatomic spacing is in the order of a few Å, i.e. falls in the wavelength range of X-rays. Thus, by radiating crystalline materials with X-rays, interference effects will become observable. In X-ray diffraction, the elastic scattering of X-rays (Thomson scattering) is investigated, i.e. the wavelength of the X-rays is conserved.

The most widely used instrument to measure diffraction in (polycrystalline) thin films is the $\theta/2\theta$ diffractometer. A sketch of the experimental geometry is shown in Figure 4.1. In a $\theta/2\theta$ scan, an X-ray beam with wavevector \mathbf{K}_0 is directed under an angle θ onto the sample. The scattered beam \mathbf{K} is probed at the same angle θ , i.e. the angle between source and detector is always 2θ . In the scan, the angle θ is varied and maxima in the intensity can be observed when the Bragg condition is met:

$$2d_{hkl} \sin(\theta_B) = \lambda \quad (4.6)$$

where d_{hkl} is the spacing of lattice planes with Miller indices hkl , θ_B the angle at which maximum intensity is observed (Bragg angle), and λ the wavelength of the X-ray beam.

As the angle θ between incoming and outgoing beam is always the same, the scattering vector $\mathbf{Q} = \mathbf{K} - \mathbf{K}_0$ is always normal to the sample surface. I.e., only lattice planes which are parallel to the sample surface can be probed. In a polycrystalline sample, crystallites are randomly oriented and therefore several Bragg peaks, stemming from crystallites having lattice planes parallel to the surface, will be observed in the scan. If the sample is textured, i.e. the crystallites have a preferential orientation, only some of the Bragg peaks will be observable.

4.2.1 GRAZING INCIDENCE X-RAY DIFFRACTION

The penetration depth of X-rays (i.e. the inverse of the X-ray attenuation coefficient μ) is in the order 10-100 μm .⁷⁴ As the thickness of the investigated thin films is often much less, a large fraction of the diffracted signal stems from the substrate. Thus, the path of the X-ray in the sample is often too small to deliver peaks with sufficient peak-to-noise ratio. In grazing incidence X-ray diffraction (GIXD), the angle of the incoming beam with respect to the sample surface is fixed to a small angle α of a few degrees or less. This allows the X-rays to

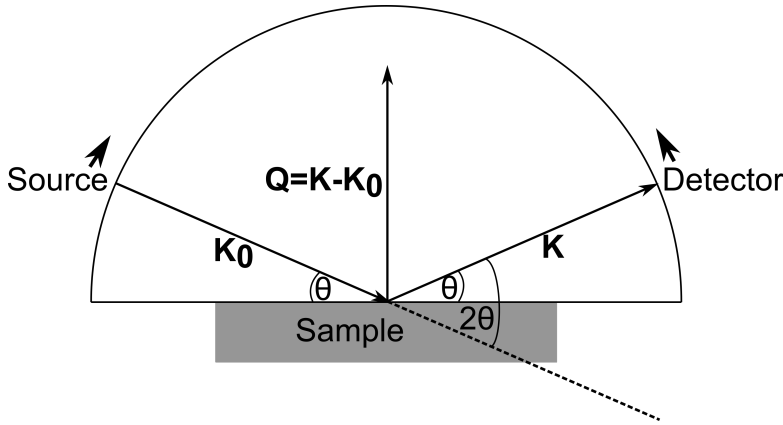


Figure 4.1: Schematic of a $\theta/2\theta$ diffractometer. Figure adapted from Birkholz.⁷⁴

travel an increased path of $l = t / \sin \alpha$ within the film for small angles. In GIXD, the setup is not in a symmetric geometry as for the $\theta/2\theta$ -diffraction as the incoming angle α is fixed. This means that the angle of the scattered beam is now $2\theta - \alpha$ and the orientation of the scattering vector \mathbf{Q} changes during the measurement, i.e. it does not consist only of a component normal to the substrate surface but also an in-plane component, which means that information about the in-plane orientation of crystallites can be gained. The GIXD measurements within this thesis have been performed at the XRD-1 beamline at the synchrotron Elettra, Trieste, Italy.⁷⁵ Here, high-intensity synchrotron radiation is used, and a large scale 2D-detector allows for the simultaneous detection of different scattering angles.

4.3 X-RAY REFLECTIVITY

The refractive index of a material for X-rays deviates from unity in the following form:⁷⁴

$$N = 1 - \delta - i\beta \quad (4.7)$$

where N is the complex refractive index, δ depends on the density and composition of the material, and β is related to the attenuation coefficient by $\beta = \frac{\lambda}{4\pi}\mu$. In X-ray reflectivity (XRR), the setup is in a $\theta/2\theta$ -configuration (see Figure 4.1). However, the experiment is usually performed at much smaller angles than in XRD and is based on reflection and refraction. From a derivation of Fresnel coefficients, the ratio of reflected and incident intensity I_R/I_0 as a function of incident angle θ is

$$\frac{I_R}{I_0} = \left| \frac{\theta - \sqrt{\theta^2 - \theta_C^2 - 2i\beta}}{\theta + \sqrt{\theta^2 - \theta_C^2 - 2i\beta}} \right|^2 \quad (4.8)$$

in which $\theta_C = (2\delta)^{1/2}$ is the critical angle. For $\theta < \theta_C$ the reflectivity is nearly constant and total reflection of the incident beam occurs. For $\theta > \theta_C$, the reflected intensity strongly decreases over several orders of magnitude. The intensity is therefore plotted on a logarithmic scale. The positive and negative interference between the reflected and refracted beams furthermore leads to the occurrence of periodic maxima and minima, so-called Kiessig fringes. The periodicity of these scales with the film thickness.

By measuring and fitting the reflected intensity as a function of θ , the complex refractive index as well as the thickness and roughness can be obtained. The complex refractive index components furthermore give information about the density, composition, and attenuation of the material.

4.4 PIEZOELECTRIC CHARACTERIZATION

Parts of this thesis deal with the piezoelectric properties of ZnO thin films. The piezoelectric properties can on the one hand be characterized microscopically by a variant of atomic force microscopy, namely piezoresponse force microscopy. This is useful for investigating in depth the response of different crystallites and the influence of process parameters on the thin film morphology and crystalline properties. On the other hand, a macroscopic characterization, by stimulating a large thin film area, is important for characterizing the performance of the thin film in a device structure.

4.4.1 PIEZORESPONSE FORCE MICROSCOPY

In atomic force microscopy (AFM), the force between a sharp tip and a surface is measured.⁷⁶ When the tip approaches the surface very closely, interatomic repulsive forces occur. The tip is mounted on a soft cantilever which deflects upon application of forces on the tip. By moving the tip across the surface and measuring the deflection of the cantilever (usually by optical methods), imaging of the surface topography can be achieved. The AFM can be operated in different modes, the constant force mode and the constant height mode. In constant force mode, the cantilever deflection (i.e. the force) is kept constant by moving the sample in vertical direction and thus following the topographical features. In constant height mode, the

vertical position of the sample is kept constant and the change of deflection of the cantilever is monitored. This mode has to be used carefully as the tip might crash into features of the sample which may lead to damages in the sample. A mode with gentler condition is the tapping mode. Here, a piezo oscillator drives the cantilever with the tip close to its resonance frequency. Thus there is only intermittent contact between tip and sample surface and topographic information is gained from the amplitude signal of the cantilever.

In piezoresponse force microscopy (PFM), the indirect piezoelectric effect is used to analyze the piezoelectric response of a sample.^{77,78} In the indirect piezoelectric effect, the strain S_j can be written as⁷⁸

$$S_j = d_{ij}E_i \quad (4.9)$$

where d_{ij} are the components of the piezoelectric tensor and E_i the applied electric field. For the application of an electric field parallel to the polarization direction the strain can be written as

$$S = \frac{\Delta Z}{Z} = \pm d_{33}E \quad (4.10)$$

where ΔZ is the sample deformation and Z the sample thickness. By dividing both sides by Z , this results in

$$\Delta Z = \pm d_{33}V \quad (4.11)$$

where V is the applied voltage across the sample. The \pm sign corresponds to polarization parallel or antiparallel to applied voltage, respectively.

A PFM-setup is an extension of an AFM, where a conductive tip is used to apply a voltage to induce a deformation in piezoelectric domains and simultaneously measures the deformation in contact mode. The substrate usually serves as the ground electrode. As the piezoelectric coefficient for many materials is in the order of dozens to hundreds pm/V, the typical application of a few volts leads to a displacement in the *pm* range (see equation 4.11). Such a small displacement is often smaller than the surface roughness and thus difficult to detect statically. To increase the sensitivity, one uses an ac-modulated voltage $V = V_0 \cos(\omega t)$ and detects the cantilever vibrations by lock-in amplifying techniques. By scanning the surface and measuring the vibrations of the cantilever, one can therefore obtain a map of the piezoresponse. The first harmonic surface vibration hereby is⁷⁸

$$\Delta Z = \Delta Z_0 \cos(\omega t + \varphi) \quad (4.12)$$

where $\Delta Z_0 = d_{eff}V_0$ is the vibration amplitude, d_{eff} the effective piezoelectric constant, and φ the phase difference between applied voltage and piezoresponse. The phase difference gives information about the polarization direction of the domains, i.e. $\varphi = 0^\circ$ for polarization parallel to the voltage and $\varphi = 180^\circ$ for polarization antiparallel to the voltage.

In piezoelectric samples, the deformation is not necessarily parallel to the applied voltage. Lateral (in-plane) deformation can occur, which leads to a buckling or torsion of the cantilever compared to deflection for out-of-plane deformation. To distinguish all these different deformations of the cantilever, images have to be obtained at different rotation stages of the sample ($0^\circ, 90^\circ, 180^\circ$). From this, the full out-of-plane and in-plane piezoresponse can be obtained.

4.4.2 MACROSCOPIC CHARACTERIZATION

In PFM, one makes use of the indirect piezoelectric effect, in which an electric field is applied to cause a strain in the material. The response is on the one hand dynamical, as an ac-field is applied and is on the other hand obtained on a microscopic scale, down to individual crystallites.

In the direct piezoelectric effect, discovered by Pierre and Jaques Curie in 1880,⁷⁹ the application of a stress on a piezoelectric material leads to a polarization within the material due to separation of the negative and positive charge centers. This can be written as⁸⁰

$$P = d\sigma \quad (4.13)$$

where P is the polarization, d the piezoelectric coefficient, and σ the applied stress. This polarization leads to the development of charges with opposite sign on the material's surfaces.⁸⁰ By sandwiching the material between two electrodes and shortcircuiting the two electrodes, the free charges of the electrodes will flow toward the surface charges with opposite sign. Thus, by application of a force on the piezoelectric material, an external current peak can be detected, which quickly diminishes upon full screening of the surface charges. By releasing again the force, a current will flow with the same magnitude in the opposite direction. By integrating this current over time, the created surface charges $Q = \int Idt$ can be obtained, and from this, the piezoelectric coefficients.

Part II

Plasma-Enhanced Atomic Layer Deposition of ZnO

5

Tuning of Material Properties of ZnO Thin Films grown by Plasma-Enhanced Atomic Layer Deposition at Room Temperature

5.1 PREFACE



Tuning of material properties of ZnO thin films grown by plasma-enhanced atomic layer deposition at room temperature

Cite as: J. Vac. Sci. Technol. A **36**, 01A109 (2018); <https://doi.org/10.1116/1.5003334>
Submitted: 05 September 2017 . Accepted: 06 November 2017 . Published Online: 04 December 2017

Julian Pilz, Alberto Perrotta, Paul Christian, Martin Tazreiter, Roland Resel, Günther Leising, Thomas Griesser, and Anna Maria Coclite

COLLECTIONS

Paper published as part of the special topic on [2018 Special Collection on Atomic Layer Deposition \(ALD\)](#)

 This paper was selected as an Editor's Pick

The work was conducted at Graz University of Technology and collaboration with Thomas Griesser of University of Leoben. The author of the thesis performed sample preparation,

characterization except for XPS and GIXD, data evaluation and wrote the manuscript. Alberto Perrotta, Paul Christian, and Martin Tazreiter supported the experimental setup, Roland Resel supported analysis of X-ray data, Günther Leising supported analysis of optical data, Thomas Griesser performed XPS measurements, and Anna Maria Coclite supervised the work and supported data analysis. All authors reviewed the manuscript. The following text and images are identical to the published work:

- Pilz, J.; Perrotta, A.; Christian, P.; Tazreiter, M.; Resel, R.; Leising, G.; Griesser, T.; Coclite, A. M. Tuning of Material Properties of ZnO Thin Films Grown by Plasma-Enhanced Atomic Layer Deposition at Room Temperature. *J. Vac. Sci. Technol. A Vacuum, Surfaces, Film.* **2018**, *36* (1), 01A109

The results of the published manuscript are in most parts also included in the Master's thesis (Pilz, J. Plasma-enhanced atomic layer deposition of zinc oxide thin films. Master's thesis, Graz University of Technology, 2017) of the author of this thesis. As the manuscript presents a good basis for the other experimental parts of this thesis, it is nonetheless included here.

5.2 ABSTRACT

The ability to grow inorganic thin films with highly controllable structural and optical properties at low substrate temperature enables the manufacturing of functional devices on thermo-sensitive substrates without the need of material postprocessing. In this study, the authors report on the growth of zinc oxide films by direct plasma-enhanced atomic layer deposition at near room temperature. Diethyl zinc and oxygen plasma were used as the precursor and coreactant, respectively. The process was optimized with respect to the precursor and coreactant dosing as well as to the purging times, which ultimately resulted in saturated atomic layer deposition growth. The so-obtained films exhibit a polycrystalline pattern with a (100) texture and low amount of incorporated carbon. Furthermore, the possibility to tune crystallite size, refractive index, and bandgap of the films by adapting the plasma radio-frequency power is demonstrated.

5.3 INTRODUCTION

Zinc oxide (ZnO) is a wide direct band gap semiconductor ($E_g \sim 3.3$ eV) with attractive optoelectronic and piezoelectric properties.⁸¹ These properties are essential for various applications such as solar cells,^{82,83,84} transparent conductive oxide layers,^{85,86,87,88} piezoelectric

nanogenerators,^{57,89,90,91} and gas sensors.^{92,93,94} The ability to tune optical and structural properties of the zinc oxide films is crucial for adapting the material characteristics to meet device requirements (i.e., enhanced device efficiency or sensitivity).^{56,95,96} Furthermore, the application of ZnO on thermo-sensitive substrates such as polymers^{69,97,98} and biomaterials^{99,100} requires deposition processes operating at low temperatures which should be well below the glass transition temperature of polymers and temperatures that would lead to, e.g., degradation of the biomolecules. ZnO films can be grown at substrate temperatures around room temperature by techniques such as RF magnetron sputtering,¹⁰¹ pulsed-laser deposition,¹⁰² and atomic layer deposition (ALD).⁸¹ Tuning of structural and optical properties of the films deposited by these techniques can be achieved by modifying deposition parameters such as RF-power, oxygen pressure, and substrate temperature. Among other techniques, ALD is the method of choice for the deposition of high-quality conformal layers with Å-level thickness control.^{81,4} The growth mechanism is composed of the sequential exposure of the substrate to two (or more) precursors, separated by an inert gas purge. The self-limiting nature of the reactions on the surface offers the possibility for atomic layer precision with a typical growth per cycle (GPC) in the Å/cycle range. The process cycle is repeated until the desired thickness has been achieved. An ALD process in which the surface reactions are driven by thermal energy is called thermal ALD. Typical thermal ALD of ZnO utilizes diethyl zinc (DEZ) and water as the reactants and shows an ALD window (in which the GPC with respect to temperature is fairly constant) of around 110–170 °C.⁸¹ A variation of ALD that allows lower deposition temperatures to be achieved is plasma-enhanced atomic layer deposition (PE-ALD). In this case, reactive plasma species are used as coreactants.⁶ By controlling the plasma process parameters (e.g., pressure, gas composition, and plasma power density), PE-ALD allows material properties to be further tuned. Several groups have been investigating the material properties and growth behavior of ZnO films grown by PE-ALD adopting DEZ as the metal precursor, and oxygen or water-fed plasmas as oxidative coreactants.^{81,103,104,105,106,107,108} A wide range of GPC values has been obtained, spreading from 1.5 to 3 Å/cycle at substrate temperatures of 75–300 °C. The GPC values are clues for different growth mechanisms which cannot be associated with pure ALD growth. It has been reported that the reason behind the variation of the ZnO growth characteristics could be attributed to precursor decomposition effects at substrate temperatures above 60 °C, leading to non-self-limiting growth.¹⁰⁹ Thus, besides the possibility to deposit on thermo-sensitive substrates, depositions which take place below this temperature are highly desired in order to achieve controlled growth and process conditions. Room temperature deposition of ZnO

has been investigated both with thermal and plasma ALD. The growth of zinc oxide at 25 °C by PE-ALD has been reported using dimethyl zinc (DMZ) as the metal precursor, resulting in a GPC of 1.6 Å/cycle.¹¹⁰ The films are polycrystalline with a preferential (100) orientation and show hydroxyl and bidentate impurities, which are diminished with temperature. Also, thermal ALD of ZnO at 23 °C has been reported using DEZ and water as the metal precursor and coreactant, respectively, resulting in polycrystalline films with a (002) preferential orientation and a GPC of around 0.85 Å/cycle.¹¹¹ Films grown at 40 °C show an average carbon content of 1.1 ± 0.3 at.% and a Zn/O ratio of 0.76 ± 0.14 in this study. However, to the authors' knowledge, no previous results have been reported for depositions near room temperature by applying DEZ and O₂-plasma. This low substrate temperature makes it possible to process thermo-sensitive substrates and prevents decomposition effects of the precursor so that controlled ALD-growth can be achieved. Furthermore, in this contribution, the tuning of ZnO properties has been investigated. In the literature, tuning of structural, optical, and electrical properties has been achieved by modifying process parameters such as substrate temperature,^{104,105} O₂-plasma dose,¹⁰⁵ or introducing additional process steps.^{112,113} In this study, we investigated the influence of RF-power on the structural and optical properties of the ZnO films and demonstrate a simple approach to tune the crystallite size, refractive index, extinction coefficient, and bandgap for PE-ALD at room temperature.

5.4 EXPERIMENT

A custom-built direct plasma ALD reactor was used to deposit ZnO thin films on single side polished silicon (100) substrates with a native oxide layer. Prior usage, the substrates were rinsed with isopropyl alcohol and subsequently dried under a CO₂ stream. The reactor was in an asymmetrical plate configuration, in which the showerhead radio frequency (RF) electrode and ground electrode have a clearance of 4 cm and are 20 and 30 cm in diameter, respectively. DEZ (Sigma-Aldrich) was used as the metalorganic precursor. The input power was supplied by an RF-power generator (Advanced Energy Cesar 13.56 MHz) through a matching network (Advanced Energy Navio). The pump system consisted of a turbomolecular pump (Pfeiffer vacuum TMH071P) and a rotary vane pump (Pfeiffer vacuum DUO5M). The pressure in the reactor was controlled via a butterfly valve (MKS 253B). The valve was set to a fixed opening in order to reach a pressure of around 100 mTorr during plasma exposure. A multi gas controller (MKS 647C) and mass flow controllers (MKS MF1-C) were used to control the flow rates of the gases. Pure oxygen was used during the plasma step and

Ar was adopted in the purging step. The flow rates for O₂ and Ar were set at 20 sccm during the plasma and the purging step, respectively. An ALD-valve (Swagelok ALD3) was used to pulse DEZ into the reactor. Due to the high vapor pressure of DEZ, no further heating or bubbling system was adopted. One cycle in the ALD process consisted of (1) O₂-plasma dose, (2) Ar purging, (3) DEZ dose, and (4) Ar purging. The process was started with O₂-plasma dose in order to activate the surface. Prior to the plasma exposure, a 10 s O₂ flow stabilization step was introduced to have a constant pressure when igniting the plasma. All depositions were carried out at a floating substrate temperature. The GPC for each deposition was determined by taking the mean value of the layer thickness of two or more samples which were put on different positions in the reactor and dividing it by the number of ALD cycles. Spectroscopic ellipsometry (J.A. Woollam M-2000V) was used to determine the thickness and optical properties of the films. The measurements were carried out at three different incidence angles (65°, 70°, and 75°) in a wavelength range from 370 to 1000 nm. To determine ZnO layer thicknesses, experimental data were modeled in the ZnO transparent region from 450 to 1000 nm with the completeease software. For this, a three-layer optical model was fitted to the data, consisting of silicon substrate, native silicon oxide layer (fixed thickness of 1.5 nm), and a Cauchy top layer, which accounts for the ZnO. In the Cauchy model, the dispersion relations between the refractive index n and the wavelength λ , as well as between the extinction coefficient k and the energy of the incoming light E , are given by

$$n(\lambda) = A + B/\lambda^2 + C/\lambda^4 \quad (5.1)$$

$$k(E) = k_0 \times e^{D \cdot (E - E_{Bandedge})} \quad (5.2)$$

Here, the variables A , B , C , as well as k_0 and D are fit parameters, while the constant $E_{Bandedge}$ denotes the band edge energy. As parameter C was found highly correlated to parameter B , this parameter was set to 0. In order to investigate bandgap and near-bandgap absorption, an oscillator model was employed instead of the Cauchy model, fitting the dielectric function over the whole (experimental) spectral range. The oscillator model consists of a Gaussian oscillator to account for high-energy contributions, a PSEMI-Mo model to account for near-bandgap absorption, and another Gaussian oscillator for the near-infrared region.¹¹⁴ The PSEMI-Mo model is an oscillator with a sharp onset and Kramers–Kronig consistent properties consisting of four connected polynomial spline functions. It is modeled by fit parameters controlling the amplitude, broadening, center energy, left and right endpoints, and left and right midwidth control points.¹¹⁵ The bandgap energy was obtained by extrapolat-

ing the linear part from a $(\alpha h\nu)^2$ vs. $h\nu$ plot to intersect the energy axis (Tauc-plot),¹¹⁶ in which α is the absorption coefficient, h is Planck's constant, and ν is the photon's frequency. The absorption coefficient α was calculated from the measured extinction coefficient k using $\alpha = 4\pi k/\lambda$.¹¹⁷ UV-Vis spectroscopy (Shimadzu UV-1800) was used to measure the absorbance of the film deposited on glass in a wavelength range from 190 to 1000 nm and extract the bandgap energy via Tauc fitting. Contributions from reflections were neglected in the analysis. X-ray diffraction (XRD) in a θ/θ -configuration was performed to analyze the crystalline properties of the films along the specular direction. The diffractometer (Panalytical Empyrean) utilized radiation of a copper tube monochromatized with a layered x-ray mirror ($\lambda = 1.5418 \text{ \AA}$) and a PIXcel3D-detector which was operated in 1D-mode. A $1/8^\circ$ divergence slit, a 10 mm mask, and a P7.5 antiscatter slit were used in the setup. Additionally, films were grown on glass substrates and investigated by XRD. Grazing incidence X-ray diffraction (GIXD) was performed to investigate the in-plane orientation of the crystallites. The measurements were conducted at the Elettra XRD1-beamline in Trieste, Italy. The incident angle α was set between 1.2° and 2° for optimal signal strength and the wavelength λ of the primary beam was either 1 or 1.4 \AA . Diffracted intensities were collected on a Pilatus 2M detector and all data have been recalculated to (wavelength-independent) reciprocal space maps utilizing the xrayutilities library for python.¹¹⁸ The atomic concentration and oxygen binding state were determined by X-ray photoelectron spectroscopy (XPS) using a Thermo Scientific instrument equipped with a monochromatic Al- K_α x-ray source (1486.6 eV). High-resolution scans were acquired at a pass energy of 50 eV and a step size (resolution) of 0.1 eV. Survey scans were acquired with a pass energy of 200 eV and a step size of 1.0 eV. Photoelectrons were collected using a take-off angle of 90° relative to the sample surface. Charge compensation was performed with an argon flood gun. All analyses were performed at room temperature. For each sample, two different spots were analyzed in pristine conditions and after sputtering with Ar ions. The sputtering was performed at 2000 eV for 5 s. The atom fractions calculated from the XPS survey scans on the two spots were used to calculate average atomic percentages.

5.5 RESULTS AND DISCUSSION

5.5.1 DETERMINATION OF SATURATION REGIMES

In order to ensure self-limited ALD growth and to avoid a chemical vapor deposition (CVD)-like growth mode, each of the four steps in an ALD cycle has to be saturated; that is, the

Table 5.1: Parameters of the deposition series performed in order to determine the saturation regimes.

| Series | DEZ dose / s | Purge after DEZ dose / s | Plasma dose / s | Purge after plasma dose / s |
|--------|--------------|--------------------------|-----------------|-----------------------------|
| A | 0.31-0.40 | 15 | 15 | 15 |
| B | 0.32 | 15 | 1-40 | 15 |
| C | 0.32 | 2-15 | 3 | 15 |
| D | 0.32 | 5 | 3 | 5-15 |

precursor and plasma exposure time should be sufficient to react with all available surface sites, and the purging steps need to effectively remove unreacted precursor molecules, byproducts, and oxidizing species, in order to avoid reactions in the gas phase.⁴ In order to minimize the overall processing time, it is desired to operate all four cycles at the minimum time required to obtain saturated growth. The deposition series reported in Table 5.1 were performed in order to determine the individual saturation regimes.

The recipe optimization was performed at RF-power of 100 W for 100 ALD cycles. GPC as a function of the four ALD-cycle parameters is shown in Figure 5.1.

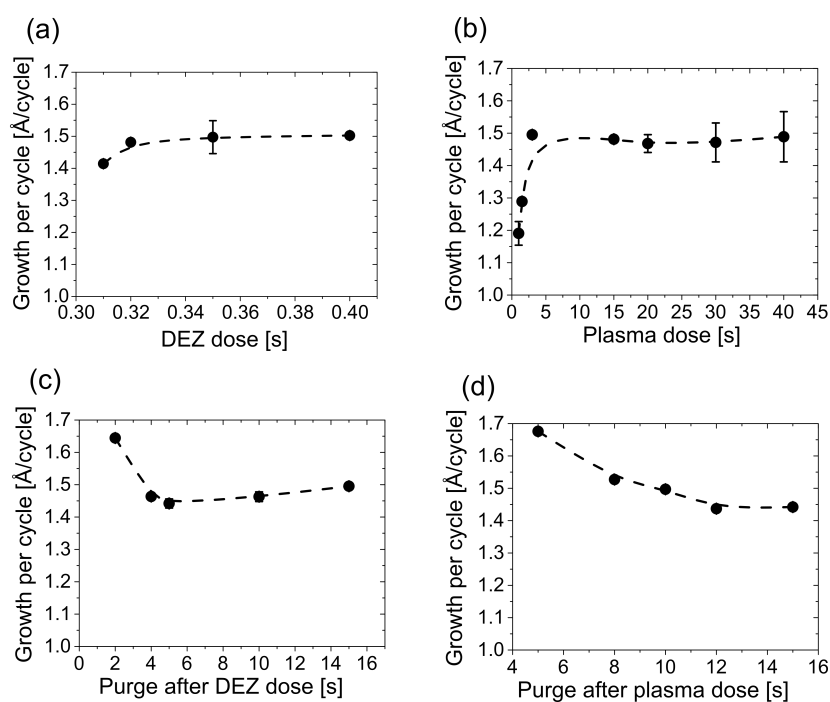


Figure 5.1: Growth saturation curves with respect to (a) precursor (DEZ) dose, (b) plasma dose, (c) purging after precursor dose, and (d) purging after plasma dose. Broken lines serve as a guide to the eye. The error bars are plotted for each data point but are within the marker size in most cases.

The GPC with respect to the DEZ dose saturates at 0.32 s [Figure 5.1(a)]. For shorter

precursor dosing, the amount of DEZ-molecules is not sufficient to fully react with the available reactive sites. The GPC with respect to the plasma dose increases with increasing plasma doses and saturates at 3 s [Figure 5.1(b)]. Below 3 s, the plasma dose is in an unsaturated regime and thus does not fully remove the organic ligands from the surface reacted DEZ molecules, limiting the growth. On the other hand, plasma doses above 15 s lead to inhomogeneous growth within our setup, which could be due to heating effects of the spatially inhomogeneous plasma leading to different substrate temperatures. The GPC with respect to the purging after the DEZ exposure decreases when the purging time is increased and saturates at 5 s [Figure 5.1(c)]. Below 5 s, the purging time is insufficient to completely remove the unreacted DEZ molecules and reaction by-products, leading to an undesired CVD-like growth of the film. The GPC with respect to the purging after plasma dose also decreases with increasing purging time and saturates at a purging time of 12 s [Figure 5.1(d)]. In summary, the optimum recipe in which the GPC saturates for all four partial steps of the ALD cycle with the minimum process time is 0.32 s DEZ dose/5 s Ar purge/3 s O₂-plasma dose/12 s Ar purge. The resulting GPC is ~1.5 Å/cycle, which is comparable to reported values for the GPC of PE-ALD ZnO films using DEZ and O₂-plasma at the lowest temperatures investigated^{103,104,105,106,107} [(~2.0 Å/cycle at 100 °C,¹⁰³ ~1.7 Å/cycle at 100 °C,¹⁰⁴ ~2.5 Å/cycle at 100 °C,¹⁰⁵ ~1.5 Å/cycle at 100 °C,¹⁰⁶ and ~1.9 Å/cycle at 75 °C¹⁰⁷] and also comparable to the GPC of PE-ALD ZnO using DMZ and O₂-plasma at room temperature (~1.6 Å/cycle).¹¹⁰ With the optimized recipe, films were deposited with 300 ALD cycles and an RF-power of 100 W both on Si and glass substrates and the optical and structural characteristics of the layers were investigated. The refractive index of the film at 633 nm on the Si substrate obtained by spectroscopic ellipsometry is 1.876 ± 0.003 and 1.877 ± 0.002 using the Cauchy and PSEMI-Mo model, respectively. The results are well comparable with the literature as will be discussed later. The crystalline properties were analyzed using specular XRD (θ/θ -scan) and GIXD. The specular diffractogram is shown in Figure 5.2(a). For the ZnO film deposited on glass, distinct peaks are observed at qz positions of 2.23, 2.41, and 2.54 Å⁻¹, which match with the (100), (002), and (101) position of a reference ZnO powder. For the ZnO film deposited on Si, the (100) and (101) peak are clearly present, whereas the (002) peak is absent, which could be due to an overlap with the Si (200) peak stemming from the substrate. Both samples show a polycrystalline pattern with a (100) texture (the (100) plane is preferentially aligned parallel to the substrate). Figure 5.2(b) shows a GIXD-map of the sample deposited on Si which provides additional information about the in-plane orientation of the crystallites. We observe diffraction rings for the (100), (002), and (101) reflection, which match with the

ZnO powder reference. Note that the (002) peak appears preferred in the in-plane direction. This confirms the observation from specular diffraction [Figure 5.2(a)] that the ZnO film features a (100) texture.

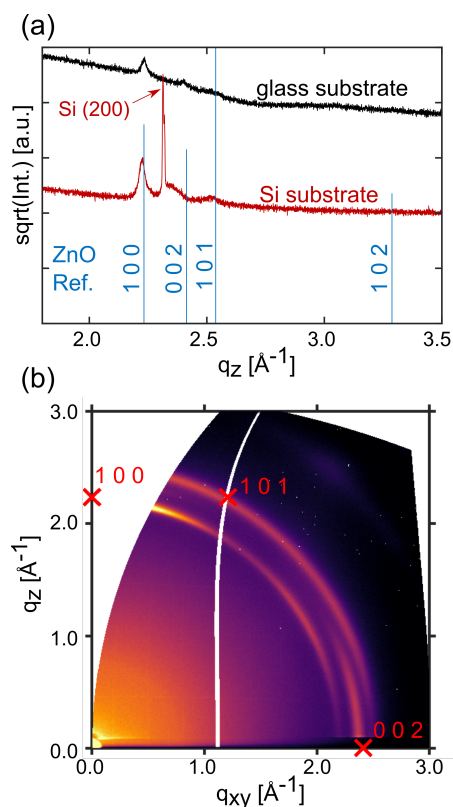


Figure 5.2: (a) Specular XRD patterns of films deposited on glass and Si-substrates utilizing the optimized recipe. Vertical lines show the peak positions and relative peak intensities of a ZnO powder reference (ICSD-26170). The spectra are shifted along the y-axis for clarity. (b) Corresponding GIXD-map of the sample prepared on the Si-substrate. Theoretical peak positions of crystalline ZnO in a (100) orientation are indicated by (x) markers and labeled with their respective hkl values.

In the literature, different crystal orientations have been reported for ALD-grown ZnO at different substrate temperatures. From the reported results, it is suggested that, besides temperature being the most influential parameter for the crystal growth,¹ the obtained orientation also depends on the substrate choice and the reaction mechanism (thermal or plasma-enhanced ALD). In agreement with our results, on Si(100) substrates, polycrystalline ZnO films with a (100) preferential orientation have been obtained by thermal ALD (using DEZ and water),⁹³ PE-ALD (using DEZ and O₂-plasma),¹⁰⁶ and PE-ALD (using DMZ and O₂-plasma)¹¹⁰ at 130, 100, and 25 °C, respectively. However, a study of thermal ALD (using

Table 5.2: Elemental compositions and Zn/O-ratios of ZnO films prepared with an unsaturated plasma dose and with the optimized recipe. Data are stated as mean values of two XPS survey scans on different sample spots and have been determined both for pristine and for surface sputtered samples. The corrected Zn/O-ratios correspond to a ratio corrected with regard to adventitious carbon (see text).

| | Oxygen / at. % | Zinc / at. % | Carbon / at. % | Zn/O-ratio | Corrected Zn/O-ratio |
|--------------------------------|----------------|--------------|----------------|-------------|----------------------|
| Unsaturated plasma dose | | | | | |
| Pristine | 45.1 ± 0.1 | 23.2 ± 0.1 | 31.7 ± 0.1 | 0.51 ± 0.01 | 0.94 ± 0.02 |
| Sputtered | 48.0 ± 0.1 | 49.3 ± 0.4 | 2.7 ± 0.4 | 1.03 ± 0.01 | |
| Optimized recipe | | | | | |
| Pristine | 43.1 ± 0.2 | 32.9 ± 0.5 | 24.0 ± 0.3 | 0.76 ± 0.02 | 0.92 ± 0.04 |
| Sputtered | 48.0 ± 0.4 | 51.0 ± 0.1 | 1.0 ± 0.3 | 1.06 ± 0.01 | |

DEZ and water) at 23 °C yielded ZnO with a (002) preferential orientation.¹¹¹ On glass substrates, polycrystalline films without preferential orientation have been reported from PEALD (using DEZ and O₂-plasma) at 100 °C,¹⁰⁴ while depositions on ITO/glass substrates yielded rather amorphous films.¹⁰⁵ XPS was used to investigate how the process parameters influence the chemical composition. Two different conditions were investigated. One sample was prepared with the optimized recipe while the other one was prepared with a shorter plasma exposure of 1 s. Both samples were sputtered to remove carbon contaminations from the surface. The results of the compositional analysis as well as the Zn/O-ratios of the pristine and sputtered samples are shown in Table 5.2.

For the pristine samples, the one prepared with the optimized recipe shows less amount of carbon and a higher Zn/O-ratio (24.0 ± 0.3 at.% and 0.76 ± 0.02, respectively) compared to the one prepared with an unsaturated plasma dose (31.7 ± 0.1 at.% and 0.51 ± 0.01, respectively). This could be due to the fact that for the sample prepared with a shorter plasma dose, the plasma step in the recipe is insufficient to fully oxidize the surface and thus remove the organic ligands. The Zn/O-ratio was further calculated taking into account organic contributions to the O 1s spectra as suggested by Payne et al.¹¹⁹ This was done by decomposition of the high-resolution spectrum of the C 1s peak obtaining normalized oxygen concentrations of the respective functional groups (alcohol/ether, carbonyl, ester, and carbonate). By subtracting the amount of oxygen in organic groups from the oxygen concentration obtained from the survey scan, a corrected Zn/O-ratio can be calculated, which is free of oxygen contributions from adventitious carbon species (labeled as corrected Zn/O-ratio in Table II). The Zn/O-ratio for both samples increases to values closer to unity (i.e., stoichiometric composition), with 0.94 ± 0.02 being observed for the sample prepared with unsaturated plasma dose and 0.92 ± 0.04 for the sample prepared with the optimized recipe. After sputtering, the amount of carbon is reduced to around 3 and 1 at.% for the sample prepared with un-

saturated plasma dose and optimized recipe, respectively. The Zn/O-ratio increases for both samples to a value slightly larger than 1 which is comparable to literature results.¹²⁰ However, preferential sputtering of oxygen could influence this ratio.¹²¹ High-resolution XPS scans of the O1s spectrum were performed on the two above mentioned samples after sputtering to obtain information about the chemical environment of the oxygen in the film. The results are shown in Figure 5.3.

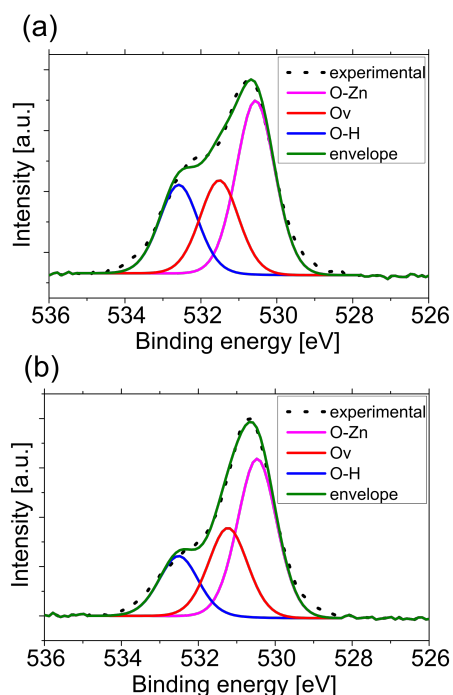


Figure 5.3: High-resolution O1s peak of (a) a film prepared with an unsaturated plasma dose (1s) and (b) a film prepared with the optimum recipe after sputtering. The experimental peak is decomposed into three Gaussian-peaks which correspond to different binding states of oxygen (see text).

The measured peak (dotted) can be decomposed into three peaks at around 530.5, 531.1, and 532.6 eV, which may be attributed to the oxygen-zinc (O-Zn) binding state, oxygen vacancy (Ov), and hydroxyl group (O-H), respectively.¹²² Oxygen vacancies reduce the screening of the nearest-neighbor oxygen ions and thus raise the effective nuclear charge which leads to a shift toward higher binding energies (medium peak).¹²³ It can be seen that the shoulder of the measured peak at around 532.6 eV, corresponding to the OH-groups, is reduced for the sample prepared with the optimized recipe compared to the sample prepared with an unsaturated plasma dose.

5.5.2 TUNING OF STRUCTURAL AND OPTICAL PROPERTIES BY RF-POWER

To investigate the effect of the RF-power on optical and structural properties, films were prepared with 300 cycles of the optimum recipe and varying the RF-power from 30 to 150 W. Figure 5.4(a) shows the diffractograms around the ZnO (100) peak for samples prepared with different RF-power. It can be seen that both peak position and intensity change with the applied RF-power, pointing out an effect on the d-spacing of the crystallites and on the amount of crystalline material being present in the film, respectively. The peak position shifts steadily to smaller q_z -values for higher powers, which means that the d-spacing in the (100)-direction is enlarged for higher powers from 2.811 Å for 30 W to 2.825 Å for 150 W. This could be due to defects or microstrain within the films. By increasing the RF-power, the peak intensity increases and saturates for RF-powers in the range 80–120 W and decreases again at 150 W.

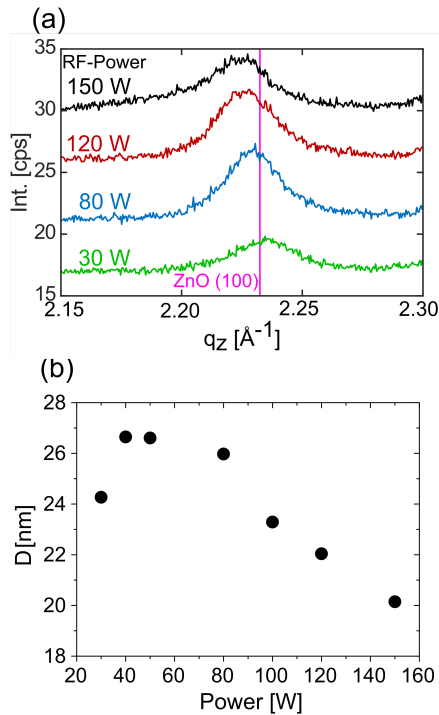


Figure 5.4: (a) Specular XRD patterns of films prepared at different RF-powers and theoretical ZnO (100) peak position (vertical line). (b) Average crystallite size in specular direction, calculated using Scherrer's formula, as a function of applied RF-power. In (a), the diffraction patterns are shifted in intensity and have been computationally smoothed for clarity.

In contrast, Kwon et al.¹¹³ reported no significant changes in crystallinity and crystal orientation for RF-powers in the range of 50–200 W, but an increase in both resistivity and O/Zn-ratio for increasing RF-power. A possible explanation is the difference in substrate

temperature; while their depositions were carried out at 100 °C, the present depositions were carried out near room temperature. Additional influencing factors are different reactor geometries and plasma densities. An estimation of the average crystallite size D in specular direction can be obtained from a Bragg peak in the diffractogram using Scherrer's formula,⁷⁴

$$D \approx \frac{\lambda}{\beta_{2\theta} \cos \theta}, \quad (5.3)$$

in which λ is the wavelength of the X-rays, $\beta_{2\theta}$ is the full-width at half maximum of the peak, and θ is the peak position. A plot of the (100) peak position with respect to the RF-power is shown in Figure 5.6 in the supplementary material. Figure 5.4(b) shows the crystallite size with respect to RF-power calculated from the (100) peak properties shown in Figure 5.4(a). The crystallite size is about 24 nm for 30 W, rapidly increases to above 26 nm for 40–80 W, and then steadily decreases to 20 nm for 150 W. These results point out the possibility of tuning the crystalline structure of the films by acting on the RF-power. With this approach, the crystallite size can be tailored to meet specific application requirements, e.g., for photocatalytic applications,¹²⁴ where a certain crystallite size of the film is desired. The growth per cycle and optical properties of the films were measured using spectroscopic ellipsometry. The results for the growth per cycle, refractive index n , extinction coefficient k , and bandgap with respect to the RF-power are shown in Figure 5.5.

The growth per cycle [Figure 5.5(a)] is constant over the whole range of RF-powers with an average value of ~ 1.5 Å/cycle. An increased standard deviation can be seen for samples prepared with 120 and 150 W (also for the refractive index and bandgap) which could be caused by spatial inhomogeneities of the plasma in our setup. The refractive index n at 633 nm [Figure 5.5(b)] is 1.814 ± 0.002 for 30 W, increases rapidly to 1.865 ± 0.003 as power is increased to 40 W and then saturates within the error limits to 1.87 ± 0.01 for RF-powers higher than 50 W. This behavior could either originate from changes in the electronic structure due to variation in defect density or from structural changes of the films (such as the amount of crystalline material, microstrain, or texture as afore-mentioned in the discussion of Figure 5.4) introduced by variation of the RF-power. Bond et al.¹²⁵ obtained a refractive index of 1.99 for a ZnO single crystal at 633 nm, which is 0.12 higher than our obtained value. The refractive index is however well comparable with results obtained for ZnO thin films grown by PE-ALD, magnetron sputtering, and spray pyrolysis,^{103,114,126} all of them obtaining refractive index values of ~ 1.88 . (Kawamura et al.¹⁰³ do not state at which wavelength the refractive index was measured; however, providing a normal dispersion relation, we assume that it has

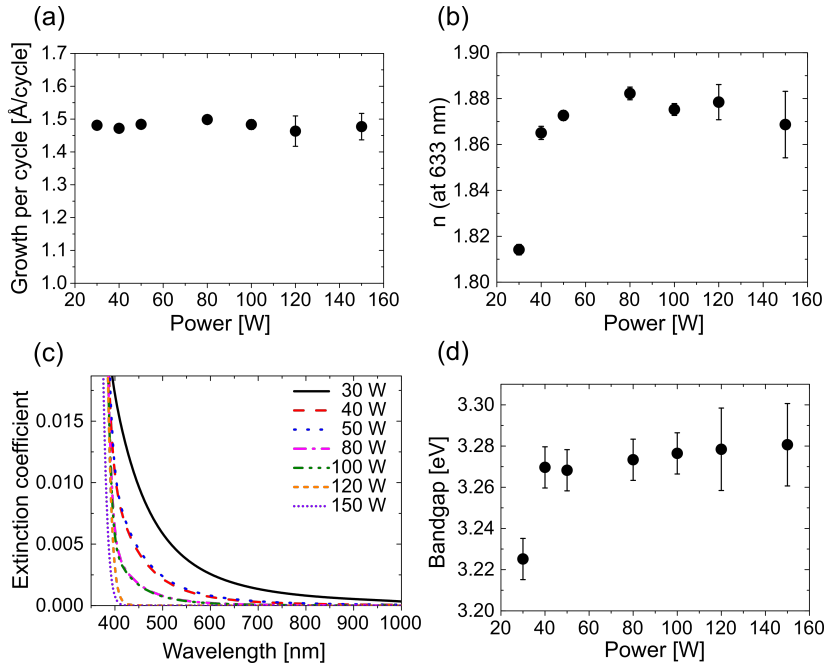


Figure 5.5: (a) Growth per cycle, (b) refractive index, (c) extinction coefficient spectra, and (d) bandgap with respect to RF-power. The error bars in (a) and (b) originate from the standard deviation of values obtained for films deposited on different positions in the reactor, the spectra in (c) are from samples at the same position in the reactor, and the error bars in (d) originate from the uncertainty in the tangent in the respective Tauc-plots.

been obtained in the ZnO transparent region.) The tuning of the refractive index together with the precise thickness control of ALD-processes could be used in devices such as dielectric Bragg reflectors.¹²⁷ The spectrum of the extinction coefficient k [Figure 5.5(c)] for an RF-power of 30 W shows a smooth transition and k only slowly decays toward higher wavelength, i.e., there is a significant absorption above the bandgap, indicating the existence of defect absorption states (e.g., carbon impurities, O-H groups, or oxygen vacancies, as shown in the XPS analysis).¹¹⁶ For higher RF-powers, the onset of the absorption becomes sharper pointing out a reduced defect concentration and less absorption at higher wavelengths. For the sample grown with 30 W, the absorption coefficient α is 405.0 and 42.1 cm^{-1} at a wavelength of 633 and 1000 nm, respectively. These values decrease with increasing power and are 26.2 and 1.1 cm^{-1} at a wavelength of 633 and 1000 nm, respectively, for the sample prepared at 100 W. The bandgap [Figure 5.5(d)] shows a rapid increase from 3.23 ± 0.01 to 3.27 ± 0.01 eV when increasing the RF-power from 30 to 40 W and then increases further to 3.28 ± 0.02 eV for 150 W. This allows for bandgap tuning in a small range without the need for dopants,^{128,129} applicable in a range of optical and electronic applications. The ob-

tained value for the bandgap using Tauc fitting compares well with the literature; for example, Viezbicke et al.¹¹⁶ found an average value for the bandgap of 3.276 ± 0.033 eV, comparing a large number of publications on thin film ZnO. Furthermore, a sample prepared with 100 W on a glass substrate was analyzed with UV-Vis spectroscopy, the absorbance plot is shown in Figure 5.7 in the supplementary material.⁵⁶ By utilizing Tauc fitting, a bandgap value of 3.26 ± 0.01 eV was obtained, which is comparable with the value obtained by fitting the spectroscopic ellipsometry spectra. Concluding, by increasing the RF-power from 30 W to an intermediate range of RF-powers in the range of 40–100 W, the ZnO layers were found to grow with increased refractive index n [at 633 nm, Figure 5.5(b)] and with increased crystallite size [for RF-powers in the range 40–80 W, Figure 5.4(b)]. The transition of the extinction coefficient was found to become sharper [Figure 5.5(c)] and the bandgap shifted toward higher energies [Figure 5.5(d)]. We found the RF-power to have no significant influence on the growth per cycle [Figure 5.5(a)].

5.6 SUMMARY AND CONCLUSIONS

In this contribution, we demonstrate the deposition of polycrystalline ZnO with a (100) texture by PE-ALD at substrate temperatures close to room temperature using DEZ and O₂-plasma as the precursor and coreactant, respectively. Only a few examples are present in literature of studies concerning the combination DEZ, PE-ALD and room temperature deposition, which to the authors' opinion is the most convenient combination in terms of monomer availability (DEZ as opposed to DMZ is largely available), and processing parameters. Especially the access to polycrystalline ZnO at low substrate temperature will enable the exploration of a wide variety of applications for this material, involving polymer hybrids and biomaterials, to name a few. The ZnO growth within our setup was found to be self-limiting when the length of every ALD cycle was fixed at 0.32 s for the DEZ dose, 5 s for the Ar purge, 3 s for the O₂-plasma dose, and 12 s for the second Ar purge. In these optimized conditions, the GPC was 1.50 ± 0.05 Å/cycle, in agreement with pure ALD growth of ZnO. The refractive index was comparable with ZnO grown by other techniques and the XPS chemical analysis confirmed a Zn/O-ratio close to unity, with a low amount of carbon impurities being present (~1 at.%, after sputtering). Another interesting aspect is the tunability of optical and structural properties by varying the RF-power. In the range from 30 to 150 W, the crystallite size changed from 20 to 26 nm, the refractive index at 633 nm from 1.81 to 1.88, and the bandgap from 3.22 to 3.27 eV. The possibility to adjust these parameters is extremely

important for the use of ZnO deposited by PE-ALD at near-room temperature for a wide range of devices for optical, electrical, or sensing applications to meet the purpose-specific requirements.

5.7 ACKNOWLEDGMENTS

This project has received funding from the European Research Council (ERC) under the European Union's Horizon 2020 research and innovation program (Grant Agreement No. 715403). The authors thank the Elettra-Trieste for the allocation of synchrotron radiation beamtime. The authors are grateful to Nicola Demitri and Luisa Barba for providing assistance in using beamline XRD and Stephan Tumphart and Oliver Werzer for supporting the experiments.

5.8 SUPPORTING INFORMATION

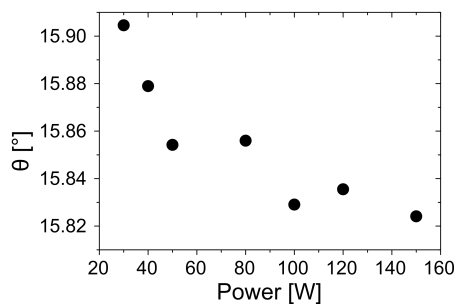


Figure 5.6: Bragg peak position θ with respect to RF-Power. θ steadily shifts to lower angles with increasing power.

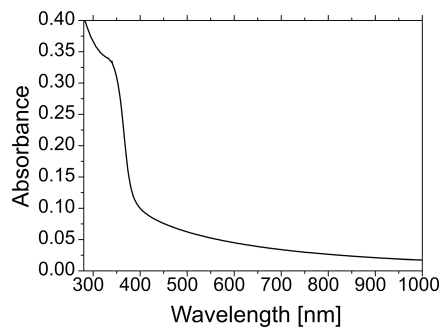


Figure 5.7: Absorbance spectrum of a sample prepared with the optimized recipe at 100 W on a glass substrate. The spectrum was corrected for the absorbance of the glass.

6

ZnO Thin Films Grown by Plasma-Enhanced Atomic Layer Deposition: Material Properties Within and Outside the “Atomic Layer Deposition Window”

6.1 PREFACE

ORIGINAL PAPER



**ZnO Thin Films Grown by Plasma-Enhanced Atomic Layer
Deposition: Material Properties Within and Outside the
“Atomic Layer Deposition Window”**

*Julian Pilz, Alberto Perrotta, Günther Leising, and Anna Maria Coclite**

The work was conducted at Graz University of Technology. The author of the thesis

performed sample preparation, characterization, data evaluation and wrote the manuscript. Alberto Perrotta supported the data evaluation, Günther Leising supported optical experiments and data evaluation, and Anna Maria Coclite supervised the work and supported data analysis. All authors reviewed the manuscript. The following text and images are identical to the published work:

- Pilz, J.; Perrotta, A.; Leising, G.; Coclite, A. M. ZnO Thin Films Grown by Plasma-Enhanced Atomic Layer Deposition: Material Properties Within and Outside the “Atomic Layer Deposition Window.” *Phys. status solidi* **2019**, 1900256.

6.2 ABSTRACT

ZnO thin films and nanostructures are applied in various devices due to their interesting optical and electrical properties. Atomic layer deposition (ALD) of ZnO offers unique advantages such as precise thickness control, uniformity, and conformality. Using reactive plasma species as the co-reactant (PE-ALD) allows further enhancement of the material characteristics and tunable properties. The substrate temperature has been reported to be the most influential parameter in this technique, as it affects the growth per cycle (GPC) and material properties. However, an investigation on how the film properties are linked to the GPC is lacking in the literature. Herein, the temperature dependence of several material properties is found closely related to the GPC. The preferential crystal orientation switches from (100) to (002) up to the constant region of the GPC versus temperature, the so-called ALD window. Refractive index and mass density show different slopes in temperature regions outside and within the ALD window. Excitonic absorption is only found for films prepared within the ALD window, and the resistivity drops rapidly above the ALD window. Following these results, more insights can be gained on the ALD growth (especially the role of the ALD window) and ideal temperature ranges for specific applications.

6.3 INTRODUCTION

ZnO attracts great attention due to its direct wide bandgap and interesting optical, electrical, and piezoelectric properties.⁵⁶ In its thin film or nanostructure form, these properties have been exploited for applications such as transparent conductive oxides,^{70,130} resistance random access memories,^{131,132} gas sensors,^{55,133} and piezoelectric generators.^{57,90}

Among the techniques used to deposit ZnO thin films, atomic layer deposition (ALD) stands out due to the possibility to conformally coat complex structures, precise thickness control (in the Å-range), and relatively low deposition temperatures.^{4,81} One cycle in the ALD process comprises the sequential exposure of the substrate to two (or more) precursors, separated by purge steps. This cycle is repeated until the desired thickness is achieved. As the surface reactions during the respective steps in a cycle are self-limiting, the growth per cycle (GPC) is typically less than a monolayer and in the Å cycle⁻¹ range.

Most investigations on ALD of ZnO adopt diethylzinc (DEZ) and water as the precursor and co-reactant, respectively. The surface reactions in this case are driven by thermal energy, and the substrate is heated during the deposition. This process is usually referred to as thermal ALD. A variant is plasma-enhanced atomic layer deposition (PE-ALD), in which reactive plasma species are utilized as co-reactants instead of water.⁶ The advantages of using PE-ALD instead of thermal ALD include often a higher growth rate, improved material characteristics at lower substrate temperature, and the possibility to tune material properties by changing the plasma characteristics.^{6,104,134}

The substrate temperature has been reported to be the most influential deposition parameter in both thermal ALD and PE-ALD.⁸¹ The GPC shows a strong temperature dependence outside the so-called ALD window, a region in which it stays constant. (This in our opinion is the most commonly used (though controversial) definition of the term ALD window in the literature. Other definitions have been used¹³ referring to a temperature range in which the criterion of self-terminating reactions is fulfilled without the necessity of having a constant GPC versus temperature.) Within the ALD window, the growth mechanism is considered to happen in an ideal ALD manner, i.e., complete and self-limiting surface reactions.⁴ Furthermore, the substrate temperature strongly affects the structure, stoichiometry, and amount of defects of the ZnO films and, in turn, device-related optical and electrical properties. While the temperature dependence of the GPC for PE-ALD of ZnO has been investigated by several groups over a wide temperature range,^{104,107,110,135,109,106} material or device properties have often been described independently of the growth behavior. The crystallinity and texture of PE-ALD ZnO films have been shown to be strongly affected by the substrate temperature. A switch from (100) preferential orientation at lower temperature to (002) for higher temperatures has been shown by Park et al.,¹⁰⁷ Zhang et al.,¹⁰⁶ and Rowlette et al.¹¹⁰ Likewise, a switch from no preferential orientation to (002) preferential orientation was shown by Kim et al.¹⁰⁴ In all these cases, the temperature at which this switch happens seems to be closely related to the beginning of the reported ALD window. A discussion on

how a switch in the preferential orientation affects the GPC is missing in these publications. Photoluminescence (PL) was also shown to depend on the substrate temperature and is an indicator for the optical quality and defects in the ZnO films. While the PL spectra showed a significant near-band-edge emission (i.e., high optical quality) for samples prepared within the ALD window,^{104,110,106} defect-related emission bands were observed for substrate temperatures below^{110,106} or above¹⁰⁴ the ALD window. Kim et al.¹⁰⁴ furthermore showed that the resistivity decreased drastically for ZnO films prepared at temperatures above the ALD window, correlating it with an increase in the defect carrier concentration. The temperatures, at which these changes in material properties occur, differ among the publications. However, when analyzing the temperature trend of the material properties and the GPC within a publication, the trends often seem to correlate.

The aim of the present publication is therefore to link the temperature dependency of several material properties to the temperature behavior of the GPC, especially focusing on regions below, within, and above the ALD window. By this, a more detailed description of the ALD growth regimes of ZnO is presented, as well as general directions to select the right temperature region for specific applications.

6.4 EXPERIMENT

ZnO thin films were deposited using a custom-built direct plasma ALD reactor. The reactor was in an asymmetric plate configuration, and the clearance between the top showerhead radio frequency (RF) electrode and the heating stage (Yuheng Electric Heating Technology Co., Ltd) was 5 cm. DEZ (optoelectronic grade, Dockweiler Chemicals) was used as the metalorganic precursor and was pulsed into the reactor using an ALD-valve (Swagelok ALD₃) without additional heating or bubbling system. An RF-power generator (Advanced Energy Cesar 13.56 MHz) combined with a matching network (Advanced Energy Navio) served as the power source for the O₂-plasma. The pumping system consisted of a turbomolecular pump (Pfeiffer vacuum TMH071P) and a rotary vane pump (Pfeiffer vacuum DUO₅M). The pressure in the reactor was ≈ 75 mTorr during plasma exposure. The flow rates of O₂ and Ar were set to 20 sccm during the plasma and purging step, respectively, using a multi gas controller (MKS 647C) and mass flow controllers (MKS MF1-C).

The ALD process consisted of the repetition of the following four steps 1) DEZ dose; 2) Ar purging; 3) O₂-plasma dose (including a 10 s O₂-flow stabilization step prior to the plasma ignition); and 4) Ar purging. Prior to the deposition, the samples were exposed to 8 s

O₂-plasma to activate the surface. The RF-power for the plasma dose was fixed at 60 W for all depositions. The saturation behavior of the four steps was investigated at room temperature,¹³⁴ and due to possible decomposition effects of DEZ,¹⁰⁹ the saturation of the purging step after DEZ was also investigated at 250 °C. At higher temperatures, the growth was found to be self-limiting when the recipe was fixed at 0.15 s for the DEZ dose, 22 s for the Ar purge, 8 s for the O₂-plasma dose, and 15 s for the second Ar purge. This recipe was applied to all temperatures investigated. The setup was controlled by an Arduino microcontroller and an in-house written Python program. The ZnO films were grown on single-side polished Si (100) substrates with a native oxide layer for spectroscopic ellipsometry and X-ray reflectivity, on quartz substrates (Esco Optics) for UV-vis spectroscopy, and on glass substrates for X-ray diffraction and four-point probing. The films were prepared at substrate temperatures ranging from room temperature to 250 °C. The growth per cycle (GPC) for each deposition was obtained by dividing the mean value of the film thickness of three samples, placed on different positions on the substrate heater, by the number of cycles. Due to the temperature-dependent GPC, the number of cycles for each of the respective depositions at different temperatures was modified to obtain film thicknesses in the range of 25–34 nm.

Spectroscopic ellipsometry (SE, J.A. Woollam M-2000V) was used to determine the thickness and optical constants of the films. Measurements were carried out in a wavelength range of 370–1000 nm at three different angles (65°, 70°, and 75°). Using a Cauchy model in the transparent region of the ZnO films (450–1000 nm), it was possible to extract the thickness and refractive index of the film.

UV-vis spectroscopy (Shimadzu UV-1800) was used to measure the transmission of the films in a wavelength range from 190 to 1100 nm, and the absorption edge could be extracted via Tauc fitting.^{134,116} Contributions from reflections were neglected in the analysis.

XRD in a θ/θ -configuration (Panalytical Empyrean) utilizing monochromatized copper radiation ($\lambda = 1.5418 \text{ \AA}$) was used to analyze the specular crystalline properties of the films. The diffractometer's PIXcel3D-detector was operated in 1D-mode and a 1/8° divergence slit, a 10 mm mask, and a P7.5 antiscatter slit were used in the setup. Furthermore, X-ray reflectivity (XRR) measurements were performed to gain information on the electron density and, from that, the mass density was derived. The measurements were performed on the same system as the XRD measurements, but adopting a 1/32° divergence slit and a Po.1 antiscatter slit. The detector was operated in point mode with three channels.

Four-point-probing (Jandel Universal Probe Station, tip spacing 1 mm inline) was performed on films deposited on 2.5 × 2.5 cm glass substrates at room temperature. The resis-

tivity was calculated by

$$\rho = 4.45 \times \frac{U}{I} \times t \quad (6.1)$$

and U and I are the measured voltage and current, respectively, 4.45 is a geometry factor, and t is the mean layer thickness from SE measurements.

6.5 RESULTS AND DISCUSSION

The dependence of the GPC with respect to the substrate temperature is shown in Figure 6.1(a). It was found to rapidly increase with the substrate temperature, from $1.6 \text{ \AA cycle}^{-1}$ at $25 \text{ }^\circ\text{C}$ to around $2.5 \text{ \AA cycle}^{-1}$ at $125 \text{ }^\circ\text{C}$. In the range of 125 to $200 \text{ }^\circ\text{C}$, the GPC was constant and therefore we identified this region as the so-called ALD window.⁴ The thickness deposited per cycle in the ALD window with a value around 2.5 \AA is comparable with the interplanar spacing along the c -axis of the ZnO wurtzite crystal structure (2.60 \AA). The crystalline properties and texture of the films are discussed in detail later, showing the correlation between the ALD window and the structural parameters. Further increase in the substrate temperature leads to a rapid increase in the GPC. In addition, the standard deviation in this region significantly increases, pointing out a spatial dependence of the growth in the reactor, typical of a chemical vapor deposition (CVD) component in the growth. Different effects have been proposed to explain the temperature dependency of the GPC. At temperatures below the ALD window, not enough energy is delivered to the system to complete all surface reactions leading to lower GPC.³² At temperatures above the ALD window, precursor molecules instead decompose into smaller fragments, leading to an accelerated CVD-like growth and an increase in GPC.^{104,109,32} At the same time, desorption of precursor molecules can take place, leading to a decrease in GPC at high temperatures.^{106,32} In addition, as ALD growth happens ideally in a monolayer-by-monolayer fashion, the GPC will also be influenced by the lattice spacing when growing crystalline films. As the preferential orientation and thus the lattice spacing normal to the substrate can change with temperature,²⁷ so will the GPC. These different effects happen simultaneously, making their individual effects on the GPC difficult to distinguish. On the other hand, especially for PE-ALD, self-limiting growth can be achieved well below the ALD window.^{134,136} This raises questions about the definition and relevance of the ALD window (in PE-ALD processes) and the often exclusive focus on properties at temperatures within the window. For this reason, an analysis of the opto-chemical and structural properties of ZnO layers as a function of the relative position

of their deposition temperature with respect to the ALD window will help in correlating process parameters and material properties in a more rigorous way.

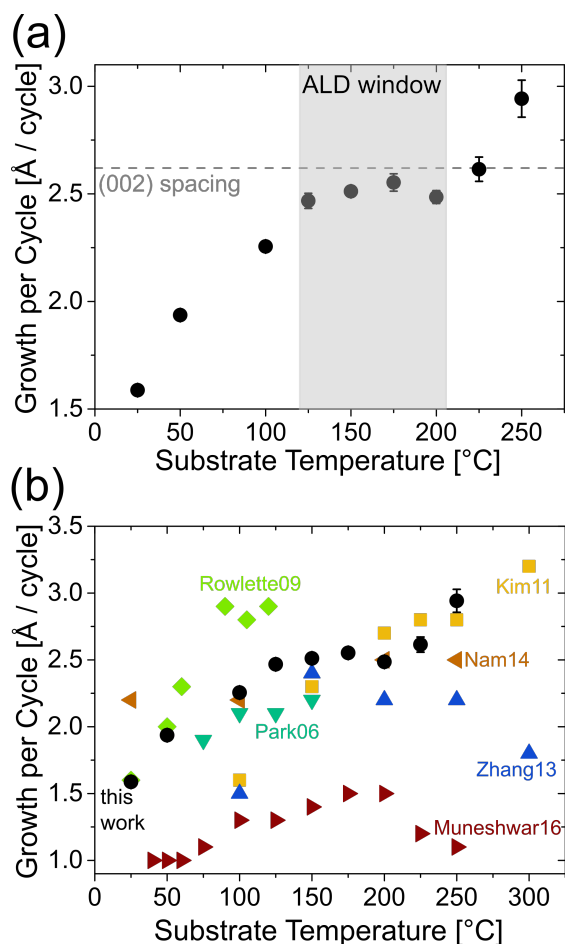


Figure 6.1: a) Growth per cycle with respect to the substrate temperature of samples prepared on Si substrates. The gray area marks the ALD window, in which the GPC stays constant. The error bars are plotted for each data point but are within marker size in most cases. The size of the unit cell along the *c*-axis of the ZnO wurtzite crystal structure is indicated by the dashed line. b) Comparison of the results from (a) with selected literature results. An error of $\pm 0.1 \text{ \AA cycle}^{-1}$ has to be taken in to account for the literature results. References are given in the main text

In the literature, a similar behavior of the GPC with respect to substrate temperature has been reported, i.e., a steep increase toward a constant regime with increasing temperature, and either an increase or decrease for temperatures higher than the ALD window. A selection of literature results^{104,107,110,135,109,106} on PE-ALD ZnO for the temperature behavior of the GPC in comparison with this work is shown in Figure 6.1(b).

While the general trend of the data in the figure is similar, the obtained values of the various publications differ largely. This difference is especially highlighted in the start, end, and width

of the ALD window as well as the values of the GPC, and it was suggested to mostly stem from differences in the reactor designs.⁸¹ Nevertheless, an ALD window has been observed in all the aforementioned publications.

The crystalline properties investigated by specular X-ray diffraction (XRD) are shown in Figure 6.2. At room temperature, the ZnO films exhibit a polycrystalline pattern with a (100) texture, as reported in a previous publication.¹³⁴ By increasing the substrate temperature, the contribution of (002) peak increases and becomes the dominant orientation. In detail, for temperatures higher than 100 °C, the crystallites are highly oriented in the [002] direction and the (100) peak is drastically reduced in intensity. A (100) or (002) texture can thus be obtained by applying either a low or high substrate temperature, respectively. A similar behavior was observed by Zhang et al.,¹⁰⁶ but temperatures below 100 °C were not investigated in their study. Depositing crystalline films with a texture at temperatures below 100 °C could, however, be beneficial for applying functional ZnO films on thermo-sensitive substrates (e.g., polymers^{69,97,98} or biomaterials^{99,100}). On the other hand, a (002) texture is often desired in piezoelectric^{57,89} or optoelectronic^{91,137} applications, as the *c*-axis (i.e., the polar axis) of the ZnO crystallites is oriented perpendicular to the substrate plane.

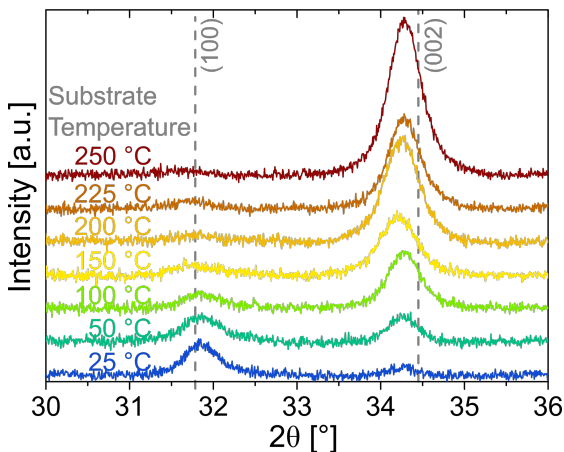


Figure 6.2: Specular XRD spectra of samples prepared on glass substrates at different substrate temperatures. The spectra are stacked for clarity. Vertical, dashed lines show the peak positions of a ZnO powder reference (ICSD-26170).¹³⁸ A shift to smaller angle (i.e., larger lattice spacing) compared with the powder pattern is apparent for the (002) peak, which may originate from microstrain in the sample.

By comparing the crystalline properties with respect to the ALD window, the following observations can be made. Below the ALD window (25–100 °C), we can observe both the (100) and the (002) peak. There is a mixture of both orientations, whereas the (002) orientation becomes the dominant one at higher temperatures. Inside the ALD window (125–

200 °C), the films are highly (002) textured and show enhanced crystallinity. As mentioned earlier, the GPC within the ALD window ($\approx 2.5 \text{ \AA cycle}^{-1}$) is close to the interplanar spacing of the (002) orientation (2.60 Å). The interplanar spacing of the ZnO wurtzite structure oriented along the (002) and the (100) planes is sketched in Figure 6.3.

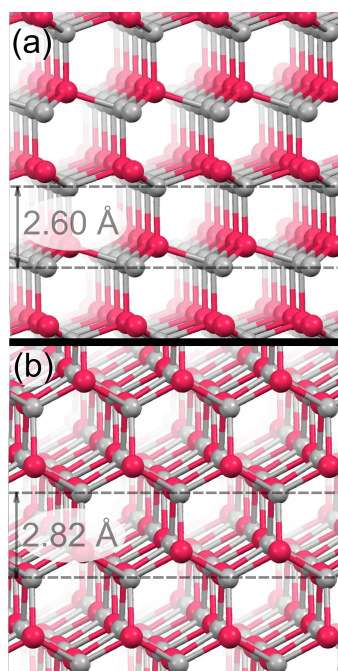


Figure 6.3: Sketch of the atomic configuration of the ZnO wurtzite crystal structure with a) (002) orientation and b) (100) orientation. Gray and pink atoms correspond to Zn and O, respectively. The sketch was obtained using the Mercury 3.10.3 software and with the lattice parameters of ICSD-26170.¹³⁸

Looking at the atomic arrangement of both orientations, the (002) planes parallel to the substrate consist of atoms of only one species, whereas the planes of the (100) orientation consist of alternating Zn and O atoms. This would suggest that not a full crystalline plane with (100) orientation can be grown within one cycle in the ALD process, but the GPC is restricted to half of the lattice spacing ($2.82 \text{ \AA} / 2 = 1.41 \text{ \AA}$). Thus, the crystal orientation at temperatures below the ALD window together with the not complete surface reactions could explain the lower GPC that we observe at those temperatures. For temperatures above the ALD window, the GPC increases to values larger than the (002) interplanar spacing, whereas the XRD results show a strong preferential (002) orientation. Thus, in this temperature region, the growth cannot happen in a monolayer-by-monolayer fashion anymore but includes a CVD-component in the mechanism. This component also accounts for the large standard deviation of GPC values at these temperatures, reported in Figure 6.1(a).

The relationship between texture and GPC in thermal ALD of ZnO (applying DEZ and water) has been investigated by Yousfi et al.¹³⁹ They found a (100) preferential orientation within the ALD window and a GPC in between 1 and 2 monolayers of the (100) orientation. The GPC values larger than a monolayer were attributed to the possible presence of roughness. In other publications on thermal ALD,^{111,93,140,141} a transition from (002) to (100) preferential orientation with temperature was reported, often accompanied with a drop in (002) peak intensity at the edges of the ALD window. Within the ALD window, both (100) and (002) orientations were apparent with no strong preferential orientation and a GPC of around 2 Å. These GPC values lie in between the (100) spacing (1.41 Å) and the (002) spacing (2.60 Å). This is an indicator that the GPC within the ALD window is strongly correlated to the preferential orientation also for thermal ALD. At high temperatures above the ALD window, the preferential orientation switched back to (002).^{139,93}

The refractive index and the mass density of the films are shown in Figure 6.4. The refractive index values were obtained by applying a Cauchy model to the SE data and are reported for a wavelength in the ZnO transparent region (633 nm). The mass density was obtained by measuring the critical angle α_c by XRR and applying the following formulas.¹⁴² The electron density can be calculated as

$$\rho_e = \left(\frac{\alpha_c}{\lambda}\right)^2 \times \pi r_e \quad (6.2)$$

where ρ_e is the electron density, α_c is the critical angle from the XRR measurement, $\lambda=1.5418$ Å wavelength of the Cu K_α radiation, $r_e = 2.818 \times 10^{15}$ m is the classical electron radius.

The mass density can then be derived from

$$\rho = \frac{\rho_e}{N_{e,ZnO}} \times \frac{M_{ZnO}}{N_A} \quad (6.3)$$

where ρ is the mass density, ρ_e is the electron density from 6.2, $N_{e,ZnO}=38$ is the number of electrons in the ZnO molecule, $M_{ZnO}=81.38$ g mol⁻¹ is the molar mass of ZnO, $N_A = 6.022 \times 10^{23}$ mol⁻¹ is the Avogadro constant.

Both the refractive index and the mass density show trends in regions corresponding to the ALD window. The refractive index shows a strong rapid increase from 1.90 at room temperature up to 1.93 at the start of the ALD window. In this region, the XRD results pointed out a switch from (100) to (002) texture. In the ALD window, the increase slows down, and XRD results showed a more pronounced (002) peak with increasing temperature. Above

the ALD window, a rapid drop down to 1.86 can be observed for the refractive index. Similarly, the mass density slightly increases below the ALD window, strongly increases within the ALD window, and decreases again above the ALD window. Please note that for calculating the mass density, ideal ZnO bulk values are assumed. Nonstoichiometric films could therefore lead to values that are above the literature value for ZnO¹⁴³ ($\rho = 5.61 \text{ g cm}^{-3}$). In fact, X-ray photoelectron spectroscopy (XPS) analysis points out an increase in Zn/O ratio for higher temperatures (Figure 6.8, Supporting Information), which has also been reported for thermal ALD of ZnO.¹²¹ However, the trend for the mass density is valid as the measured electron density is only multiplied by a constant to obtain the mass density.

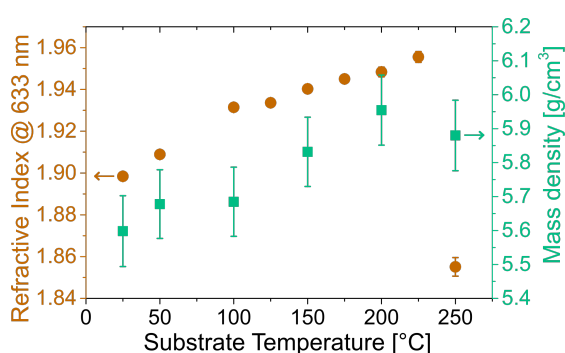


Figure 6.4: a) Refractive index at 633 nm obtained from SE (circles) and b) mass density obtained from XRR (squares) as a function of substrate temperature for samples prepared on Si substrates. Error bars are plotted for all data points but are only visible for some.

Transmission spectra obtained by UV–vis spectroscopy are shown in Figure 6.5(a). All the films are highly transparent (transmission >90%) over most of the visible light range, sufficient for its use as a transparent electrode (when doped, e.g., with Al)⁵⁶ or as a buffer layer¹⁴⁴ in photovoltaic devices. At around 500 nm, the films start to absorb and the transmission decreases rapidly. Interesting features can be observed around the bandgap that can be better followed in Figure 6.5(b), in which the absorption coefficient is plotted over energy in the region marked in Figure 6.5(a). The absorption coefficient was calculated from the transmission values by $\alpha = -\frac{\log(T)}{d}$, with α being the absorption coefficient, T the transmission, and d the layer thickness. Below the band edge, α includes contributions from reflection; it is however well represented above the band edge.

For films deposited at temperatures below the ALD window (25 and 50°C) the absorption coefficient shows a rather smooth transition from transmitting to the absorbing region, while it becomes sharper with temperatures within the ALD window. At 250°C (above the ALD window), the transition becomes again very smooth. A sharper transition in the absorp-

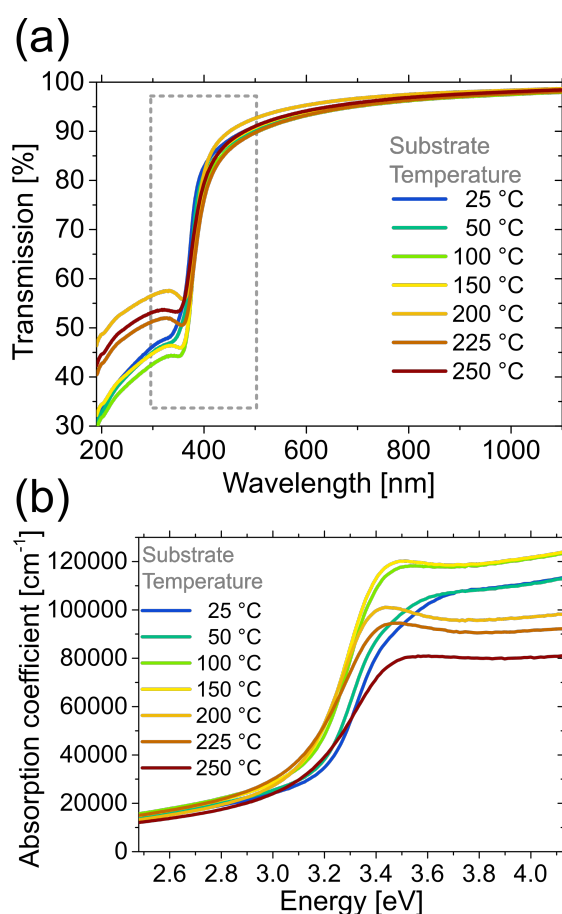


Figure 6.5: a) UV-vis transmission spectra of samples prepared at different substrate temperatures on quartz substrates and b) absorption coefficient from the region around the band edge region highlighted in (a).

tion spectra can be attributed to a higher optical quality within the ALD window, i.e., less amount of defect absorption states.¹¹⁶ Furthermore, for samples prepared within the ALD window, a peak at around 3.4 eV was observed. The peak can be attributed to the formation of excitons. Observing these excitonic features at room temperature (for films deposited within the ALD window) points out a high structural quality of these thin films.^{145,146} This property, combined with the significantly lower substrate temperature compared with other techniques (such as pulsed laser deposition¹⁴⁵) and the possibility to conformally coat complex structures, makes PE-ALD an attractive deposition technique for functional optical devices.¹⁴⁷ As an example, UV lasing has been reported for ZnO thin films, which is based on stimulated excitonic emission.^{56,137,148}

The absorption edge could be obtained via Tauc-fitting from the absorption coefficient

spectra. As ZnO has a direct bandgap, the absorption coefficient reads

$$\alpha(E) = \frac{A}{E}(E - E_g)^{\frac{1}{2}} \quad (6.4)$$

with A a constant and E_g the bandgap. Thus, by plotting $(\alpha E)^2$ over E , the bandgap can be extracted by extrapolating the linear region to 0 (Tauc plot; example shown in Figure 6.9, Supporting Information).^{116,149} It was, however, reported that this fitting procedure does not give the real bandgap value in the presence of an excitonic peak in the absorption spectrum but rather the onset of the absorption edge.¹⁴⁹ The absorption edge obtained from both SE and UV-vis measurements is plotted in Figure 6.6.

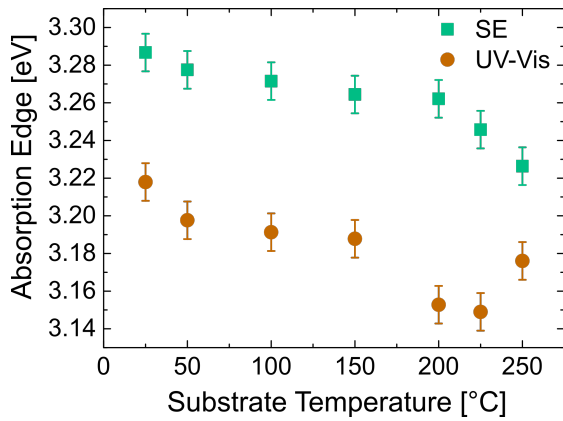


Figure 6.6: Absorption edge as a function of substrate temperature obtained from Tauc fitting from SE (square) and UV-vis (circle) measurements. Samples prepared on Si (SE) or quartz (UV-vis) substrates.

The absorption edge obtained from UV-vis measurements shifts to lower energy (red shift) with increasing temperature from 3.22 eV at room temperature to 3.15 eV at 225 °C. A red shift of the absorption edge with increasing substrate temperature has been observed in thermal ALD¹⁴¹ and CVD¹⁵⁰ of ZnO. In the thermal ALD reference,¹⁴¹ Yuan et al. found a reverse relationship between the refractive index and the bandgap with increasing substrate temperature, which is in line with our results (Figure 6.4). Furthermore, the near-bandgap-emission (in PL) showed a red shift and high intensity (accompanied by increased crystal quality) at high temperature. Tan et al.¹⁵⁰ performed CVD of ZnO and found a red shift of the bandgap with increased substrate temperature due to crystallization of amorphous regions. Moreover, a red shift of the absorption edge has been observed in annealing procedures of ZnO, associated with an enhanced removal of intrinsic defects and improved crystallinity at a higher annealing temperature.^{151,65} The absorption edge increases by around 30 meV when the sub-

strate temperature is further increased from 225 to 250°C. This phenomenon could be explained by the Burstein-Moss effect caused by an enhanced free electron density and thus filling of lower states in the conduction band.¹⁵² This would also agree well with the resistivity drop in Figure 6.7. The absorption edge shift could thus be explained by an interplay of changes in the crystalline structure (Figure 6.2) and defect density. A detailed analysis of the defects by, e.g., PL is, however, not within the scope of this article. Also for the absorption edge obtained from SE measurements, a red shift can be observed. However, an offset is apparent, with the SE results being around 70 meV higher than the UV-vis results. This is attributed to the limited measurement range of the available ellipsometer (370–1000 nm), being able to measure only the foot region of the absorption. The limited measurement range leads to a different slope in the Tauc-fitting and consequently to an offset (and further decrease instead of an increase of the absorption edge at 225 to 250°C) compared with the evaluation of the UV-vis measurements.

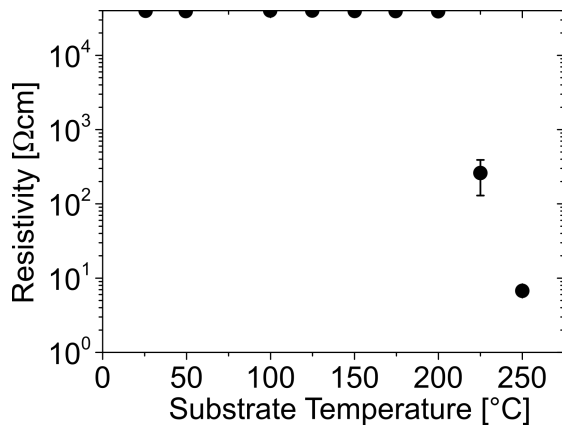


Figure 6.7: Resistivity measured by four-point-probing (inline, at room temperature) as a function of substrate temperature for sample prepared on glass substrates. Half circles on the top axis depict resistivity values that were too high to measure ($> 4 \times 10^4 \Omega cm$). Standard deviation results from measuring two samples and several measurement points around the center.

The resistivity of the films was obtained by four-point-probing and is shown in Figure 6.7. Films prepared below or within the ALD window (25–200°C) have a high resistivity, which was too high to measure with the available setup. Above the ALD window (225–250°C), films show a decrease in resistivity over several orders of magnitude, reaching around 10 Ωcm at 250°C. As already mentioned, the drop in resistivity accompanied by the increase of the absorption edge could be described by the Burstein-Moss effect. Kim et al. found a similar behavior in PE-ALD ZnO;¹⁰⁴ in their case, the resistivity dropped over 6 orders of

magnitude when increasing the substrate temperature from 225 to 300 °C. They showed that the decrease in resistivity was caused by an increase in carrier concentration. Further studies on thermal ALD ZnO showed that zinc interstitials can play a major role in the conduction mechanism of films deposited at a higher substrate temperature.^{152,153} It is fair to assume that in our case the drop in resistivity above the ALD window is caused by zinc-related defects. The drop in refractive index, the loss of excitonic absorption, and the slightly nonstoichiometric composition point in the same direction.

Regarding possible applications, films within the ALD window have high resistivity and strong (002) preferential orientation, both prerequisites for piezoelectrics.¹⁵⁴ On the other hand, films prepared (slightly) above the ALD window showed lower resistivity and high transmission, pointing out a possible application (with Al doping) for transparent conductive oxides.⁷⁰

6.6 CONCLUSION

In this contribution, the temperature-dependent growth of ZnO thin films, deposited by PE-ALD, was investigated. The growth per cycle was constant at $\approx 2.5 \text{ \AA cycle}^{-1}$ in the range of 125–200 °C, which was identified as the ALD window. The GPC within the ALD window was shown to be just below the lattice spacing of the (002) orientation (2.60 Å) pointing out a growth close to a monolayer-by-monolayer growth. Above the ALD window, the GPC started to increase rapidly with increased standard deviation, pointing out a possible CVD-component in the growth.

Structural and optical material properties were investigated, which showed a different behavior in regions closely related to the temperature regions defined by the GPC (below, within, and above the ALD window).

The specular orientation measured by XRD showed a (100) preferential orientation at 25 °C. The (002) peak increased with increasing temperature and became the preferential orientation within the ALD window and above.

The refractive index (at 633 nm) measured by SE exhibited a strong increase from 1.90 to 1.93 below the ALD window (25–100 °C). The increase slowed down for temperatures within the ALD window and slightly above (125–225 °C), reaching a value of 1.96 at 225 °C. Above the ALD window (250 °C), the refractive index dropped rapidly to 1.86. Similarly, the mass density showed two slopes below and within the ALD window and a decrease above the ALD window.

UV-vis spectroscopy showed that all samples were highly transparent ($\approx 90\%$ transmission) over most of the visible range. Samples prepared at temperatures within the ALD window and slightly above ($100\text{--}225\text{ }^\circ\text{C}$) exhibited a peak that could be attributed to excitonic absorption. The absorption edge was found to red shift with increasing substrate temperature until $225\text{ }^\circ\text{C}$ and increased again at $250\text{ }^\circ\text{C}$ (possibly due to the Burstein-Moss effect).

The resistivity of the samples (measured at room temperature) was very high ($> 4 \times 10^4\ \Omega\text{cm}$) for samples below and within the ALD window and dropped above the ALD window to $10\ \Omega\text{cm}$ at $250\text{ }^\circ\text{C}$.

Regarding device applications, ZnO films prepared below the ALD window could be useful for application on thermosensitive substrates in which polycrystalline films are necessary. Films prepared within the ALD window are more textured, exhibit excitonic absorption, and have high resistivity. Typical application fields would be therefore in optical devices such as UV-lasers or piezoelectrics. Films prepared above the ALD window show a drop in resistivity and could therefore be used as a basis for transparent conductive oxides, however exhibiting less uniform growth.

6.7 ACKNOWLEDGMENTS

This project has received funding from the European Research Council (ERC) under the European Union's Horizon 2020 research and innovation program (Grant Agreement No. 715403).

6.8 SUPPORTING INFORMATION

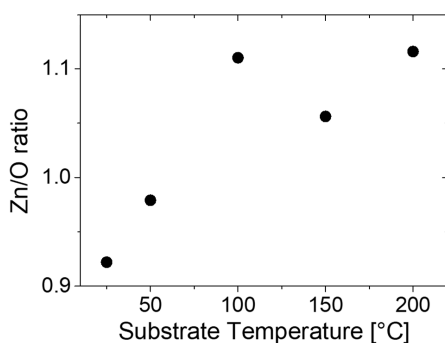


Figure 6.8: Zn/O ratio as a function of substrate temperature obtained by XPS for samples prepared on Si.

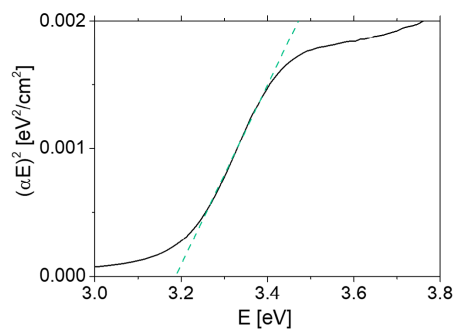


Figure 6.9: Tauc fit from UV-Vis measurements for a sample prepared at 150 °C on a quartz substrate.

7

Initial Growth and Crystallization Onset of Plasma Enhanced-Atomic Layer Deposited ZnO

7.1 PREFACE



Article

Initial Growth and Crystallization Onset of Plasma Enhanced-Atomic Layer Deposited ZnO

Alberto Perrotta ^{1,†}, Julian Pilz ^{1,†}, Roland Resel ¹, Oliver Werzer ² and Anna Maria Coclite ^{1,*}

The work was conducted at Graz University of Technology and collaboration with Oliver Werzer of University of Graz. Author contributions: Conceptualization, methodology, implementation and writing: A.P. and J.P.; AFM methodology and data curation, O.W.; XRR data curation: R.R.; writing—review and editing, A.P., J.P., A.M.C., O.W., R.R.; supervision, A.M.C., R.R.; funding acquisition, A.M.C. All authors have read and agreed to the

published version of the manuscript. Alberto Perrotta and Julian Pilz share the first authorship. The following text and images are identical to the published work:

- Perrotta, A.; Pilz, J.; Resel, R.; Werzer, O.; Coclite, A. M. Initial Growth and Crystallization Onset of Plasma Enhanced-Atomic Layer Deposited ZnO. *Crystals* **2020**, *10* (4), 291.

7.2 ABSTRACT

Direct plasma enhanced-atomic layer deposition (PE-ALD) is adopted for the growth of ZnO on c-Si with native oxide at room temperature. The initial stages of growth both in terms of thickness evolution and crystallization onset are followed ex-situ by a combination of spectroscopic ellipsometry and X-ray based techniques (diffraction, reflectivity, and fluorescence). Differently from the growth mode usually reported for thermal ALD ZnO (i.e., substrate-inhibited island growth), the effect of plasma surface activation resulted in a substrate-enhanced island growth. A transient region of accelerated island formation was found within the first 2 nm of deposition, resulting in the growth of amorphous ZnO as witnessed with grazing incidence X-ray diffraction. After the islands coalesced and a continuous layer formed, the first crystallites were found to grow, starting the layer-by-layer growth mode. High-temperature ALD ZnO layers were also investigated in terms of crystallization onset, showing that layers are amorphous up to a thickness of 3 nm, irrespective of the deposition temperature and growth orientation.

7.3 INTRODUCTION

Zinc oxide (ZnO) is a II-VI semiconductor, well-studied because of its unique qualities. As thin films, it has been researched for an increasing number of optical and electronic devices, and the tunability of its physical-chemical properties is still investigated in various scientific fields.^{155,156,157,81} To name a few, it possesses a wide direct bandgap (≈ 3.37 eV) and large excitonic binding energy (60 meV), which is useful for near-UV optoelectronics and lasing applications.^{158,56} Furthermore, it is applied as a transparent conductive oxide due to the possibility to tune its electrical properties via doping, e.g., aluminum doping.^{159,130}

Several vapor phase methods are adopted for the deposition of ZnO thin films, such as sputtering,¹⁶⁰ pulsed laser deposition,¹⁶¹ and atomic layer deposition (ALD). ALD, either

thermal or enhanced by plasma (PE-ALD), has often been adopted as the method of choice to deliver high quality (ultra-)thin ZnO films.^{81,104,162,163,164,165,166} Polycrystalline thin films were obtained down to room temperature.^{81,110,134} PE-ALD is known to deliver ZnO of higher quality compared to thermal ALD, with a fewer number of defects (e.g., oxygen vacancies and Zn interstitials) and a higher mass density, both at room and elevated temperatures.^{81,104,112,167} The highly reactive species formed in the plasma phase are considered the key aspect for the improved material quality, contributing to a more efficient removal of the organic ligands in the ALD Zn-organometallic precursor, and generally an improved crystallogenic packing.^{6,27}

Recently in the literature, great attention has been given to the initial stages of growth of ZnO by thermal ALD.^{168,169,170,171,172,173,174,175} Understanding the first stages of growth is of particular importance when ultrathin and continuous ZnO films are required, e.g., as an electron buffer layer for inverted solar cells,⁸¹ or as a passivation layer in transistors.^{176,177} Depending on the temperature and substrate material adopted, the growth was found to be from island-like to layer-by-layer or epitaxial, highlighting the great influence of these parameters in the growth stages. Following the growth mode schemes presented by Puruunen and Vandervorst,¹⁴ ZnO grown by ALD generally showed a substrate-inhibited growth.

Together with the initial growth, the onset of crystallization represents another critical aspect when the first stages of the deposition of materials are investigated. The first crystalline units could develop as early as the first atomic layer or in a later stage of deposition and the details can depend on the growth orientation, interaction with the substrate and/or the adopted method (e.g., if thermal or plasma enhanced-ALD).²⁷ Compared to the initial growth stages, the onset of crystallinity has not received the same attention. In a series of investigations on thermal ALD ZnO, Renevier, Ciatto et al. reported on the growth of ZnO when deposited on different substrates (a-SiO₂,^{171,172,173} c-Al₂O₃,^{171,172,173} In_{0.53}Ga_{0.47}As^{174,175}). The in-situ methodology adopted (mainly X-ray based methods, such as X-ray fluorescence and X-ray absorption near-edge structure spectroscopy) identified the onset of crystallization to start from the very first cycle when deposited on c-Al₂O₃, adopting a 2D-like growth and developing in-plane crystallinity; a different growth behavior was instead observed when deposited on a-SiO₂ and In_{0.53}Ga_{0.47}As, on which the crystallinity starts after the development of an initial amorphous layer.

In this contribution, the initial growth and onset of crystallization of ZnO is investigated by adopting a direct plasma-enhanced ALD (PE-ALD) approach, thus highlighting the role of plasma surface activation. The initial stages of growth of inorganic materials have been

seldom investigated for PE-ALD,^{178,64,179} and the specific nucleation of crystallites adopting plasma as co-reactant has not been reported for ZnO. Following the studies on room¹³⁴ and high temperature deposition of ZnO by direct PE-ALD, the evolution of the material properties is investigated with a combination of several ex-situ analysis techniques.

7.4 EXPERIMENT

A custom-built direct plasma ALD reactor was used to deposit ZnO thin films on single side polished c-Si (100) substrates (Siegert Wafer, Aachen, Germany) with native oxide. Details on the system can be found in previous publications.^{134,65,66,67} The pressure in the reactor was controlled via a manual gate valve, set to a fixed opening to reach a pressure of around 85 mTorr during plasma exposure. Pure oxygen was used during the plasma step (step A, plasma power 60 W, duration 6 s for O₂ exposure) and Ar was adopted in the purging step. The flow rates for O₂ and Ar were set at 20 sccm during the plasma and the purging step, respectively. Diethyl zinc (DEZ, Sigma-Aldrich, Darmstadt, Germany, CAS 557-20-0) was used as the metalorganic precursor (step B, duration 150 ms). The purging times were set at 12 s and 15 s for step A and B, respectively. The cycles always started and ended with a plasma step, as follows: (A-B)n-A, with n the number of cycles. The last plasma step was adopted to ensure the removal of the organic ligands of DEZ also on the surface of the layer. Sets of samples were deposited at constant temperatures in the range from 25 to 250 °C.⁶⁷ Thickness variation of the films was achieved by varying the number of cycles.

Spectroscopic ellipsometry (SE) (J.A. Woollam M-2000V, Lincoln, NE, USA) was used to determine the thickness and optical properties of the films after deposition. The measurements were carried out at three different angles (65°, 70°, and 75°) in a wavelength range from 370 to 1000 nm. The analysis of the spectra was performed with the software CompleteEASE® (J.A. Woollam, Lincoln, NE, USA). The thickness was determined by applying a three-layer model consisting of a semi-infinite silicon substrate, a native silicon oxide layer with a fixed thickness of 1.3 to 2 nm (measured before each deposition), and a Cauchy layer, as follows

$$n(\lambda) = A + \frac{B}{\lambda^2} + \frac{C}{\lambda^4} \quad (7.1)$$

where n is the wavelength-dependent refractive index, λ is the wavelength and A , B , and C are fit parameters. The fitting was limited to the transparent region of ZnO, i.e., 450–1000 nm.

To verify the robustness of the model adopted, the analysis was extended to a wavelength range close to the bandgap of ZnO (generally reported at 375 nm). An oscillator model

was also adopted, extending the wavelength range to 370 to 1000 nm. The oscillator model consisted of Gaussian oscillators to account for the high- and near infrared-energy contributions and a PSEMI-Mo model to account for the near-bandgap absorption. The PSEMI-Mo model is an oscillator with a sharp onset and Kramers–Kronig consistent properties consisting of four connected polynomial spline functions.¹¹⁵ The two models were found to deliver comparable results for the thickness investigated, and thus, the Cauchy model was preferred due to the lower number of variables adopted.

As a complementary technique to ellipsometry, X-ray reflectivity (XRR) measurements were performed to determine the film thickness and density as well as the surface and interface roughness. A PANalytical Empyrean diffractometer (Malvern Panalytical, Kassel, Germany) utilizing monochromatized copper radiation with a wavelength $\lambda = 1.5418 \text{ \AA}$ was used. The beam was narrowed by a $1/32^\circ$ divergence slit and a 10 mm beam mask. Its PIXcel3D-detector was operated in receiving slit mode, facilitating the Po.1 antiscatter slit. Two different fitting procedures were applied to explain the experimental data: a model-dependent and a model-independent approach. For the first, fitting of the measured data was performed with the software X'Pert Reflectivity (Panalytical, The Netherlands) applying a three-layer model consisting of a semi-infinite Si substrate, a native SiO₂ layer, and a ZnO layer. The fit parameters in the model were the ZnO layer thickness, density, and surface roughness as well as the interface roughness with the native SiO₂ layer on the c-Si. The approach here used a segmented algorithm to fit the model onto the experimental data. The second fitting method is a stochastic model-independent electron density profiles variation using the software Stochfit.¹⁸⁰ A scattering length density (SLD) of 19.5 was chosen for the subphase (SiO₂) and the initial value for the film SLD was 40. For sake of simplicity, the initial value for the film thickness was the one obtained by the other fit using the X'Pert Reflectivity software and the number of boxes was 1.5 times this value.

Grazing incidence X-ray diffraction (GIXD) was performed on the thin films of ZnO to investigate the in-plane orientation of the crystallites with respect to the silicon oxide surface. The measurements were conducted at the synchrotron Elettra (Trieste, Italy) using the XRD1-beamline.¹⁸¹ The wavelength was set at 1.4 Å and an incident angle α of 1.2 to 2° was chosen to minimize footprint artifacts. Diffracted intensities were collected on a Pilatus 2M detector and all data have been recalculated to reciprocal space maps using the in-house developed software package GIDVis.¹⁸²

X-ray fluorescence (XRF) spectroscopy was performed with an PANalytical Epsilon 1 (Malvern Panalytical, Kassel, Germany) to obtain the relative Zn amount after different deposition

steps. X-rays were generated in an Ag anode X-ray tube using a voltage and current of 50 kV and 100 μ A, respectively. A 100 μ m Ag-filter was used in the measurements, and the intensity of the Zn- K_{α} peak at 8.63 keV was evaluated.

Atomic force microscopy (AFM) was performed in non-contact mode on a Nanosurf Easyscan 2 (Liestal, Switzerland) equipped with a C3000 controller. The tapping mode measurements were performed using a TAP-300 cantilever (BudgetSensors, Bulgaria). The correction of artifacts, plotting, and data evaluation were done with the freely available software package Gwyddion.¹⁸³ The samples were rinsed with water and 96% EtOH and dried for 5 minutes on a hot plate at 60 °C under constant nitrogen stream to obtain high quality images.

7.5 RESULTS AND DISCUSSION

7.5.1 THICKNESS AND MORPHOLOGY

ZnO thin films were prepared at room temperature by PE-ALD, as previously reported,¹³⁴ and the thickness was varied by varying the number of cycles from 1 to 50 resulting in a maximum thickness of about 8 nm. X-ray reflectivity (XRR) measurements of the respective samples were carried out to follow the evolution of the thickness of the growing ZnO (Figure 7.1).

The XRR curves in Figure 7.1a show a high intensity for low angles, which is the region of total reflection. At the critical angle (around $2\theta = 0.44-0.47^{\circ}$), the intensity rapidly drops showing the capability of the X-ray beam to penetrate into the layer. Typically, the angle is related to the electron density of the top layer, but as ZnO is thin and the native SiO_2 layer has a comparable thickness value, useful information on the density cannot be directly extracted. After the critical angle, the intensity decays further for higher angles according to Fresnel's law. By increasing the thickness of the top ZnO starting from one cycle, Kiessig fringes appear in the curves due to thickness-dependent interference effects visible in a clear minimum between 3 and 4.5°. The period of these fringes decreases with increasing number of cycles; thus, it is inversely correlated to the thickness. Using a model-dependent fitting, film properties such as the thickness, density, and surface and interface roughness can be derived from the XRR curves. The modelled thickness as a function of the number of cycles is shown in Figure 7.1b. For the first few cycles (up to 10 cycles), the thickness increases rapidly. After this transient growth region, the rate slightly decreases and shows a linear behavior throughout the investigated range (50 cycles). Differentiating the thickness vs. number of cycles curve, the growth per cycle (GPC) can be obtained (Figure 7.1c). The GPC is about 0.85 nm for

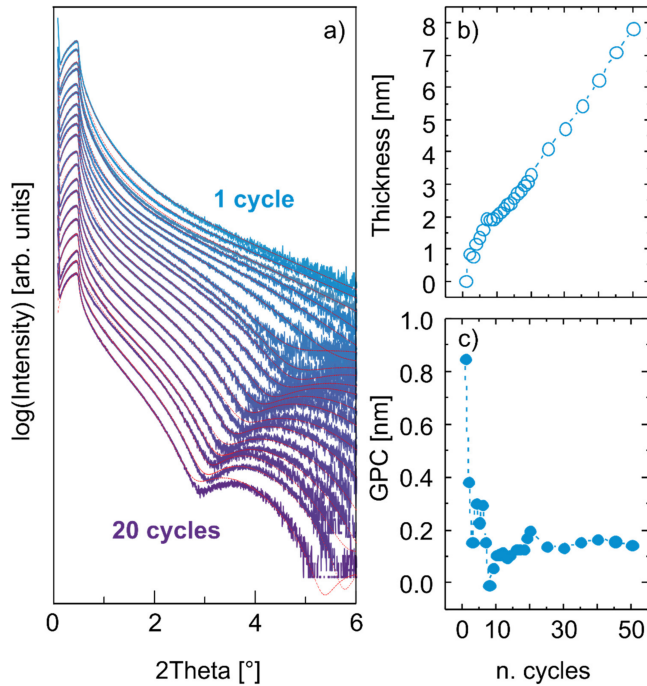


Figure 7.1: (a) XRR curves of the first (top) up to the 20th (bottom) PE-ALD ZnO cycle; the curves are stacked for clarity. The fitting curves are also reported with a red dashed line; (b) modelled ZnO layer thickness as determined from the XRR curves adopting a three-layer model vs. number of cycles; (c) growth per cycle (GPC) calculated from the XRR-derived thickness for all samples.

the first cycle, and afterwards decreases with the numbers of cycles. After 10 cycles the GPC was found constant with a value of around 0.16 nm and does not appear to change up to 50 cycles.

Puurunen et al.¹⁴ proposed four different models to describe the variation of the GPC in the initial stages of the growth. These are 1) linear growth (constant GPC for all number of cycles), 2) substrate-enhanced growth (higher GPC in the beginning followed by a decrease to a constant value), 3) substrate-inhibited growth type 1 (lower GPC in the beginning followed by an increase to a constant value, and 4) substrate-inhibited growth type 2 (first increase to a maximum and then decrease to constant value). Following this classification, the GPC trend shown in Figure 7.1c can be identified as substrate-enhanced growth. The first cycle shows the highest difference to the steady-state value and the GPC for 2 to 8 cycles rapidly drops to 0.16 nm. In the literature, for the initial growth of thermal ALD of ZnO, the GPC behavior is often reported with a “substrate-inhibited”-like behavior on different substrates such as a-SiO₂,¹⁶⁸ In_{0.53}Ga_{0.47}As,¹⁷⁴ and Al₂O₃.¹⁷⁰ In these studies, the first cycles of the ZnO growth

were characterized by island formation, with a limited thickness development, as measured by in-situ XRR and XRF. In our contribution, the effect of the oxygen plasma in direct contact with the substrate is believed to increase the number of reactive sites available for the DEZ molecules, enhancing the growth, similarly to the increase in hydrophilic properties of the Si wafers adopted in the semiconductor industry prior to wafer bonding.¹⁸⁴ A similar behavior was reported for the growth of AlN when comparing thermal and plasma enhanced-ALD.¹⁸⁵

With the purpose of better understanding the ZnO growth, additional material properties are shown in Figure 7.2, i.e., mass density, surface and interface roughness, derived from the fitting of the XRR data.

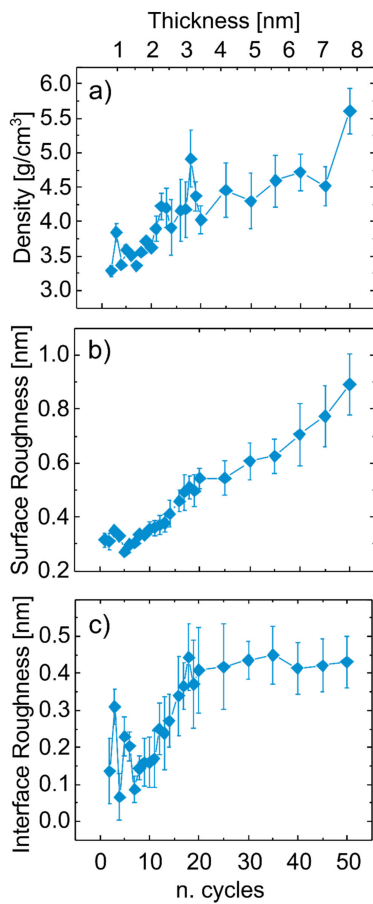


Figure 7.2: XRR-derived parameters (a) density, (b) surface roughness, and (c) interface roughness as a function of the number of cycles, showing the different phases of growth. The respective thickness development scale is also reported.

For the transient regime, the mass density fluctuates around a value of $3.5 \pm 0.2 \text{ g cm}^{-3}$, the roughness around a value of $0.32 \pm 0.02 \text{ nm}$ and the interface roughness around 0.19

± 0.06 nm. For more than 10 cycles, the mass density increases rapidly for a few cycles and slows down afterwards, with the values being between 4.2 ± 0.3 and 4.5 ± 0.3 g cm⁻³. These values increase for thicker films, up to a mass density of 5.6 g cm⁻³, as measured on a 30-nm-thick ZnO.⁶⁷ The surface roughness shows a fairly linear increase after 10 cycles and the interface roughness also increases at first until it reaches a constant value of around 0.4 nm at 20 cycles. The interface roughness values point out the completion of the interface between the ZnO layer and the a-SiO₂ above 10 cycles, suggesting the formation of a continuous layer in correspondence with a constant GPC, as shown in Figure 7.2c.

A model-independent method was also used to fit the data in Figure 7.1 to verify the robustness of the prior adopted three-layer model and exclude a mutual dependence of the model variables. The normalized electron density profiles of several films obtained are shown in Figure 7.3. Below six cycles, the fitting procedure did not converge to feasible results, indicating a highly structured surface and corroborating the hypothesis of a non-continuous layer in the first cycles of growth. After six cycles feasible results converged from the model independent fitting and some of the data are summarized in Figure 7.3. For $-1 < z < 0$ nm, the electron density values represent the c-Si substrate and are normalized to 1. The onset of the electron density increases at $z = 0$ nm, reflecting the electron density of the native oxide layer, which is about 1 nm for all samples. The electron density then rapidly increases and finally reaches plateau values which can be generalized in two groups; up until 10 cycles, the normalized electron density of the films is around 1.7, whereas for films above 10 cycles the normalized electron density saturates at around 2.0. The values of the reported electron density correspond to mass density values (assuming a stoichiometric ZnO film) of 3.1 and 3.7 g cm⁻³, respectively. The trend of the density (i.e., two plateaus for the transient and steady-state region) agrees well with the fitting using the model-dependent software. However, an offset of around 0.5 g cm⁻³ is apparent, which could be due to stoichiometric assumptions. In fact, thicker ZnO layers deposited at room temperature showed a lower mass density as bulk ZnO, as mentioned above. The roughness is represented by the slope of the electron density toward the surface to air, which is located at the right hand side of the curves or larger z values. The slope does not show large variations until 17 cycles, where it mildens, corresponding to an increase in surface roughness.

Both model-dependent (Figure 7.2) and model-independent (Figure 7.3) results identify the two distinct regions of growth. In order to further confirm the so-far observed trend, additional experimental techniques were employed. The thickness measured by SE and the Zn amount measured by XRF as a function of the number of cycles is shown in Figure 7.4.

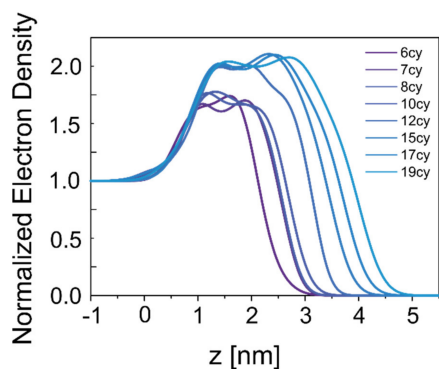


Figure 7.3: Normalized electron density profiles of a selection of XRR data as a function of the distance from the substrate. The electron density profiles were obtained with Stochfit.

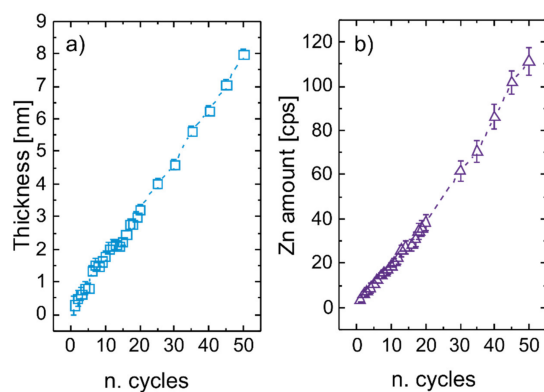


Figure 7.4: (a) Thickness vs. number of cycles as derived from SE; (b) Zn amount in cps from the XRF measurements.

The thickness by SE shows the same trend as the one obtained with XRR measurement, i.e., an initial region with a slightly enhanced growth followed by a transition to a steady-state growth. The roughness could not be implemented in the SE model without giving unphysical or non-significant values. For the amount of Zn measured by XRF, no significant deviation from a constant slope can be observed as function of the number of cycles. The slight difference in rate between the obtained thickness (by XRR and SE) and the zinc amount (by XRF) in the transient region might occur due to morphological considerations. This means that while the same zinc amount is deposited per cycle, as expected being in a self-limiting regime,¹³⁴ the measured thickness might not be the same due to changes in the structure and mass density. In order to complete the morphological picture of the ZnO layers and shed light on the initial growth modes, AFM height images of films prepared with different number of cycles at room temperature are shown in Figure 7.5.

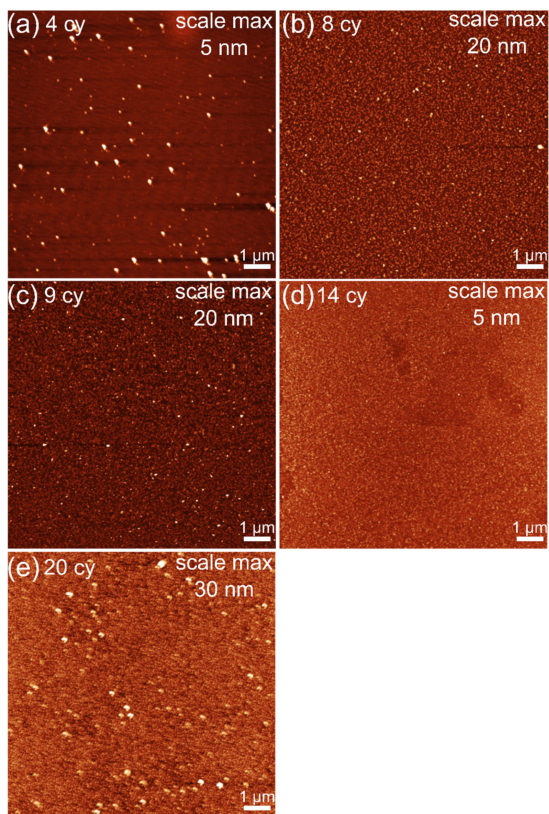


Figure 7.5: AFM height images of ZnO on Si substrates grown at room temperature with (a) 4, (b) 8, (c) 9, (d) 14, and (e) 20 PE-ALD cycles. Image size is $10 \times 10 \mu\text{m}$ for all images and the color bar maximum (white) is indicated in the figures.

The AFM images reveal scattered island deposited in the first cycles of deposition, similar to the work of Baji et al. for ZnO deposited at 150°C by thermal ALD.¹⁶⁹ For four cycles (Figure 7.5a), scattered islands are found on the surface and the coverage is below 2%. Line scans reveal larger islands with diameters of around 100 nm and heights of around 6 nm and smaller islands with a diameter of around 50 to 60 nm and height of around 1 nm. Increasing the number of cycles to 8 and 9 cycles (Figure 7.5b,c) leads to an increase in coverage to around 25% and the island height increases to a maximum of 3 to 4 nm, whereas the diameter stays around 50 nm. A coalescence of the islands resulting in a closed and smooth layer is observed at 14 cycles (Figure 7.5d), whereas the size of the coalescing islands is still around 50 nm. The stage at which a continuous layer is achieved (according to the AFM images around 14 cycles) is also in agreement with other investigated material properties. A large change in the mass density was shown for films grown after a similar number of cycles (see Figure 7.2 and Figure 7.3). Furthermore, the GPC settles to a constant value at this stage (Figure 7.1), which

indicates the initialization of the ALD-typical layer-by-layer growth. By further increasing the number of cycles to 20 cycles (Figure 7.5e), the roughness increases compared to the 14 cycles sample and there are areas with increased height. This increased height suggests the development of crystallites. Baji et al.¹⁶⁹ investigated the initial stages of growth of ZnO by thermal ALD on different substrates. The growth on Si (with native oxide) showed a similar trend for the morphology to our results, that is, scattered islands at 5 and 10 cycles, and a full coverage above 15 cycles. In a nutshell, the AFM results suggest an island growth for the initial stages whereas the number of islands with diameters of around 50 nm increases with increasing number of cycles (4 to 9 cycles). After forming a closed layer by coalescence (around 14 cycles), an increase in height and roughness is observed (20 cycles), suggesting the formation of crystallites.

In summary, the combination of XRR, XRF, SE, and AFM revealed an enhanced island-growth mode for direct plasma ALD on Si substrates. Scattered islands are formed in the first cycles, with a higher mass density compared to thermal ALD of ZnO, resulting in a higher apparent thickness of the growing layer. The plasma is believed to increase the number of available nucleation sites, which grow in number and height after every cycle. A higher mobility of the species on the surface is to be excluded, considering that the deposition is run at room temperature. On the contrary, the islands are forming and quickly growing in the first ALD cycles, supporting the hypothesis of an active role of the direct plasma in the formation of additional reactive sites. In the literature, Napari et al.¹⁸⁶ reported on a comparison between the growth of ZnO obtained by remote and direct plasma sources in PE-ALD at room temperature. They also reported a generally higher GPC for the direct plasma growth compared to the remote one, due to the higher flux density of plasma species actively contributing to the material growth. A continuous layer is formed between cycle 10 and 14, with a thickness of 2 nm. Mass density, surface and interface roughness are increasing steeply starting from this stage, while the GPC starts to have a constant value.

7.5.2 DEVELOPMENT OF CRYSTALLITES

The onset of the crystalline ZnO was also investigated, as polycrystalline ZnO layers with a 100 texture had been obtained for thicker layers grown at room temperature with PE-ALD.¹³⁴ To investigate the beginning of the crystallization, GIXD was performed on the films with different thickness. Such a measurement allows the gathering of structural information down to monolayers extension from the substrate. An example for a reciprocal space map of a ZnO film is shown in Figure 7.6a.

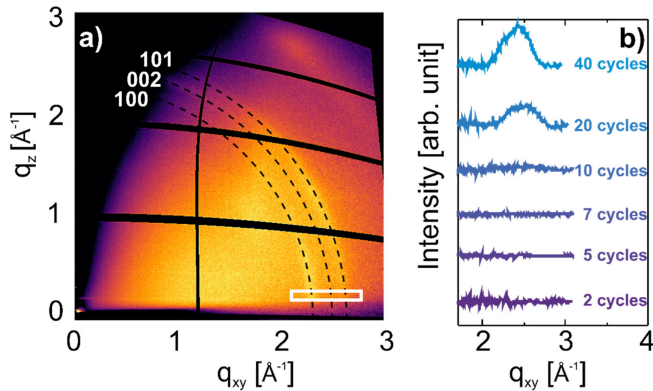


Figure 7.6: (a) Example of an GIXD pattern from a 50 cycle ZnO layer. Rings indicate the position of three Scherrer rings related to the polycrystalline ZnO; the white box shows the integrated area which was used to obtain information on the in-plane crystal formation. The integral density data is presented in (b) as intensity as a function of q for various ZnO layers prepared at room temperature of different thickness.

For polycrystalline samples, the so called Scherrer rings will appear in the space map, indicating the in-plane and near out-of-plane (excluding specular) orientation of the crystallites. To see at which cycle number crystalline features appear in the film, a linear integration was performed around the in-plane direction ($q_z = 0 \text{ \AA}^{-1}$) (indicated in Figure 7.6a). The intensity as a function of q_{xy} for samples of different thickness prepared at room temperature is shown in Figure 7.6b. For thicknesses up to 10 cycles, peaks cannot be observed. This either indicates an amorphous layer in the first stages of growth or the lateral (in-plane) size of the crystallites is too small so that not enough diffracted intensity can be generated to be detected. Starting from 20 cycles, a rather broad peak appears at around 2.5 \AA^{-1} . The deconvolution of such a peak allows for the distinction of a contribution at 2.41 \AA^{-1} , and 2.54 \AA^{-1} , attributed to the (002) and (101) orientation, respectively, when compared to the reference ZnO powder (26170-ICSD).¹³⁸ No signal from the (100) orientation at 2.23 \AA^{-1} is present. This is in agreement with the (100) preferential orientation in the specular direction previously reported at room temperature.^{134,65,67} When integrating the signal for the in-plane orientation, a peak arises originating from the (002) planes perpendicular to the substrate surface. In the literature, the ZnO crystallization is generally reported as island crystallites growing and coalescing before giving a layer-by-layer growth.²⁷ In a series of works on the initial growth of thermal ALD of ZnO, Ciatto et al.^{171,172,173} focused on the crystal formation in the early stages of the ZnO growth. By means of in-situ X-ray based techniques, a 2D structure was identified in the first cycles of growth, with an in-plane crystallinity developing as early as from the second cycle when deposited on a-Si. A (001) fiber texture developed, together

with grains, showing no preferential texture. However, in this study, no grain growth was witnessed in the first 10 cycles, that is, until a continuous layer is formed. Instead, in our work the onset of the crystallization starts after the completion of a continuous layer. The first 2.5 to 3 nm of growth (corresponding to the first 20 cycles) are amorphous, indicating that the enhanced island growth has no long-range ordering. The onset of crystallization corresponds to the beginning of the layer-by-layer growth. Furthermore, mass density, surface and interface roughness have an abrupt change in trend after the onset, as mentioned above. The crystallites grow with the number of cycles, and for a thickness of 45 nm we earlier reported crystallite sizes close to 30 nm.¹³⁴ Thus, the crystallization is thought to start once a closed amorphous layer is formed. In the extensive review on the crystallization of inorganic materials by ALD, Puurunen et al.²⁷ identified three possible modes for the crystallization onset, schematically reported in Figure 7.7a–c.

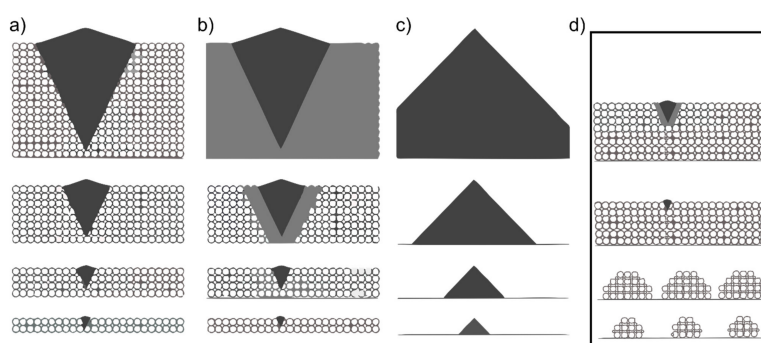


Figure 7.7: Schematics of different growth regimes of crystallites in ALD: (a) growth of crystallites from initial crystalline nuclei in an amorphous film; (b) growth of crystallites from initial crystalline nuclei in an amorphous film, inducing crystallization of the amorphous region next to the crystallite; (c) growth of the ALD layer directly from crystalline nuclei, in an island growth-like regime; (d) growth of the ALD layer in island growth-like regime starting from an amorphous material and developing crystallinity after the completion of a continuous layer. (a) to (c) were adapted from Ref.²⁷.

The initial growth of ZnO via direct-plasma enhanced ALD presented here shows an intermediate behavior between the crystalline island growth (Figure 7.7c) and the formation of an amorphous region, followed by formation in the amorphous material of the crystallite (Figure 7.7b). The formation of additional reactive sites on the substrate surface due to the direct plasma develops an initial amorphous growth of the ZnO clusters, followed first by a coalescence of the amorphous islands and formation of the initial crystal nuclei. Generally, for ALD the plasma was found to accelerate the onset of the crystallization.²⁷ However, earlier studies focusing on the (self-)texture development of ZnO adopting (plasma-based) sputtering or chemical vapor deposition methods highlighted the possibility of the formation of an

amorphous region prior to the crystallization onset.^{187,188} Moreover, an amorphous initial layer was also reported for thermal ALD of ZnO deposited on a-SiO₂¹⁶⁸ and recently on *In*_{0.53}*Ga*_{0.47}*As*.¹⁷⁴ In a recent in-situ study on the effect of annealing on PE-ALD ZnO, we demonstrated the presence of an amorphous fraction of material in the room-temperature-deposited ZnO,⁶⁵ supporting the hypothesis of its initial amorphous growth.

7.5.3 CRYSTALLIZATION AT HIGH TEMPERATURE

The ALD initial growth and crystallization studies reported so far investigated processes run at high temperature, i.e., starting from 100 °C. With the aim of verifying if the room temperature processes adopted in this study have an influence on the onset of crystallization, considering the lower surface mobility, higher sticking coefficient and lower energy of the species at this temperature, the same GIXD analysis was performed for samples with increasing thickness prepared at different substrate temperatures. The intensity plots for substrate temperatures from 50 to 200 °C are shown in Figure 7.8a–d.

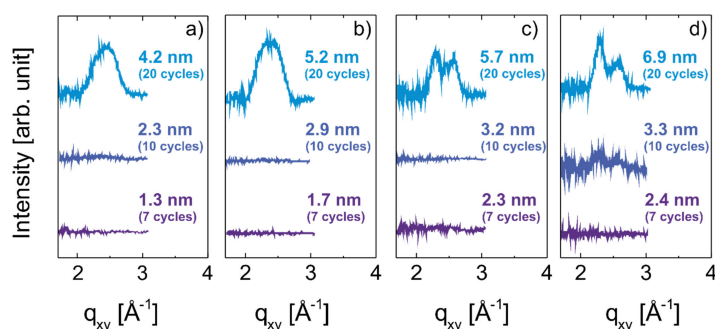


Figure 7.8: GIXD intensity as a function of q for ZnO layers of different thickness (7, 10, and 20 cycles) and deposited at different temperatures: (a) 50 °C, (b) 100 °C, (c) 150 °C, and (d) 200 °C. Irrespective of deposition temperature and preferred orientation (100 or 002), the crystallinity develops at above 3 nm.

Similar to the room temperature sample, a peak appears above 3 nm, irrespective of the substrate temperature. (Figure 7.8a–c). Starting from 150 °C, peaks corresponding to the (100) and (101) in-plane orientation are distinguishable and show similar intensity. For the sample prepared at 200 °C (Figure 7.8d), peaks can be observed already at 3.3 nm. Compared to the 150 °C sample, the (100) in-plane orientation shows an enhanced intensity. This temperature dependence of the preferential orientation is known and has already been shown in the literature for thicker films.^{107,106} Considering that the growth per cycle increases with increasing temperature (i.e., the same number of cycles at higher temperature results in a thicker film

than for a lower temperature), the development of crystallinity seems to happen at a thickness above 3 nm, irrespective of the crystalline orientation and deposition temperature. This result excludes the contribution of these parameters in the formation of an initial amorphous layer and corroborates the hypothesis of the role of the direct plasma in enhancing the initial growth at the expenses of the long-range order.

7.6 CONCLUSIONS

The initial growth of polycrystalline ZnO deposited at room temperature by direct PE-ALD on Si with native oxide is investigated. Different ex-situ characterization methods (XRR, SE, XRF, and AFM) allowed the identification of an additional growth mechanism for inorganic materials deposited by ALD. An accelerated island growth was found to occur in the first stages of layer formation, with a behavior in between the classical substrate-accelerated and island growth previously identified for inorganic ALD layers. In the initial 14 to 20 cycles, corresponding to 2.5 to 3 nm of material, an elevated number of islands of ZnO are forming. Increasing the number of cycles, the islands were found to coalesce and a classical layer-by-layer mechanism was identified. Furthermore, by adopting synchrotron radiation GIXD, the onset of crystallization was studied. Differently from the classical ALD island growth model, amorphous islands are grown in the first stages. The first crystallites are formed after the islands coalesce, that is, starting from roughly 3 nm. The direct plasma adopted as co-reactant is believed to accelerate the island formation and prevent an initial crystallization by increasing the number of reactive sites present on the substrate surface. The onset of crystallization was additionally studied at high temperature to better identify the origin of the late crystallite formation. Irrespective of temperature and crystal orientation, an amorphous layer with a minimum thickness of 3.2 nm was witnessed. This investigation extends the knowledge on the initial growth of inorganic materials adopting ALD and highlights the need for further efforts in studying the role of plasma in deviating from the classical growth-models.

7.7 ACKNOWLEDGMENTS

This research was funded by European Research Council (ERC) under the European Union's Horizon 2020 research and innovation program (grant agreement 715403). The authors thank Elettra Sincrotrone Trieste for the allocation of synchrotron radiation beamtime and L. Barba and M. Polentarutti for aiding with the beamline XRD1. Open Access Funding by the Graz University of Technology is also gratefully acknowledged.

8

Piezoelectric Properties of Zinc Oxide Thin Films grown by Plasma-Enhanced Atomic Layer Deposition

8.1 PREFACE

The work was conducted at Graz University of Technology and Joanneum Research in Weiz with a collaboration with Markus Kratzer and Christian Teichert from Montanuniversität Leoben. The author of this thesis performed sample preparation, XRD characterization, data analysis, and wrote the manuscript. Taher Abu Ali performed sample preparation, macroscopic piezoelectric characterization, data analysis, and wrote the manuscript. Philipp Schöffner assisted in evaluation of piezoelectric measurements. Markus Kratzer performed and analyzed PFM measurements. Christian Teichert supervised and analyzed PFM measurements. Barbara Stadlober and Anna Maria Coclite supervised the project. All authors reviewed the manuscript. Taher Abu Ali and the author of this thesis share the first authorship. The following text and images are identical to the submitted manuscript which is currently under review:

- Abu Ali, T; Pilz, J.; Schöffner, P.; Kratzer, M.; Teichert, C.; Stadlober, B.; Coclite, A. M. Piezoelectric properties of zinc oxide thin films grown by plasma-enhanced atomic layer deposition. *Under Review*

8.2 ABSTRACT

Zinc oxide (ZnO) thin films are deposited by plasma-enhanced atomic layer deposition (PE-ALD). This deposition method allows depositing stoichiometric and highly resistive ZnO films at room temperature. Despite such important requirements for piezoelectricity being met, not much is known in literature about the piezoelectric properties of ZnO thin films (< 70 nm) deposited by PE-ALD. The films were grown at different substrate temperatures to investigate the crystalline and piezoelectric properties. Films deposited on flexible polyethylene terephthalate (PET) generated higher piezoelectric current (> 1.8 nA) and charge (> 80 pC) compared to films deposited on glass (> 0.3 nA and > 30 pC) due to bending effects of the substrate when mechanically excited. Furthermore, increasing the substrate temperature, during the deposition, enhances the growth along the (002) crystallographic orientation, which further strengthens the generated piezoelectric current signal for mechanical excitations along the ZnO film's c-axis.

8.3 INTRODUCTION

Zinc oxide (ZnO) has attracted a lot of interest in material research due to its wide band gap energy (3.37 eV),¹⁸⁹ high excitonic binding energy (60 mV)¹⁰⁵ and relatively high piezoelectric coefficients ($d_{33} = 11.67$ pC/N⁻¹ and $d_{31} = -5.43$ pC/N⁻¹, for bulk ZnO).¹⁹⁰ Such properties, associated with its wurtzite structure, make ZnO of particular interest in many applications which include electronics (transparent electrodes and transparent thin film transistors),^{189,191} optoelectronics (laser diodes and solar cells),^{105,192} sensors (chemical, piezoelectric and pyroelectric),^{55,193} transducers (surface acoustic wave devices),¹⁹⁴ and energy harvesting.⁵⁷ Additionally, ZnO is an n-type semiconductor, where its semiconducting properties are tuned by doping, annealing, and most importantly by the growth process and related process parameters. Therefore, several techniques have been implemented to synthesize ZnO bulk crystals or films and to tailor their properties for different applications.⁵⁶ Of particular interest is atomic layer deposition (ALD).⁵⁶ It allows the deposition of uniform and conformal ZnO thin films with Å-level precision.^{81,4} Uniformity and conformality are products of self-limiting layer-by-layer film growth from vapour phase precursors, with each precursor dosing step being separated by a purging step. Common ALD processes include thermal ALD and plasma-enhanced ALD (PE-ALD). PE-ALD allows for the deposition of high-quality films at lower substrate temperature compared to thermal ALD as the surface reactions are driven by energetic plasma species rather than thermal energy.⁶ Such low deposi-

tion temperatures are suitable for ZnO growth on flexible substrates such as polymers, while maintaining control over films' optical, electrical, and mechanical properties.^{134,67} Similarly, the piezoelectric properties of ZnO films are influenced by the deposition technique and the growth parameters. Table 8.1 shows the piezoelectric coefficient d_{33} of ZnO films prepared by several deposition techniques as reported in literature.

Table 8.1: Reported piezoelectric coefficient d_{33} of ZnO films.

| Technique | Film thickness [nm] | d_{33} [pmV ⁻¹] |
|-------------------------|---------------------|-------------------------------|
| PLD | 200 | 12 ¹⁹⁵ |
| PLD | 50 | 25 ¹⁹⁶ |
| PLD | 800 | 49.7 ¹⁹⁷ |
| RF magnetron sputtering | 285 | 5 ¹⁹⁸ |
| RF magnetron sputtering | 710 | 5.3 ¹⁹⁸ |
| RF magnetron sputtering | 1400 | 8 ¹⁹⁸ |
| DC sputtering | 210 | 110 ¹⁹⁹ |

The investigation of the piezoelectric properties in these studies were performed by piezo response force microscopy (PFM), which measures the indirect piezoelectric effect, i.e., the reported values result from a local microscopic effect.^{200,201,77} Macroscopic piezoelectric properties can be measured with a stamp setup, which excites the piezoelectric material mechanically and measures the direct piezoelectric effect. While the piezoelectric characterization has been reported for ZnO films grown by different techniques, literature on piezoelectric properties of ZnO films prepared by ALD is very limited.²⁰² Nevertheless, ZnO deposited by ALD and especially PE-ALD has shown ideal properties for piezoelectric applications such as polycrystallinity with (002) texture,^{67,104,107} high resistivity,^{67,104} and low amount of impurities.^{134,104,110,106} Furthermore, the high reactivity of the plasma co-reactant allows for the deposition on thermo-sensitive substrates at substrate temperatures as low as room temperature.^{134,67} This study therefore focuses on the piezoelectric properties of ZnO thin films grown on flexible PET and rigid glass substrates at different substrate temperatures.

8.4 RESULTS

Since the crystallographic properties have a large effect on the piezoelectric coefficients,^{203,154} X-ray diffraction was performed. The XRD spectra of ZnO thin films grown on ITO-PET and on glass at different substrate temperatures are shown in Figure 8.1a and 8.1b, respectively. The spectra are shown in a 2θ range in which peaks corresponding to the ZnO wurtzite

structure were observed. For all the measured spectra in Figure 8.1a, a decaying background can be observed, which can be associated with the amorphous PET substrate. The ZnO samples show a polycrystalline pattern with diffraction peaks which can be associated with the (100) and (002) crystallographic orientation of the ZnO wurtzite structure. By increasing the substrate temperature, the preferential orientation of the films switches from (100) to (002). By further increase of the substrate temperature beyond 150 °C, the contribution from the (100) orientation further diminishes. Furthermore, the (002) peak position shifts to higher angles with increased substrate temperature, mainly for the samples deposited on ITO-PET, which could be explained by decreased microstrain within the sample. As the *c*-axis is the polar axis in the hexagonal wurtzite structure, a strong (002) preferential orientation of the crystallites is desired to enhance the measured piezoelectric current.^{134,67,198,204,205}

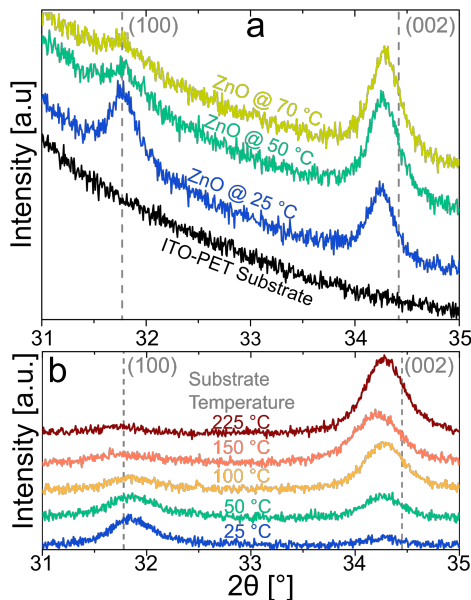


Figure 8.1: XRD patterns of ZnO films grown a) on PET and b) on glass at different substrate temperatures. Vertical, dashed lines show the peak positions of a ZnO powder reference (ICSD-26170).¹³⁸

The piezoelectric current signal *I* was measured as a function of time *t* upon periodic force cycles applied to the ZnO thin films by means of the setup shown in Figure 8.2.

Figure 8.3 shows the characteristic output plots for the films deposited at 25 °C a) on ITO coated PET substrate and b) on ITO coated glass substrate. Positive current pulses are generated upon pressing onto the sample and negative current pulses upon releasing the stamp from the sample. For such films, the average positive piezoelectric peak current generated

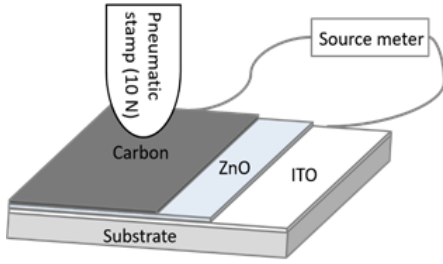


Figure 8.2: Schematic diagram of device architecture and piezoelectric measurement setup. Image not to scale, the area of the tip is 0.8 cm^2 and the sample size is 1.5 cm^2 .

from one cycle was $1.8 \pm 0.1 \text{ nA}$ when deposited on PET and $0.3 \pm 0.1 \text{ nA}$ when deposited on glass. When the films deposited on ITO-PET were mechanically excited, a recoil current was detected upon pressing and releasing, due to the elasticity of the substrate.²⁰⁶ The piezoelectric charge Q was calculated by integrating the piezoelectric current over time, as shown in equation 8.1.

$$Q = \int Idt \quad (8.1)$$

Figure 8.3c shows the calculated piezoelectric charge Q , for ZnO thin films deposited on both flexible PET and rigid glass substrates at different substrate temperatures T , respectively. A linear increase of the piezoelectric charge for films on both substrates was observed. For ZnO on PET, increasing the substrate temperature to 50°C resulted in a piezoelectric peak current of $I = 3.6 \pm 0.1 \text{ nA}$, corresponding to a charge of $Q = 180 \pm 10 \text{ pC}$. Further increase of the substrate temperature to 70°C resulted in a piezoelectric peak current of $I = 5.8 \pm 0.1 \text{ nA}$ and $Q = 320 \pm 10 \text{ pC}$. The increasing linear trend, attributed to the enhancement of the (002) orientation with increased temperature, was measured also for the samples deposited on glass: in this case, at 50°C , the generated piezoelectric peak current was $I = 1.4 \pm 0.2 \text{ nA}$ and $Q = 65 \pm 8 \text{ pC}$. Reaching a maximum of $4.3 \pm 0.2 \text{ nA}$ ($Q = 190 \pm 10 \text{ pC}$) for samples deposited at 225°C .

Piezoelectric current/charge generated from ZnO thin films deposited on rigid glass substrates were lower compared to those generated by ZnO thin films on flexible PET substrates, due to bending effects of the substrate.²⁰⁷ Bending of PET substrates generates charges through the transverse piezoelectric effect (attributed to the d_{31} coefficient), which results in higher measured piezoelectric current/charge.²⁰⁸ However, ZnO films deposited on rigid glass substrates are not prone to bending, resulting in lower generated piezoelectric current/charge.

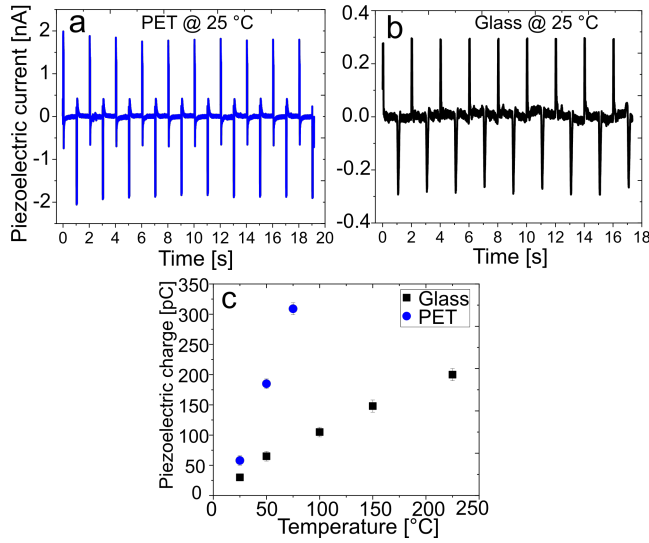


Figure 8.3: Piezoelectric current signal vs. time for 9-10 step force cycles applied to ZnO thin film deposited at 25°C a) on ITO coated PET b) on ITO coated glass. c) Generated piezoelectric charge as a function of the substrate deposition temperature for films grown on PET and glass.

As the response of ZnO films deposited on glass is not expected to have d_{31} contributions, the piezoelectric coefficient d_{33} can be calculated by

$$d_{33} = Q/F \quad (8.2)$$

where Q is the piezoelectric charge and F is the excitation force. The calculated d_{33} coefficients are shown in Table 8.2 below.

Table 8.2: Calculated piezoelectric coefficient for ZnO films deposited on glass substrates at different temperatures.

| Deposition temperature [°C] | d_{33} [pCN^{-1}] |
|-----------------------------|--------------------------------|
| 25 | 3.0 |
| 50 | 6.5 |
| 100 | 10.5 |
| 150 | 14.8 |
| 225 | 20.0 |

The calculated piezoelectric coefficient ranges between 3.0 pCN^{-1} and 20.0 pCN^{-1} , for ZnO films grown within the temperature range of 25 °C and 225 °C. The d_{33} values are comparable to those reported in Table 8.1. The results obtained from our in-house built piezoelectric setup allows macroscopic piezoelectric characterization of ZnO thin films. However, mi-

croscopic characterization using PFM, gives information about the local piezoelectric properties at a nanometer scale. Figure 8.4a shows the topography of ZnO film deposited at 25°C, which is characterized by small grains < 30 nm. The phase response (Figure 8.4b) does not show a coherent orientation of the grain polarization. However, large areas are recognizable, where the piezoelectric phase is ca. 180°. The piezo response (PR) amplitude (Figure 8.4c) is relatively low, with a maximum displacement of 20 pm. The incoherence of the phase response and the low amplitude can be explained by the crystallographic properties of the film, i.e. where the wurtzite ZnO structure is mostly oriented along the (100) axis. Figure 8.4d shows the topography of ZnO film deposited at 225°C, which is characterized by a granular topography with grain diameter of ≈60 nm. The PR amplitude signal (Figure 8.4f) follows the grain structure, where regions with higher piezoelectric displacement are mostly located within the grains, while at the grain boundaries, the displacement is lower. This could be attributed to the fact that the grain boundaries are crystallographic defects. From the PFM phase image (Figure 8.4e), a certain degree of phase shift is recognizable. The grains seem to be in-phase with the external AC driving voltage, while boundaries seem to be mostly out-of-phase. Considering that the wurtzite ZnO structure in this film is mostly oriented along the (002) axis, the PFM phase can be related with the grain polarization, being this in-phase, it corresponds to a Zn-terminating surface.

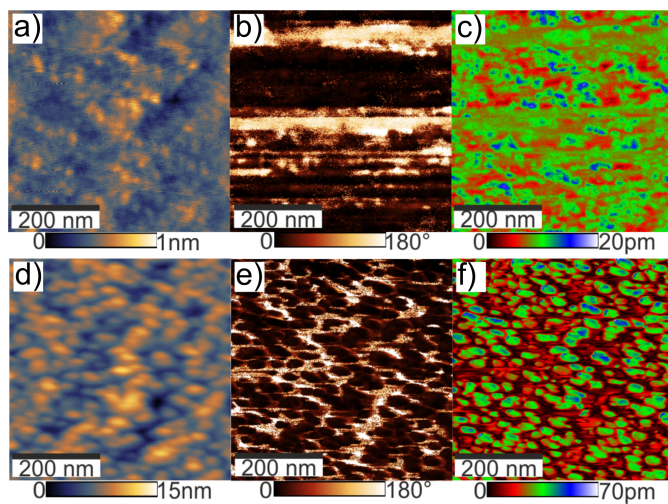


Figure 8.4: a) topography b) PR phase and c) PR Amplitude of ZnO at 25°C, d) topography e) PR phase and f) PR amplitude of ZnO at 225°C. Both films are grown on Si substrates.

8.5 CONCLUSION

Piezoelectricity in ZnO thin films deposited on flexible PET substrates as well as on rigid glass substrates by PE-ALD at different substrate temperatures was investigated. For this purpose, the piezoelectric current/charge was macroscopically measured and evaluated with an in-house built piezoelectric measurement setup, applying a periodic step force signal of 10 N. ZnO films grown on flexible substrates showed increased piezoelectric output (up to 320 pC) compared to films grown on rigid substrates, possibly due to contributing bending effects upon force application. Furthermore, films showed increased piezoelectric output with increasing substrate temperature for both substrates, which can be related to an enhanced orientation of the crystallites along the polar (002) crystallographic axis. This is confirmed by PFM measurements which indicate a predominant polarization orientation in the film.

8.6 EXPERIMENTAL

ZnO thin films were grown by PE-ALD in an in-house-built direct plasma reactor. Details on the setup can be found elsewhere.^{134,67} One cycle of the process consisted of 0.15 s diethylzinc (DEZ) dose, 22 s Argon (Ar) purge, 8 s O₂-plasma (60 W power), and 15 s Ar purge. ZnO films were deposited on Si (100) wafers with native oxide (Siegert Wafer, cut to approx. 2 x 2 cm) for spectroscopic ellipsometry and piezo response force microscopy measurements and on PET coated with Indium Tin oxide (ITO; 60 Ω/sq surface resistivity) substrates (Sigma-Aldrich, Germany), as well as glass slides and glass coated with ITO (60 Ω/sq surface resistivity) substrates (Sigma-Aldrich, Germany) for crystallographic and macroscopic piezoelectric characterization. Depositions on ITO coated PET substrates were performed at substrate temperatures of 25 °C, 50 °C, and 70 °C. Due to the temperature dependent growth per cycle of the ALD process,¹³⁴ the number of cycles was adapted for each deposition series to reach a thickness of around 65 nm. Depositions on ITO coated glass substrates were performed at 25 °C, 50 °C, 100 °C, 150 °C, and 225 °C with resultant film thicknesses of around 50 nm.

Spectroscopic ellipsometry (SE, J.A. Woollam M-2000V) was performed on films grown on Si substrates to determine the thickness and optical constants of the films. Measurements were carried out in a wavelength range of 370–1000 nm at three different angles (65°, 70°, and 75°). Using a Cauchy model in the transparent region of the ZnO films (450–1000 nm), the thickness and refractive index of the films were extracted.

X-ray diffraction (XRD) in a θ/θ -configuration (Panalytical Empyrean) was performed

to analyze the specular crystal orientation of films grown on ITO/PET substrates as well as films grown on glass substrates. A $1/8^\circ$ divergence slit, a 4 mm mask, and a P7.5 antiscatter slit were used in the setup, and the detector was operated in 1D-mode. The macroscopic piezoelectric properties were measured in an in-house-built piezoelectric measurement setup. For this evaluation, conductive carbon tape (Science Services GmbH) was applied on the ZnO film, as a top electrode. The setup consisted of a pneumatic stamp generating a step force signal with magnitude $F=10$ N and frequency $f=0.5$ Hz. The generated piezoelectric current I was measured with a National Instruments PXIe-4139 source meter, for 9-10 cycles of step force. Piezoelectric charge Q values were calculated from the integrated current signal.

To confirm the trends of the macroscopic measurements, PFM measurements were performed on ZnO films grown on Si. The measurements were conducted utilizing an Asylum Research (Oxford Instruments) MFP 3D atomic force microscope using Ti/Ir coated ASYLELEC-01-R2 conductive probe with a nominal tip radius of (25 ± 10) nm and a cantilever spring constant of 2.8 ($1.4-5.8$) Nm^{-1} . In order to extend the applicable voltage range, a $10\times$ voltage amplifier F10A from FLC Electronics AB was interconnected between the AFM controller output and the AFM probe. For signal enhancement, the measurements were performed in Dual AC Resonance Tracking (DART) mode, exploiting the superior signal-to-noise ratio enhancement at contact resonance.²⁰⁹

8.7 ACKNOWLEDGEMENTS

This project has received funding from the European Research Council (ERC) under the European Union's Horizon 2020 research and innovation program (Grant Agreement No. 715403). T. Abu Ali and J. Pilz contributed equally to this work.

Part III

Vapor Phase Infiltration of ZnO

9

Vapor Phase Infiltration of ZnO into Thin Films of Cis-Polyisoprene (Natural Rubber)

9.1 PREFACE

The work was conducted at the School of Materials Science and Engineering at Georgia Institute of Technology. The author of this thesis performed sample preparation, characterization except for SIMS and XPS, data evaluation, and wrote the manuscript. Anna Maria Coclite and Mark D. Losego supervised the project. All authors reviewed the manuscript. The following text and images are identical to the submitted manuscript which is currently under review:

- Pilz, J.; Coclite, A. M.; Losego M. D. Vapor Phase Infiltration of ZnO into Thin Films of Cis-Polyisoprene (Natural Rubber). *Under Review*

9.2 ABSTRACT

Elastomers are an important class of polymers for many applications. Often, additives are added to the polymer matrix of elastomers to promote vulcanization or enhance physical or

chemical properties. In this study, vapor phase infiltration (VPI) is investigated for transforming unvulcanized cis-polyisoprene (from natural rubber) into an organic/inorganic hybrid material. Specifically, we examine single-cycle infiltration with diethylzinc (DEZ) and water to form infiltrated zinc oxide species. Interestingly, low-temperature pre-heating of the cis-polyisoprene acutely affects the processes of infiltration, including diffusivity, maximum solubility, and chemical reactivity. We attribute these effects to a combination of film relaxation and oxidation. Independent of thermal pre-treatments, all infiltration processes exhibited consistent zinc oxide loading irrespective of purge time between the DEZ and water doses, indicating the presence of a strongly bound intermediate state between the DEZ precursor and the cis-polyisoprene polymer. Increasing infiltration process temperature accelerates diffusion and lowers the maximum solubility, in accordance with Fick's law and gas phase sorption equilibrium. Resulting organic-inorganic hybrid films show enhanced resistance to dissolution in toluene, a good solvent for the pure polymer.

9.3 INTRODUCTION

Cis-polyisoprene is the main component of natural rubber.²¹⁰ In commercial applications, cis-polyisoprene is often vulcanized (i.e. cross-linked; in the case of natural rubbers often driven by sulfur compounds) and different components such as activators, accelerators, or fillers²¹¹ are added to the polymer to achieve desired properties. Activators and accelerators lower the process temperatures and accelerate the vulcanization process. ZnO is widely used as an activator in rubber manufacturing. An even distribution in the polymer matrix as well as the morphology of ZnO particles is key to its effectiveness in modulating vulcanization.^{212,213} Fillers are added to reinforce physical properties (mechanical, electrical, optical,...) and prominent examples are carbon black²¹⁴ and silica.²¹⁵ Similar to activators and accelerators, the size and distribution of fillers impacts the resulting properties.²¹⁶

As such, vulcanizates (i.e. cross-linked elastomer polymers with additives) are a prominent example of composite and often hybrid organic-inorganic materials. Polymers that make up these vulcanizates are a new opportunity for vapor phase infiltration (VPI), a solvent-free method for infusing inorganic materials into polymers. Unlike many other methods currently used, VPI incorporates the inorganic species homogeneously at the atomic level, and the species may be chemically bound or unbound to the polymer host.²¹⁷

VPI is capable of distributing the inorganic material uniformly inside polymers and the amount of loading can be tuned by infiltration hold times, pressures, and cycle numbers.^{218,219}

While VPI originated from the atomic layer deposition (ALD) community and shares similar precursor chemistries, the process mechanisms are substantially different. In ALD, precursors follow self-limiting surface reactions on the exterior of a material. In VPI, the gas-phase precursors are expected to sorb into the material (polymer), diffuse throughout that material, and eventually become entrapped within the material through either chemical reactions or other means. The mechanism for entrapment is important as it determines whether VPI processing can be run as an equilibrium or non-equilibrium process and whether the inorganic species form primary chemical bonds to the polymer host. These final hybrid materials are intermixed organic-inorganic hybrid structures with properties distinctly different from the original polymer.^{42,46} For example, VPI has been used to increase the toughness of spider silk,⁴⁸ increase the electrical conductivity of semiconducting polymers,²²⁰ and increase the solvent stability and separation performance of membranes.⁴⁹

A recent investigation examined the use of vapor phase infiltration to incorporate inorganic materials into block co-polymers containing a rubber (elastomeric) block. In this recent study, VPI with diethyl zinc and water was used to infiltrate ZnO into epoxidized and unepoxidized polystyrene-block-poly(1,4-isoprene) copolymers (PS-b-PI).²²¹ The authors found that even PS-b-PI (lacking strong functional groups) were effective templates for selective infiltration of the polyisoprene block, attributing it to factors such as increased miscibility of DEZ in the polyisoprene block. However, a concrete mechanism of infiltration of polyisoprene has not been reported in literature, despite the technological importance of this polymer.

Depending on a polymer's chemical structure, different mechanisms of infiltration may happen.⁷ In the case of non-reactive polymers, precursor molecules can diffuse into the polymer matrix and become weakly entrapped by physisorption or steric hindrance. However, by applying long purges, these weakly bound precursors should diffuse out of the matrix, leaving no loading within the polymer. For polymers with reactive functional groups, precursor molecules chemically bind to the available reactive groups and are not removed by long purges. This mechanism may further lead to cross-linking of the polymer chains. It is unclear to what extent the alkene functional groups in polyisoprene may play in entrapping metalorganic precursors in a VPI process.

This study aims to elucidate the fundamental kinetic and chemical mechanisms of zinc oxide VPI into cis-polyisoprene using DEZ and water precursors. The results expand the currently limited knowledge about VPI in rubber and provide a new possible technical application for VPI in introducing inorganic constituents to rubber polymers.

9.4 EXPERIMENTAL

Cis-polyisoprene was purchased from Sigma-Aldrich (431257, average $M_w \approx 38,000$ by GPC, made from natural rubber). 2 wt% solutions were prepared in toluene (Sigma-Aldrich) and stirred overnight. Thin films of polyisoprene (thickness 78 ± 2 nm ($n=100$) after coating) were deposited on single-side polished Si wafers (p-type, WRS Materials) and glass slides by spin coating (10 s, 2000 rpm). No cleaning procedures were applied to the substrates prior to coating except for nitrogen flow. Pre-heating of the films was performed at 80°C on a hot plate in air (thickness after 5 h pre-heating 68 ± 6 nm ($n=180$), thickness after 24 h pre-heating 47 ± 6 nm ($n=100$)). Note that the glass transition temperature for this polymer is around -64°C .²²²

Vapor phase infiltration (VPI) of the polymer films was performed in a custom-built system described earlier,⁴⁹ and was controlled via a tree-based control software.⁵⁹ The chamber was operated at a temperature of 60, 80, or 100°C . Diethylzinc (STREM Chemicals, 95% purity, DANGER: pyrophoric) was used as the metalorganic precursor, deionized water as the oxidizing co-reactant, and nitrogen (99.995% purified from air) as the purging gas (flow rate 250 sccm). One cycle of VPI was applied to the polymer films which consisted of purging for 3600 s (to release residual water and other vapors trapped within the polymer), pump down to base pressure (60 mTorr), chamber isolation, DEZ dose for 1 s (through a valve with $C_v = 0.27$, providing a chamber pressure of 0.2 Torr DEZ), hold in this static DEZ atmosphere for 20 s to 7200 s, purge for 300 s, pump down, chamber isolation, water dose for 5 s (reaching 2 Torr H_2O), hold in this static H_2O atmosphere for 1800 s, and purge for 300 s. For investigating the influence of purge time, the DEZ hold was fixed at 800 s and the purge time after DEZ was varied from 100 s to 232200 s (2.5 days).

Attenuated total reflectance infrared spectroscopy (ATR-FTIR) was performed to monitor the chemical changes of spin-coated films upon pre-heating and infiltration. For these studies, films were prepared on glass substrates to minimize background intensities. Spectra were collected on a Thermo ScientificTM NicoletTM iS5 FTIR spectrometer with an iD7 ATR accessory with a diamond crystal. The resolution was 4 cm^{-1} and the spectra were averaged over 128 scans.

Thicknesses and optical constants of pristine, infiltrated, and calcinated films were obtained by spectroscopic ellipsometry (SE; J.A. Woolam alpha-SE). Spectra were obtained in a wavelength range 380-900 nm at 70° (additionally 75° for calcinated films). The model to fit the data consisted of a (semi-infinite) Si substrate, 1.7 nm fixed native oxide, and a Cauchy

layer with thickness, A, B, and k as fit parameters. For better comparison of layer thickness and due to correlation of fit parameters, the generic oscillator library model for ZnO (Complete Ease 5.08 software) was used for calcinated films and only the thickness was fitted.

Inorganic loading within the polymer was determined with both X-ray fluorescence spectroscopy (XRF; Thermo Scientific Niton FXL FM-XRF) and calcination of the infiltrated films. XRF was used to measure the relative amount of Zn in the films after infiltration. For this purpose, the amplitude of the Zn K α peak at 8.637 keV was obtained by fitting a Gaussian to the spectrum. Spectra were recorded in general metals mode with a measurement time of 30 s. Infiltrated films were also calcined in a furnace (Barnstead Thermolyne 1400; ramp up to 650 °C for 20 min, hold for 30 min) to remove the polymeric template and leave only the ZnO fraction. This residual quantity of ZnO was then evaluated with spectroscopic ellipsometry. X-ray photoelectron spectroscopy was conducted with a Thermo Scientific K-Alpha system using a monochromatic Al-K α X-ray source (1486.6 eV) with a 60° incident angle and a 90° emission collection geometry (pass energy 200 eV) for survey elemental analysis.

Zinc concentration depth profiles of the infiltrated polyisoprene films were measured with time-of-flight secondary ion mass spectroscopy (ToF-SIMS, IONTOF, 5 Series). SIMS spectra were collected using oxygen ion sputtering (150 μm \times 150 μm , 2kV accelerating voltage) and bismuth analyzer (50 μm \times 50 μm) beams. Positive polarity was used to detect the Zn+, Si+, and C+ signals from the infiltrated polymer films.

Chemical stability was tested by immersing pre-heated and infiltrated films (on Si) in 10 ml of toluene. The thickness was monitored intermittently by ex situ spectroscopic ellipsometry.

9.5 RESULTS AND DISCUSSION

9.5.1 DEMONSTRATION OF DEZ + H₂O VPI IN CIS-POLYISOPRENE

Figure 9.1 illustrates that DEZ + H₂O VPI can successfully infuse ZnO into cis-polyisoprene films. Figure 9.1(a) shows an X-ray fluorescence spectrum (XRF) of a hybrid film and a blank Si wafer. The hybrid film shows a clear signal from the Zn K α transition (enlarged spectrum shown in the inset), whereas all the other peaks stem either from the Si wafer or the sample holder (the fluorescence signal from organic elements [$Z < 12$] are undetectable by this XRF). The strong XRF signal is indicative of the Zn being infiltrated throughout the entire film and not just a single atomic layer on the surface. Figure 9.1(b) shows an X-ray photoelectron spectrum (XPS) with the Zn, O, and C peaks, i.e. the components of the hybrid film, highlighted. The shown spectra serve as a preview on the infiltration of polyisoprene; in the

following paragraphs the infiltration mechanisms as well as the influence of the pretreatment of the polyisoprene films are examined in detail.

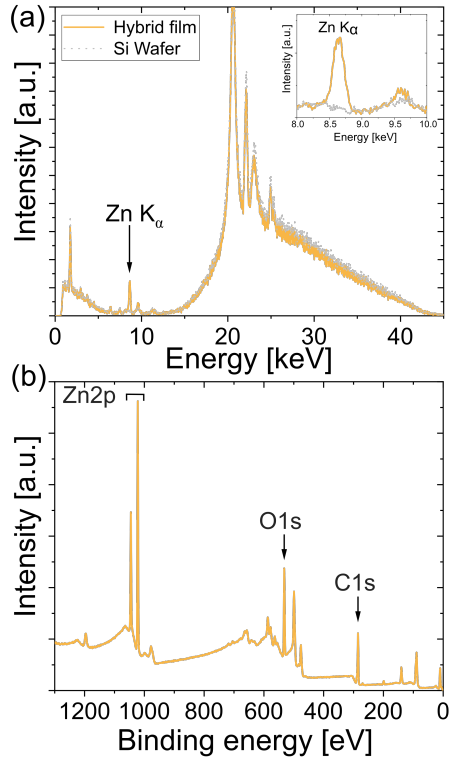


Figure 9.1: Exemplary X-ray spectra of hybrid films demonstrating that ZnOx was successfully loaded into the polyisoprene films. (a) X-ray fluorescence spectrum of a hybrid film and a blank Si wafer. The hybrid film displays a significant Zn K α signal whereas all the other peaks stem either from the Si wafer or the sample holder. (b) X-ray photoelectron survey spectrum from the surface of a hybrid film displaying Zn, O, and C components.

9.5.2 PRE-HEATING OF POLYISOPRENE FILMS

Early in our investigations of the VPI process on polyisoprene, we noted some unusual variations in the polymer relaxation when being pre-heated on the hotplate. A pre-heating step is typically used after spin coating a polymer film to remove solvent and relax the polymer structure. For polyisoprene, we found that this relaxation process appears to occur over a fairly long period of time, potentially many hours. Figure 9.2(a) plots the polyisoprene film thickness as a function of drying time (80 °C) for four independent trials (For trials 1-3, the thickness of the same individual film was monitored. For trial 4, each datapoint corresponds to the mean thickness of two individual samples, which were removed from the hotplate after the respective pre-heating times). While the thickness immediately after spin coating is

around 80 nm, all samples show a rapid thickness decrease for the first 5 to 10 h. After about 20 h, the thickness decrease slows and approaches a value between 40 and 50 nm (50 to 65% of the initial thickness). Initially, we attribute this reduction in thickness to a reduction in free volume of the polymer. Rapidly drying the polymer from solution via spin casting at room temperature often results in a metastable glass with high free volume. Even though the polymer is above T_g at room temperature, heating it should accelerate chain motion, relaxation, and reduce free volume, resulting in a reduction of the film thickness. However, as shown subsequently, it is likely that the changes in film thickness may be a combination of changes to both the free volume and polymer chemistry (e.g., an increase in cross-linking).

ATR-FTIR spectra were collected as a function of pre-heating time to interrogate potential chemical changes to the cis-polyisoprene films. The (scaled) IR spectra are shown in Figure 9.2(b). For unheated films (0 h), the FTIR spectrum shows the characteristic =C-H stretching, and CH₃ and CH₂ stretching and deformation modes of polyisoprene.^{223,224} The weak C=C stretching mode (1665 cm⁻¹) is not visible, which we attribute to the rather small thickness of the films. After 1 h of heating, an absorption peak attributed to C=O stretching (ketones, 1714 cm⁻¹) is apparent, indicative of partial oxidation. Longer heating durations (i.e. further oxidation) leads to more ketone groups as well as an increase in O-H stretching absorbance. At 4 h heating, an additional peak appears, which can be attributed to carboxylic acids (1766 cm⁻¹). Longer heating times lead to an increased absorbance in the O-H and C=O regions. These studies suggest continued oxidation of the polymer from ketones to alcohols to carboxylic acids with longer heat treatments. Thermal treatment of unvulcanized and vulcanized elastomers has been a field of significant research.^{225,226,227,228,229} In a study by Colin et al.,²²⁵ trans-polyisoprene is shown to oxidize in atmosphere similar to the behavior observed here via mechanisms such as chain-scission and cross-linking. Using molecular dynamics simulations, Li et al.²³⁰ show that (sulfur) cross-linking leads to shrinkage of cis-polyisoprene chains. While the exact mechanisms of oxidation and film shrinkage are difficult to ascertain, oxidation and subsequent cross-linking could be one factor in addition to polymer relaxation for the film shrinkage observed in Figure 9.2(a).

9.5.3 QUANTIFYING INORGANIC LOADING

Because pre-heating steps significantly affect the polyisoprene chemistry and structure, they are also expected to affect the infiltration process. To better understand this influence, we study infiltration of unheated, 5 h pre-heated (partially relaxed and oxidized), and 24 h pre-heated (close to fully relaxed and oxidized) films. Figure 9.3 summarizes the variations in zinc

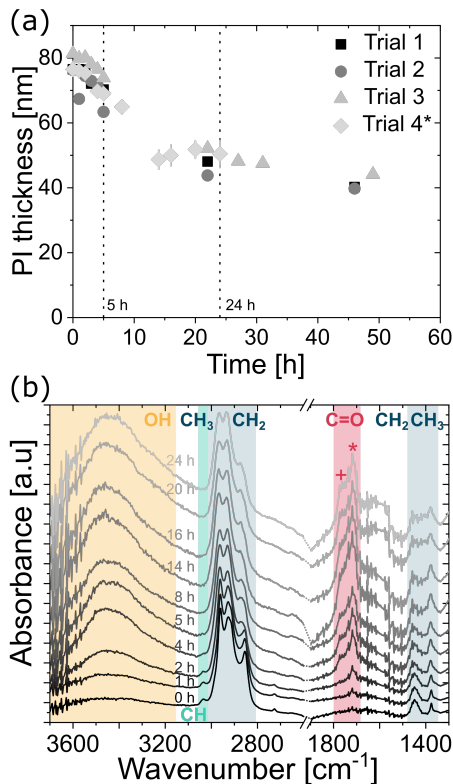


Figure 9.2: (a) Thickness decrease as a function of time during pre-heating of polyisoprene thin films at 80 °C. Trial 1 to 3 constitute thickness data for the same films, respectively, whereas for trial 4 each datapoint constitutes the mean value of 2 individual samples. (b) ATR-FTIR absorbance spectra of spin coated polyisoprene films on glass. Films were pre-heated at 80 °C for different durations (indicated by time in hours). Colored regions refer to O-H stretching (3400 cm^{-1}), =C-H stretching (3036 cm^{-1}), CH₃ and CH₂ stretching ($2800\text{-}2900 \text{ cm}^{-1}$), C=O stretching (+ and * referring to carboxylic acids (1766 cm^{-1}) and ketones (1714 cm^{-1}), respectively), and CH₂ and CH₃ deformation ($1370 - 1450 \text{ cm}^{-1}$). Spectra are scaled to their respective maximum value, offset, and cut to the regions where the main absorptions occur (strong absorption of glass substrate below 1300 cm^{-1}). Dotted lines at the axis break serve as a guide for the eye.

oxide loading depending upon pre-heating conditions for VPI at 80 °C and DEZ hold times of 7200 s (5 individual samples per pre-heating condition). Most of the polyisoprene films pre-heated for 0 h and 5 h show a decrease in thickness (-1.6 % and -4.3 % on average, respectively) upon infiltration while most films pre-heated for 24 h show an increase in thickness (+5.6 % on average). Presuming that volume change is indicative of inorganic loading, these differences in film thickness upon infiltration suggest that the films pre-heated for 0 h or 5 h have less inorganic loading than the films heated for 24 h. However, after calcining these films to leave just the inorganic ZnO component, we find the opposite trend. Figure 9.3 (b) plots this result, showing the ZnO layer thickness after calcination for each of the trials in Figure 9.3(a). On average the polyisoprene films pre-heated for only 5 h have about twice the

ZnO thickness (8 nm) as those pre-heated for 0 h or 24 h (4 nm). While the swelling of polymer films is often used as an indicator for inorganic loading in VPI literature,^{42,7,44} it is not a direct measure of the mass loading, and as shown here, film swelling is not always a good indicator of inorganic loading. The noncorrelation of the swelling and the ZnO thickness after calcination is attributed to a competition between the relaxations / shrinking occurring within the film due to a reduction of the polymer's free volume (thickness decrease) with the swelling due to inorganic mass uptake (thickness increase).

These results suggest that spectroscopic ellipsometry is not always a reliable non-destructive characterization tool for assessing inorganic loading in VPI synthesized hybrid materials. Thus, we also explored the use of XRF as an alternative method for inorganic loading quantification. XRF has not previously had wide use in the VPI community.⁴² XRF is a non-destructive and fast (measurement times < 1 min) characterization technique, that can readily be used to provide relative quantities of inorganics within a hybrid material. (Note: absolute amounts can be measured by calibrating the XRF detector to standards; within the scope of this paper, relative amounts are sufficient, although good standards for infiltrated materials should be developed.) Figure 9.3(c) plots the correlation of the measured XRF Zn K α peak height (of the hybrid film) against the calcined ZnO film thickness determined by spectroscopic ellipsometry in Figure 9.3(b). Good correlation is found between these two methods, validating XRF's use for non-destructive quantification of Zn loading in VPI hybrid thin films.

9.5.4 KINETICS OF ZINC OXIDE INFILTRATION INTO CIS-POLYISOPRENE

Next, we examine the kinetics of inorganic loading as a function of VPI process temperature (60 °C, 80 °C, and 100 °C). Figure 9.4 plots the amount of zinc uptake (measured by XRF) into cis-polyisoprene during a 1-cycle VPI process for varying 0.2 Torr DEZ exposure times (20 sec to 4 hrs). These Zn uptake plots are shown for both unheated (Figure 9.4(a)), 5 h pre-heated (Figure 9.4(b)) and 24 h pre-heated (Figure 9.4(c)) cis-polyisoprene films. (Figure 9.11 plots the calcined ZnO film thickness as a consistent comparison).

When the cis-polyisoprene is not pre-heated prior to infiltration (Figure 9.4(a)), the sorption behavior is consistent with standard models. The inorganic loading increases with increasing hold time until it saturates (for 80 °C and 100 °C). Higher temperatures seem to promote faster saturation (i.e., faster diffusion); in fact, at 60 °C, saturation is not realized within the time scales studied (4 h). The saturation loading (i.e. maximum solubility) decreases with increasing process temperature. These observations are consistent with the kinetic model for VPI presented by Leng and Losego.⁴⁴ From a derivation of Fick's 2nd law,

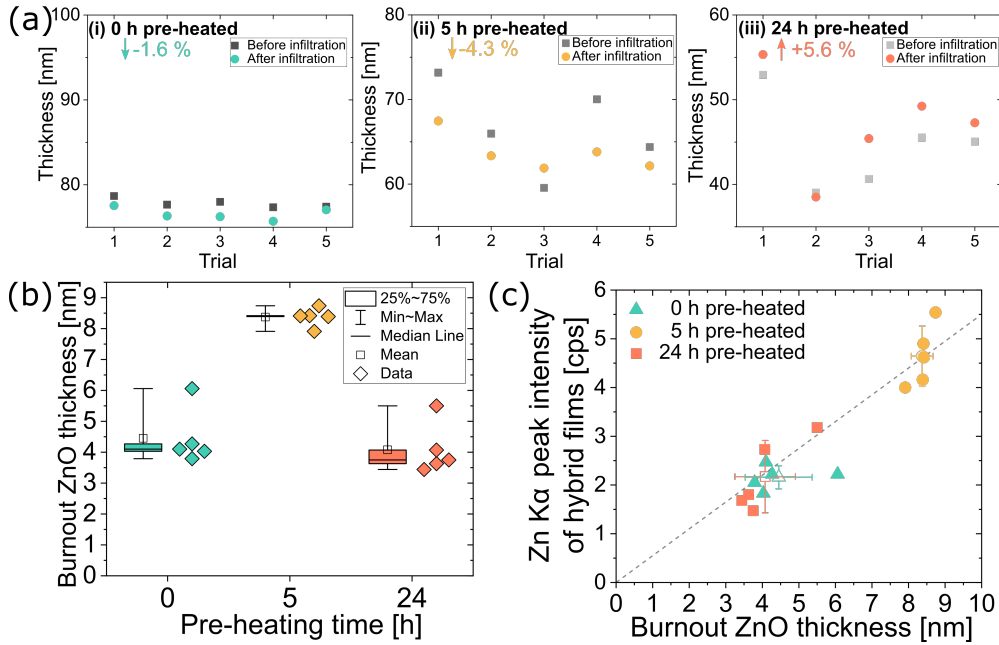


Figure 9.3: (a) Thicknesses of cis-polyisoprene films before and after zinc oxide infiltration for 5 separate but equivalent trials. Films were pre-heated at 80 °C for (i) 0 h, (ii) 5 h, and (iii) 24 h in air prior to infiltration. (Note the changing abscissa in (i) to (iii) for film thickness but same unit spacing). (b) ZnO film thickness after calcination of the infiltrated films at 650 °C for 30 min in air, and (c) correlation of the XRF Zn K α peak height of the hybrid films and the ZnO film thickness after calcination; mean values with their standard deviation of the respective data are indicated with open symbols and the linear slope serves as a guide for the eye. All films were infiltrated at 80 °C using a 7200 s, 0.2 Torr DEZ exposure step.

the normalized mass uptake ($\frac{M_t}{M_\infty}$, where M_∞ is the saturation value) shows a square-root dependence on time (t), with a slope that depends upon the diffusivity (D) and thickness (L) of the polymer matrix

$$\frac{M_t}{M_\infty} = \frac{2}{L} \left(\frac{D}{\pi} \right)^{\frac{1}{2}} \sqrt{t} \quad (9.1)$$

The diffusivity furthermore follows an Arrhenius relationship

$$D = D_0 \exp \left(-\frac{\Delta H_D}{k_B T} \right) \quad (9.2)$$

with D_0 being a temperature independent constant, ΔH_D the activation energy for diffusion, k_B Boltzmann's constant, and T temperature. Using these equations and the data presented in Figure 9.4(a), we estimate the diffusivity to be about 0.5×10^{-14} cm²/s and 3×10^{-14} cm²/s at 80 °C and 100 °C, respectively. These values are within the same order

of magnitude as effective diffusivity values reported for infiltration of trimethylaluminum into poly(methyl methacrylate)⁴⁴ and can give valuable information about infiltration depth when upscaling the process to thicker films or macroscopic objects.^{217,44} Diffusivity values in the order of 10^{-6} cm²/s have been reported for the diffusion of gas molecules such as O₂, N₂, or CO₂ in (vulcanized) natural rubber, i.e. 8 orders of magnitude higher than the current findings; however, it was shown that the diffusivity rapidly decreases with increasing gas molecule size for natural rubber and other polymers.^{231,45} Diffusivity of the much larger DEZ molecule is thus expected to be much lower than for the above mentioned diatomic and triatomic gases. A close examination of the mass uptake curves for the 5 h pre-heated cis-polyisoprene films presented in Figure 9.4(b) suggests that two separate diffusion regimes may exist (indicated by two linear slopes). For short hold times, precursor can diffuse faster whereas the diffusion slows down for longer hold times (estimates of the diffusivity are given in the supporting information). A possible reason for this behavior might be ongoing relaxation of polyisoprene films during infiltration, which comes into effect for longer hold times. Furthermore, from FTIR analysis shown in Figure 9.2(b), films pre-heated for 5 h appear to be in a state in which the oxidation is not yet complete. This might lead to the more complex diffusion kinetic curves as the precursor molecules diffuse through both oxidized and unoxidized regions. For the films pre-heated for 24 h (shown in Figure 9.4(c)), the infiltration kinetics are less differentiable with respect to temperature. While an increase of loading can be observed by increasing the hold time, the relative changes (between measurements for different temperatures) are rather small and difficult to differentiate within measurement error. A reason might be that on average these films are thinner than the films pre-heated for 5 h and thus reach full infiltration faster, limiting the temporal resolution of the diffusion process.⁴⁴ However, it appears that for these films only one diffusion regime exists (indicated by an averaged slope), which agrees with the fact that the films were much longer pre-heated prior to infiltration. Also, the maximum loading is on average smaller than for the films pre-heated for 5 h, which can be attributed to the decreased thickness.

9.5.5 ENTRAPMENT OF DEZ PRECURSOR IN CIS-POLYISOPRENE

Next we explore the entrapment of DEZ precursors within cis-polyisoprene films. Films undergoing 0 h, 5 h, and 24 h pre-heating to 80 °C were all investigated. Infiltration was conducted at 80 °C for 800 s at 2 Torr DEZ. Purge times between the DEZ exposure and water exposure were varied between 100 s and 232200 s (2.5 days). If the DEZ precursor does not strongly bind to the polyisoprene, Zn loading should decrease with increasing purge time.²³²

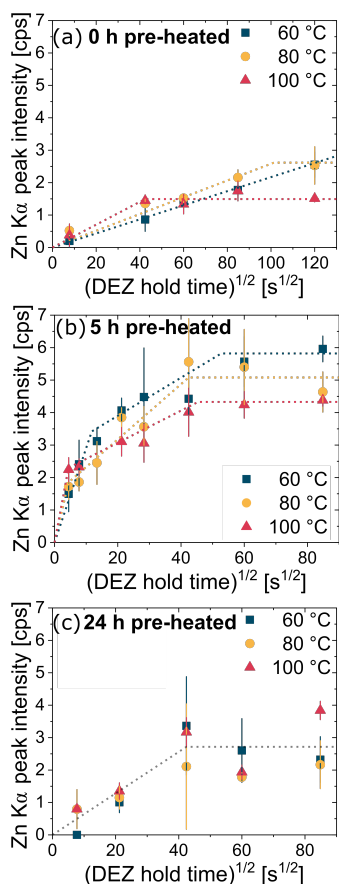


Figure 9.4: XRF measurements of zinc uptake after VPI as a function of DEZ exposure time for various process temperatures using cis-polyisoprene thin films pre-heated at 80 °C in air for (a) 0 h, (b) 5 h, and (c) 24 h. Note the wider ordinate scale for (a). Dotted lines serve as a guide for the eye. Most data points are an average of at least 5 independently processed hybrid films. Error bars represent the standard deviation from measurements on multiple films.

If DEZ forms a permanent or semi-permanent bond to the cis-polyisoprene, then Zn loading should remain nearly invariant with this purge time. As shown in Figure 9.5, the latter situation is true, Zn concentration is relatively invariant with purge time irrespective of pre-heating conditions, even up to a purge time of 2.5 days. This suggests that the precursor DEZ molecules are strongly bound (entrapped) within the polymer and do not easily diffuse out upon removal of the DEZ overpressure.

To further understand the entrapment mechanisms, ATR-FTIR spectroscopy is used to understand the chemical structure of the ZnO-polyisoprene hybrid after infiltration. These ATR-FTIR spectra are shown in Figure 9.6, together with the spectra of the polyisoprene films before infiltration (from Figure 9.2(b)). In comparison to the spectra of pure polymer

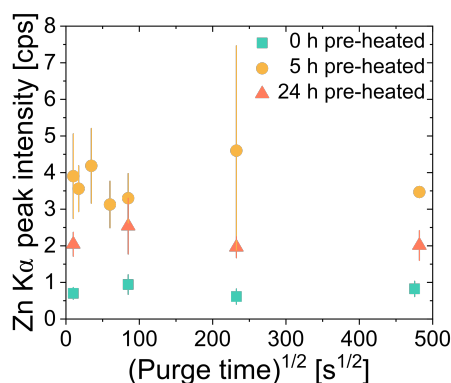


Figure 9.5: XRF measurements of zinc concentration in hybrid films as a function of purge time between DEZ exposure and H₂O exposure. Polyisoprene films are pre-heated at 80 °C for 0 h, 5 h, or 24 h, DEZ hold time is 800 s, and infiltration temperature is 80 °C. Most data points are an average of at least 5 independently processed hybrid films. Error bars represent the standard deviation from measurements on multiple films.

films, several changes can be observed. The contribution of O-H is increased for all films which can be attributed to the water co-reaction in the infiltration process and the likely formation of metal oxyhydroxide inorganic clusters. The reduction in C=O peak intensity with DEZ exposure time indicates a consumption of these groups, likely due to chemical reaction with DEZ. For all the hybrid films, a broad absorption emerges at 1550-1650 cm⁻¹. In VPI literature, this mode has been attributed to metalorganic precursors binding to carbonyl groups, both for DEZ²³³ and trimethylaluminum^{217,234,235}. This suggests that DEZ entrapment is at least partially explained by binding and reaction with these carbonyl groups, which are not inherent to the pure polyisoprene structure but are rather easily created via pre-heating oxidation. However, based on Figure 9.5, the unheated polyisoprene also retains constant Zn loading with purging despite having a negligible concentration of carbonyl or hydroxyl groups. This suggests that DEZ molecules can also become permanently or semi-permanently entrapped within the pure cis-polyisoprene polymer. While this binding may occur to the alkene functional group, its weak absorption in IR spectroscopy makes this difficult to ascertain. Further investigations, including a computational investigation and/or in situ spectroscopy are likely necessary.

Upon further inspection of this entire IR data set (see Figure 9.13), it appears that the relative intensity of remaining C=O groups after infiltration is higher for films pre-heated for a longer duration (see Figure 9.13). One explanation is that these groups are inaccessible for reaction with DEZ. A possible reason is that these more oxidized polymers react with more DEZ molecules in the near surface region, creating a dense hybrid near-surface layer that hin-

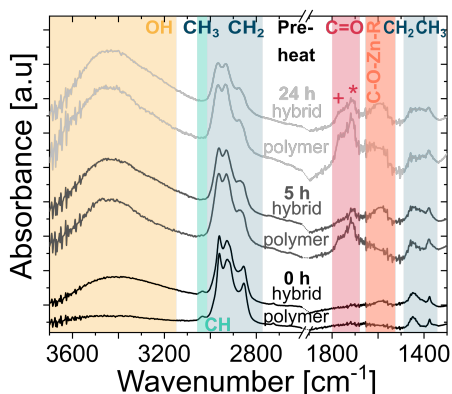


Figure 9.6: ATR-FTIR spectra of polyisoprene films before (same data as in Figure 9.2(b)) and after infiltration, for polyisoprene films pre-heated at 80 °C in air for different durations (indicated above the curves) prior to infiltration. Colored regions refer to O-H stretching (3400 cm^{-1}), =C-H stretching (3036 cm^{-1}), CH₃ and CH₂ stretching (2800-2900 cm^{-1}), C=O stretching (+ and * referring to carboxylic acids (1766 cm^{-1}) and ketones (1714 cm^{-1}), respectively), C-O-Zn-R (1550-1650 cm^{-1}), and CH₂ and CH₃ deformation (1370 - 1450 cm^{-1}). Spectra are scaled to their respective maximum value, offset, and cut to the regions where the main absorptions occur (strong absorption of glass substrate below 1300 cm^{-1}). Dotted lines at the axis break serve as a guide for the eye.

ders further DEZ diffusion. If true, this process should lead to a non-uniform distribution of inorganic throughout the hybrid layer's thickness. To investigate the distribution of Zn within the polymer layer, SIMS was performed on a hybrid film that was preheated for 24 h prior to infiltration. The SIMS depth profile showing Zn⁺, C⁺, and Si⁺ signals is shown in Figure 9.7. The Zn concentration drops precipitously at about 2/3 of the film's thickness, suggesting that for these conditions it is not evenly distributed across the 60 nm hybrid film thickness. Combined with the FTIR data, these results begin to suggest that the greater number of functional groups in the longer pre-heated films lead to a near-surface hybrid layer that significantly inhibits diffusion and full infiltration.

Figure 9.8 plots the Zn loading for polyisoprene films pre-heated for different durations. Analyzing these data allows us to partially deconvolute the effects of polymer relaxation from the creation of reactive functional groups due to polymer oxidation. For this purpose, we divide the curve into three regions. In region I, a strong increase in the amount of inorganic loading is observed with increasing pre-heating time. The increase in loading can be related to the creation of functional groups, and the effect is greater than the loss of free volume due to relaxation. In Region II, Zn loading decreases with pre-heating time. As shown in Figure 9.2(a), Region II also corresponds to a significant decrease in neat polymer film thickness with pre-heating. This decrease in film thickness is attributed to a loss of free volume, which appears to have a greater effect on the loading than the addition of more functional groups,

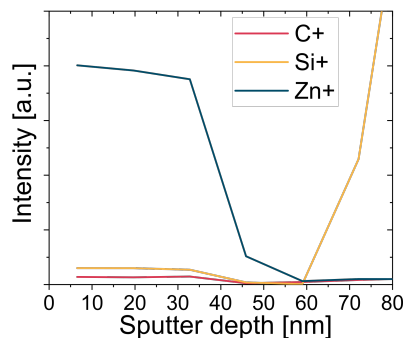


Figure 9.7: SIMS profiles for Zn+, Si+, and C+ as a function of sputter depth for an infiltrated polyisoprene films which was preheated for 24 h at 80 °C prior to infiltration.

leading to a decrease in Zn loading. For the longest pre-heating times (Region III), in which both the polymer relaxation and chemical oxidation reach completion (Figure 9.2), Zn uptake becomes constant irrespective of pre-heating time. Based on FTIR (Figure 9.13) and SIMS (Figure 9.7) data, it is likely that films within Region III are also not fully infiltrated. Instead, these films only have a saturated near-surface layer, likely of similar thickness dictated by the high concentration of reactive functional groups. It is also possible that the decrease in Zn loading in region II could be a combination of lower free volume and reduced infiltration due to the blocking layer. In fact, the fast and then slow diffusion regimes of Figure 9.4(b) may be indicative of these different contributions to the inorganic loading process.

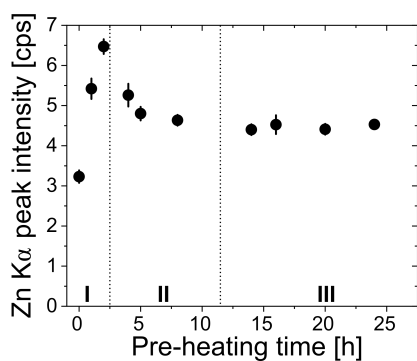


Figure 9.8: XRF measurements of zinc concentration in hybrid films as a function of cis-polyisoprene pre-heating time prior to infiltration. General sample size per data point is $n = 2$. Error bars represent the standard deviation.

Figure 9.9 provides a schematic sketch summarizing our current understanding of the mechanisms controlling DEZ / ZnO entrapment in polyisoprene polymers as a function of

pre-heating time. The infiltration of unheated polyisoprene films results in a small to modest amount of loading. While the DEZ is permanently entrapped, the exact chemical bonding mechanism is not known. Increasing pre-heating times lead to relaxation of the polyisoprene film and increased loading due to creation of functional groups through oxidation. Further increase of pre-heating time leads to further relaxation and dense loading in the top of the film. This dense hybrid layer blocks further sorption and diffusion of the precursor, leaving uninfiltreated regions at the bottom of the film.

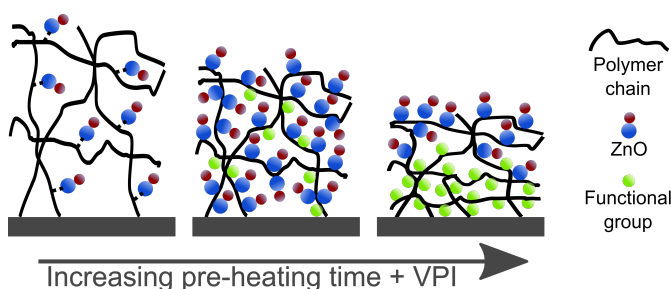


Figure 9.9: Schematic of ZnO loading into polyisoprene as a function of polymer pre-heating time. Pre-heating is believed to affect both the concentration of functional groups reactive to DEZ and the free volume in the polymer.

9.5.6 DISSOLUTION OF ZnO-POLYISOPRENE HYBRID FILMS

Dissolution experiments are performed to better understand the physicochemical structure of the ZnO-polyisoprene hybrid materials. Hybrids are tested against toluene because it is a good solvent for the neat cis-polyisoprene polymer. Figure 9.10 plots the normalized thickness as a function of immersion time for (a) pure polyisoprene polymers pre-heated for 0 h, 5 h and 24 h and (a) infiltrated ZnO-polyisoprene hybrids formed from these various preheated conditions. Polyisoprene polymers (Figure 9.10(a)) rapidly lose thickness upon immersion in toluene. All films show a loss of at least 40 % in thickness within 30 min of immersion. The unheated neat polymer dissolves most rapidly and is completely dissolved within 1 h. Neat polymers that are pre-heated prior to immersion in toluene show increased stability. The 5 h heated film loses around 90 % of thickness within 25 h, but at least 50 % of the 24 h heated film survives for 25 h of immersion. This stability is likely the result of oxidative cross-linking.²²⁵ Infiltration of the films leads to increased stability for all pre-heating conditions. Unheated film and films pre-heated for 5 h do show some dissolution but at a much slower rate than the pure polymer films. Films which are pre-heated for 24 h prior to infiltration swell upon immersion (normalized thickness exceeds 100 %). This result suggests that these

hybrid materials are likely chemically cross-linked. For 5 h pre-heating, this cross-linking is probably incomplete. For unheated films, precursors may not be bound to the polymer at all, and rather act to simply inhibit polymer reptation and simply slow the dissolution rate. The ability to increase chemical stability of polymers in solvents by VPI has been reported for different systems.^{217,49} In a recent study by McGuinness et al.,²¹⁷ the stability of AlO_x -poly(methyl methacrylate) hybrid films was tested in various solvents. The authors found that the infiltration temperature controlled the physicochemical structure of the final hybrid material and its resultant chemical dissolution performance. Low infiltration temperatures led to unbound inorganic in the polymer matrix whereas high temperatures led to chemical bonds between the precursor and the moieties of the polymer as well as cross-linking. Films infiltrated at high temperatures were found to be stable in all investigated solvents whereas films infiltrated at low temperature showed dissolution in some solvents, including dissolution of the inorganic in water. While the effect of infiltration temperature on dissolution behavior was not part of this study, we observe similar trends via the introduction of chemically reactive functional groups through polymer oxidation. Longer pre-heating times lead to the creation of more functional groups in the polymer with which the precursor can chemically react. These chemical reactions lead to more cross-linking that increase chemical stability.

9.6 CONCLUSIONS

This study demonstrates the ability to use single-exposure vapor phase infiltration of DEZ + H_2O on cis-polyisoprene polymers to create ZnO-polyisoprene hybrid materials. Unlike other VPI chemistries, volume changes (i.e., film thickness changes) with infiltration are not well correlated to inorganic mass loading. Volume changes appear to be a convolution of polymer relaxation processes (reduced volume) and mass uptake (volume expansion processes) that are often similar in magnitude. XRF spectroscopy is introduced as an alternative non-destructive method for quantifying the amount of inorganic loading in these hybrid films. Several complicating factors are identified in controlling the infiltration process of polyisoprene rubbers. Both changes in the free volume of the polymer and the potential to oxidize the polymer and form reactive carbonyl and hydroxide groups at modest temperatures (80°C) contribute to the DEZ sorption, diffusion, and entrapment processes. With modest heating and oxidation of the polymer, it is possible to significantly increase the zinc oxide loading by more than 2x. IR spectroscopy confirms reaction with these oxidized functional groups, revealing both a decrease in the carbonyl intensity and the emergence of a C-O-Zn-R functional

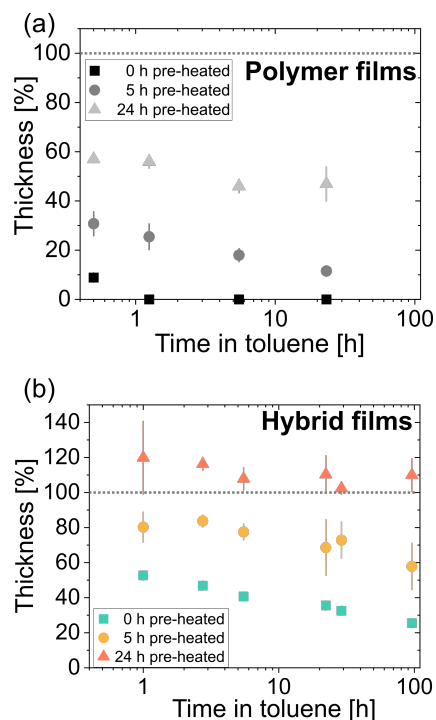


Figure 9.10: Normalized film thickness of (a) pure and (b) infiltrated polyisoprene films as a function of time in toluene. Polyisoprene films were pre-heated for either 0 h, 5 h, or 24 h prior to (a) dissolution or (b) infiltration and dissolution. Dotted lines indicate normalized film thickness (100 %) prior to immersion in toluene. Sample size per data point $n=2$. Error bars represent the standard deviation from measurements on multiple films.

group. However, continued heating of the polymer decreases Zn loading. This decrease is attributed to either a decrease in the polymer's free volume or a highly cross-linked near surface layer that prevents further sorption and diffusion, the latter appearing to be more likely. Interestingly, even without these oxide functional groups, the DEZ appears to form a stable adduct within the polymer that is highly resistant to desorption, even without dosing the water co-reactant. However, the resulting hybrid films show significantly different dissolution behavior in toluene, a good solvent for the pure polymer. Infiltrated polyisoprene with negligible functional groups dissolve, albeit slowly, while infiltrated polyisoprene with many reactive functional groups show much more limited dissolution or even swelling as would be expected for a cross-linked gel. These observations suggest distinct differences in the chemical bonding structure of these organic-inorganic hybrid materials. Further computational studies or in situ process characterization will be necessary to fully understand this behavior, however, significant opportunity exists in exploring these infiltrated hybrid materials as new

accelerators for rubber vulcanization or modifiers to alter the physical properties of polyisoprene rubbers.

9.7 ACKNOWLEDGEMENTS

This project has received partial funding from the European Research Council (ERC) under the European Union's Horizon 2020 research and innovation program (Grant Agreement No. 715403). This material is also based upon work partially supported by the National Science Foundation under Grant # 1921873. J. P. acknowledges personal funding from the Austrian Marshall Plan Foundation for funding his research stay at Georgia Tech. The authors acknowledge Yi Li for performing XPS measurements and Jamie P. Wooding for performing SIMS measurements. Any opinions, findings, and conclusions or recommendations expressed in this material are those of the authors and do not necessarily reflect the views of these funding agencies.

9.8 SUPPORTING INFORMATION

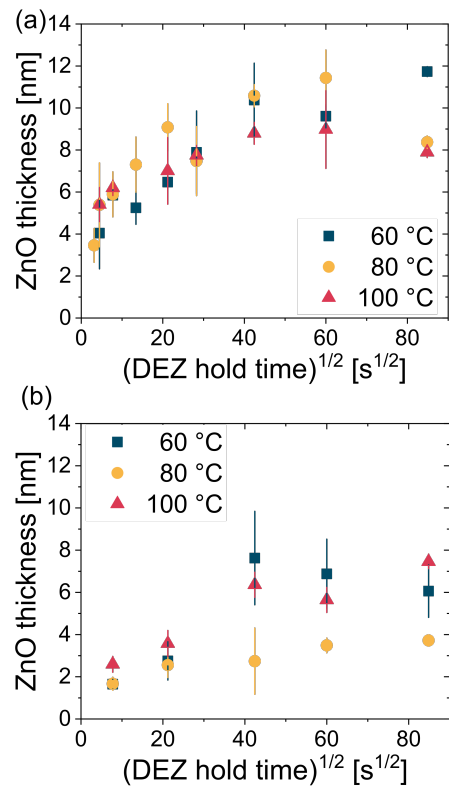


Figure 9.11: Thickness of the resulting ZnO layer after calcination of infiltrated polyisoprene films at 650 °C as a function of DEZ hold time. (a) Films pre-heated for 5 h, and (b) films pre-heated for 24 h prior to infiltration.

9.8.1 DIFFUSION KINETICS

- Normalized slope $k = \frac{M_t}{M_\infty t}$
- Diffusivity $D = \left(\frac{kL}{2}\right)^2 \pi$

○ H ANNEALED

Assumption: $L = 80$ nm

| Infiltration temperature / °C | k | $D / 10^{-14} \text{ cm}^2/\text{s}$ |
|-------------------------------|-------------------|--------------------------------------|
| 60 | Not yet saturated | |
| 80 | 0.01 | 0.5 |
| 100 | 0.025 | 3 |

5 H ANNEALED

Assumption: $L = 70 \text{ nm}$, two diffusion regimes

| Infiltration temperature / °C | k_1 | $D_1 / 10^{-14} \text{ cm}^2/\text{s}$ | k_2 | $D_2 / 10^{-14} \text{ cm}^2/\text{s}$ |
|-------------------------------|-------|--|-------|--|
| 60 | 0.06 | 14 | 0.012 | 0.55 |
| 80 | 0.07 | 19 | 0.018 | 1.25 |
| 100 | 0.12 | 55 | 0.011 | 0.5 |

24 H ANNEALED

Assumption: $L = 50 \text{ nm}$

| Infiltration temperature / °C | k | $D / 10^{-14} \text{ cm}^2/\text{s}$ |
|-------------------------------|-------|--------------------------------------|
| All temperatures | 0.025 | 1.1 |

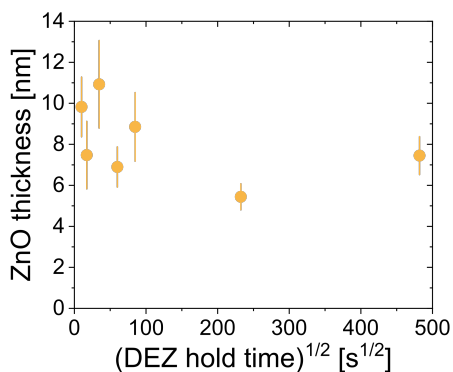


Figure 9.12: Thickness of the resulting ZnO layer after calcination of infiltrated polyisoprene films at 650 °C as a function of purge after DEZ exposure. Films were pre-heated for 5 h prior to infiltration.

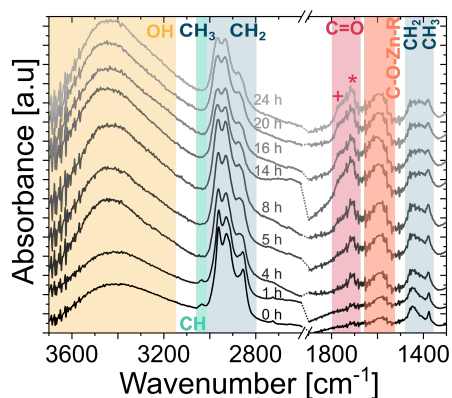


Figure 9.13: ATR-FTIR spectra of polyisoprene films after infiltration, for polyisoprene films pre-heated at 80 °C in air for different durations (indicated the curves) prior to infiltration. Colored regions refer to O-H stretching (3400 cm^{-1}), =C-H stretching (3036 cm^{-1}), CH_3 and CH_2 stretching ($2800\text{-}2900\text{ cm}^{-1}$), C=O stretching (+ and * referring to carboxylic acids (1766 cm^{-1}) and ketones (1714 cm^{-1}), respectively), C-O-Zn-R ($1550\text{-}1650\text{ cm}^{-1}$), and CH_2 and CH_3 deformation ($1370\text{ - }1450\text{ cm}^{-1}$). Spectra are scaled to their respective maximum value, offset, and cut to the regions where the main absorptions occur (strong absorption of glass substrate below 1300 cm^{-1}). Dotted lines at the axis break serve as a guide for the eye.

10

Conclusions and Outlook

In this thesis, the deposition of ZnO by plasma-enhanced atomic layer deposition (PE-ALD) and vapor phase infiltration (VPI) has been investigated.

PE-ALD of ZnO thin films at room-temperature showed self-limiting behavior and resulted in high-quality films with only small amount of impurities. This low-temperature process could be interesting for the application on thermo-sensitive substrate such as synthetic polymers or biological materials. By investigating the influence of the substrate temperature, the growth characteristics and the resulting material properties were found closely related and temperature regions for different applications could be identified. For example, in the temperature region in which the growth per cycle was found constant, ZnO exhibited a strong preferential crystalline orientation, high density, high resistivity, and excitonic absorption, which could be attractive for optical applications such as lasers. By studying the first few cycles of PE-ALD, the initial growth could be identified as substrate-enhanced island growth. After formation of a continuous layer by island coalescence, the growth transitioned to the ideal layer-by-layer growth and crystallites started to grow. The crystallite formation was hereby investigated by high-intensity synchrotron radiation. Knowledge about the initial stages of growth are essential for e.g. the application of ultrathin passivation layers, which need to be dense and continuous (i.e. pin-hole free). In the last study on PE-ALD ZnO, the piezoelectric properties of the films were investigated. A macroscopic evaluation of the film sandwiched between two electrodes revealed that films on a flexible substrate show a higher piezoresponse than films on a rigid substrate, possibly due to bending effects. Fur-

thermore, films grown at higher substrate temperature showed higher piezoresponse due to an enhanced crystalline orientation. The trend was furthermore confirmed by microscopic scanning probe techniques. The study showed the successful deposition of piezoelectric films which could be used in sensors or nanogenerators. By utilizing the conformal features of ALD, these films could be applied on 3D-substrates with potential applications in micro- and nanoelectromechanical systems.

The growth of ZnO was furthermore investigated by vapor phase infiltration. In the presented study, cis-polyisoprene was successfully infiltrated and the infiltration kinetics monitored. Pre-heating of the polymer resulted in shrinking and oxidation of the polymer and had large effects on the infiltration characteristics. As an example of the properties of the hybrid material, dissolution studies were performed, which showed enhanced stability for the hybrid material compared to the pure polymer. While this study presented the basics of infiltration, further properties (mechanical, optical, ...) were likely changed upon infiltration which could demonstrate the ability of infiltrated ZnO to serve as a UV-protection or vulcanization accelerator in the rubber.

Contributions

ARTICLES

1. Pilz, J.; Perrotta, A.; Christian, P.; Tazreiter, M.; Resel, R.; Leising, G.; Griesser, T.; Coclite, A. M. Tuning of Material Properties of ZnO Thin Films Grown by Plasma-Enhanced Atomic Layer Deposition at Room Temperature. *J. Vac. Sci. Technol. A* **2018**, *36* (1), 01A109. <https://doi.org/10.1116/1.5003334>
2. Perrotta, A.; Pilz, J.; Milella, A.; Coclite, A. M. Opto-Chemical Control through Thermal Treatment of Plasma Enhanced Atomic Layer Deposited ZnO: An in Situ Study. *Appl. Surf. Sci.* **2019**, *483*, 10–18. <https://doi.org/10.1016/j.apsusc.2019.03.122>
3. Perrotta, A.; Pilz, J.; Pachmajer, S.; Milella, A.; Coclite, A. M. On the Transformation of “Zincone”-like into Porous ZnO Thin Films from Sub-Saturated Plasma Enhanced Atomic Layer Deposition. *Beilstein J. Nanotechnol.* **2019**, *10* (1), 746–759. <https://doi.org/10.3762/bjnano.10.74>
4. Pilz, J.; Perrotta, A.; Leising, G.; Coclite, A. M. ZnO Thin Films Grown by Plasma-Enhanced Atomic Layer Deposition: Material Properties Within and Outside the “Atomic Layer Deposition Window.” *Phys. status solidi* **2019**, 1900256. <https://doi.org/10.1002/pssa.201900256>
5. Pilz, J.; Tazreiter, M.; Coclite, A. M. Universal Software for the Real-Time Control of Sequential Processing Techniques. *J. Vac. Sci. Technol. A* **2019**, *37* (6), 063201. <https://doi.org/10.1116/1.5125052>
6. Perrotta, A.; Pilz, J.; Resel, R.; Werzer, O.; Coclite, A. M. Initial Growth and Crystallization Onset of Plasma Enhanced-Atomic Layer Deposited ZnO. *Crystals* **2020**, *10* (4), 291. <https://doi.org/10.3390/cryst10040291>
7. Pilz, J.; Coclite, A. M.; Losego M. D. Vapor Phase Infiltration of ZnO into Thin Films of Cis-Polyisoprene (Natural Rubber). *Under Review*
8. Abu Ali, T; Pilz, J.; Schöffner, P.; Kratzer, M.; Teichert, C.; Stadlober, B.; Coclite, A. M. Piezoelectric properties of zinc oxide thin films grown by plasma-enhanced atomic layer deposition. *Under Review*

POSTER PRESENTATIONS

1. Tuning of material properties of ZnO thin films grown by plasma-enhanced atomic layer deposition at room temperature. *Advanced Materials Day*, Graz, Austria, Sep 2017.
2. Tuning Material Properties of ZnO Thin Films for Advanced Sensor Applications. *Euroensors Conference*, Graz, Austria, Sep 2018.
3. Tuning Material Properties of ZnO Thin Films for Advanced Sensor Applications. *Advanced Materials Day*, Graz, Austria, Sep 2018.

ORAL PRESENTATIONS

1. Temperature Effect on ZnO by Plasma-Enhanced Atomic Layer Deposition. *IMPRESS Symposium*, Graz, Austria, Jul 2018.
2. Influence of Substrate Temperature on Structural, Optical, and Electrical Properties of ZnO Deposited by Plasma-Enhanced Atomic Layer Deposition. *68th Annual Meeting of the Austrian Physical Society*, Graz, Austria, Sep 2018.
3. Temperature Effect on ZnO by Plasma-Enhanced Atomic Layer Deposition. *AVS 65th International Symposium*, Long Beach, CA, USA, Oct 2018.
4. Study of the properties of Al:ZnO thin films grown by plasma-enhanced atomic layer deposition. *24th International Symposium on Plasma Chemistry*, Naples, Italy, Jun 2019.
5. ZnO thin films grown by plasma-enhanced atomic layer deposition: material properties in and outside the ALD window. *EuroCVD 22 Baltic ALD 16 Conference*, Luxembourg, Luxembourg, Jun 2019.
6. Piezoelectric Response of ZnO Thin Films Grown By Plasma-Enhanced Atomic Layer Deposition. *236th ECS Meeting*, Atlanta, GA, USA, Oct 2019.
7. Piezoelectric Response of ZnO Thin Films Grown By Plasma-Enhanced Atomic Layer Deposition. *AVS 66th International Symposium*, Columbus, OH, USA, Oct 2019.

References

- [1] Moezzi, A.; McDonagh, A. M.; Cortie, M. B. Zinc oxide particles: Synthesis, properties and applications. *Chemical Engineering Journal* **2012**, *185-186*, 1–22.
- [2] Klingshirn, C. F.; Meyer, B. K.; Waag, A.; Hoffmann, A.; Geurts, J. *Zinc Oxide: From Fundamental Properties Towards Novel Applications*; Springer Series in Materials Science; Springer Berlin Heidelberg: Berlin, Heidelberg, 2010.
- [3] Wang, Z. L. Towards Self-Powered Nanosystems: From Nanogenerators to Nanopiezotronics. *Advanced Functional Materials* **2008**, *18*, 3553–3567.
- [4] George, S. M. Atomic Layer Deposition: An Overview. *Chemical Reviews* **2010**, *110*, 111–131.
- [5] Johnson, R. W.; Hultqvist, A.; Bent, S. F. A brief review of atomic layer deposition: from fundamentals to applications. *Materials Today* **2014**, *17*, 236–246.
- [6] Profijt, H. B.; Potts, S. E.; de Sanden, M. C. M.; Kessels, W. M. M. Plasma-assisted atomic layer deposition: basics, opportunities, and challenges. *Journal of Vacuum Science & Technology A: Vacuum, Surfaces, and Films* **2011**, *29*, 50801.
- [7] Leng, C. Z.; Losego, M. D. Vapor phase infiltration (VPI) for transforming polymers into organic–inorganic hybrid materials: a critical review of current progress and future challenges. *Materials Horizons* **2017**, *4*, 747–771.
- [8] Smith, D. L. *Thin-Film Deposition: Principles and Practice*; McGraw-Hill: New York City, 1995.
- [9] Ohring, M. *Materials Science of Thin Films*; Academic Press: San Diego, 2002.
- [10] Coclite, A. M.; Howden, R. M.; Borrelli, D. C.; Petruczok, C. D.; Yang, R.; Yagüe, J. L.; Ugur, A.; Chen, N.; Lee, S.; Jo, W. J.; Liu, A.; Wang, X.; Gleason, K. K. 25th Anniversary Article: CVD Polymers: A New Paradigm for Surface Modification and Device Fabrication. *Advanced Materials* **2013**, *25*, 5392–5423.
- [11] Parsons, G. N.; Elam, J. W.; George, S. M.; Haukka, S.; Jeon, H.; (Erwin) Kessels, W. M. M.; Leskelä, M.; Poedt, P.; Ritala, M.; Rosnagel, S. M. History of atomic layer deposition and its relationship with the American Vacuum Society. *Journal of Vacuum Science & Technology A: Vacuum, Surfaces, and Films* **2013**, *31*, 050818.

- [12] King, D. M.; Liang, X.; Carney, C. S.; Hakim, L. F.; Li, P.; Weimer, A. W. Atomic Layer Deposition of UV-Absorbing ZnO Films on SiO₂ and TiO₂ Nanoparticles Using a Fluidized Bed Reactor. *Advanced Functional Materials* **2008**, *18*, 607–615.
- [13] Puurunen, R. L. Surface chemistry of atomic layer deposition: A case study for the trimethylaluminum/water process. *Journal of Applied Physics* **2005**, *97*, 121301.
- [14] Puurunen, R. L.; Vandervorst, W. Island growth as a growth mode in atomic layer deposition: A phenomenological model. *Journal of Applied Physics* **2004**, *96*, 7686–7695.
- [15] Richey, N. E.; de Paula, C.; Bent, S. F. Understanding chemical and physical mechanisms in atomic layer deposition. *The Journal of Chemical Physics* **2020**, *152*, 040902.
- [16] Weckman, T.; Laasonen, K. Atomic Layer Deposition of Zinc Oxide: Diethyl Zinc Reactions and Surface Saturation from First-Principles. *The Journal of Physical Chemistry C* **2016**, *120*, 21460–21471.
- [17] Bartram, M. E.; Michalske, T. A.; Rogers, J. W. A reexamination of the chemisorption of trimethylaluminum on silica. *The Journal of Physical Chemistry* **1991**, *95*, 4453–4463.
- [18] Grillo, F.; Moulijn, J. A.; Kreutzer, M. T.; van Ommen, J. R. Nanoparticle sintering in atomic layer deposition of supported catalysts: Kinetic modeling of the size distribution. *Catalysis Today* **2018**, *316*, 51–61.
- [19] Nič, M., Jiráť, J., Košata, B., Jenkins, A., McNaught, A., Eds. *IUPAC Compendium of Chemical Terminology*; IUPAC: Research Triangle Park, NC, 2009.
- [20] Heil, S. B. S.; van Hemmen, J. L.; van de Sanden, M. C. M.; Kessels, W. M. M. Reaction mechanisms during plasma-assisted atomic layer deposition of metal oxides: A case study for Al₂O₃. *Journal of Applied Physics* **2008**, *103*, 103302.
- [21] Dendooven, J.; Deduytsche, D.; Musschoot, J.; Vanmeirhaeghe, R. L.; Detavernier, C. Conformality of Al₂O₃ and AlN Deposited by Plasma-Enhanced Atomic Layer Deposition. *Journal of The Electrochemical Society* **2010**, *157*, G111.
- [22] Profijt, H. B.; Kudlacek, P.; van de Sanden, M. C. M.; Kessels, W. M. M. Ion and Photon Surface Interaction during Remote Plasma ALD of Metal Oxides. *Journal of The Electrochemical Society* **2011**, *158*, G88.
- [23] Knoops, H. C. M.; Faraz, T.; Arts, K.; Kessels, W. M. M. E. Status and prospects of plasma-assisted atomic layer deposition. *Journal of Vacuum Science & Technology A* **2019**, *37*, 030902.

- [24] Faraz, T.; Arts, K.; Karwal, S.; Knoops, H. C. M.; Kessels, W. M. M. Energetic ions during plasma-enhanced atomic layer deposition and their role in tailoring material properties. *Plasma Sources Science and Technology* **2019**, *28*, 024002.
- [25] Musschoot, J. Advantages and challenges of plasma enhanced atomic layer deposition. Ph.D. thesis, Universiteit Gent, 2011.
- [26] Emslie, D. J.; Chadha, P.; Price, J. S. Metal ALD and pulsed CVD: Fundamental reactions and links with solution chemistry. *Coordination Chemistry Reviews* **2013**, *257*, 3282–3296.
- [27] Miikkulainen, V.; Leskelä, M.; Ritala, M.; Puurunen, R. L. Crystallinity of inorganic films grown by atomic layer deposition: Overview and general trends. *Journal of Applied Physics* **2013**, *113*, 021301.
- [28] Mackus, A. J. M.; Schneider, J. R.; MacIsaac, C.; Baker, J. G.; Bent, S. F. Synthesis of Doped, Ternary, and Quaternary Materials by Atomic Layer Deposition: A Review. *Chemistry of Materials* **2019**, *31*, 1142–1183.
- [29] ALD database. <https://www.atomiclimits.com/alddbatabase/>.
- [30] Cremers, V.; Puurunen, R. L.; Dendooven, J. Conformality in atomic layer deposition: Current status overview of analysis and modelling. *Applied Physics Reviews* **2019**, *6*, 021302.
- [31] Rossnagel, S. M. Thin film deposition with physical vapor deposition and related technologies. *Journal of Vacuum Science & Technology A: Vacuum, Surfaces, and Films* **2003**, *21*, S74–S87.
- [32] Knoops, H.; Potts, S.; Bol, A.; Kessels, W. *Handbook of Crystal Growth*, second ed ed.; Elsevier, 2015; Vol. 3; pp 1101–1134.
- [33] Lundstrom, M. Moore's law forever? *Science* **2003**, *299*, 210–211.
- [34] Mistry, K. et al. A 45nm Logic Technology with High-k+Metal Gate Transistors, Strained Silicon, 9 Cu Interconnect Layers, 193nm Dry Patterning, and 100% Pb-free Packaging. 2007 IEEE International Electron Devices Meeting. 2007; pp 247–250.
- [35] Auth, C. et al. A 22nm high performance and low-power CMOS technology featuring fully-depleted tri-gate transistors, self-aligned contacts and high density MIM capacitors. 2012 Symposium on VLSI Technology (VLSIT). 2012; pp 131–132.
- [36] Lu, W.; Lee, Y.; Gertsch, J. C.; Murdzek, J. A.; Cavanagh, A. S.; Kong, L.; del Alamo, J. A.; George, S. M. In Situ Thermal Atomic Layer Etching for Sub-5 nm InGaAs Multigate MOSFETs. *Nano Letters* **2019**, *19*, 5159–5166.

- [37] Asundi, A. S.; Raiford, J. A.; Bent, S. F. Opportunities for Atomic Layer Deposition in Emerging Energy Technologies. *ACS Energy Letters* **2019**, *4*, 908–925.
- [38] Sundberg, P.; Karppinen, M. Organic and inorganic–organic thin film structures by molecular layer deposition: A review. *Beilstein Journal of Nanotechnology* **2014**, *5*, 1104–1136.
- [39] Weimer, A. W. Particle atomic layer deposition. *Journal of Nanoparticle Research* **2019**, *21*, 9.
- [40] Fan, H. J.; Nielsch, K. In *Atomic Layer Deposition of Nanostructured Materials*; Pinna, N., Knez, M., Eds.; Wiley-VCH: Weinheim, 2012; Chapter 11, pp 251–270.
- [41] King, D. M.; Spencer, J. A.; Liang, X.; Hakim, L. F.; Weimer, A. W. Atomic layer deposition on particles using a fluidized bed reactor with in situ mass spectrometry. *Surface and Coatings Technology* **2007**, *201*, 9163–9171.
- [42] Waldman, R. Z.; Mandia, D. J.; Yanguas-Gil, A.; Martinson, A. B. F.; Elam, J. W.; Darling, S. B. The chemical physics of sequential infiltration synthesis—A thermodynamic and kinetic perspective. *The Journal of Chemical Physics* **2019**, *151*, 190901.
- [43] Wilson, C. A.; Grubbs, R. K.; George, S. M. Nucleation and Growth during Al₂O₃ Atomic Layer Deposition on Polymers. *Chemistry of Materials* **2005**, *17*, 5625–5634.
- [44] Leng, C. Z.; Losego, M. D. A physiochemical processing kinetics model for the vapor phase infiltration of polymers: measuring the energetics of precursor-polymer sorption, diffusion, and reaction. *Physical Chemistry Chemical Physics* **2018**, *20*, 21506–21514.
- [45] Berens, A.; Hopfenberg, H. Diffusion of organic vapors at low concentrations in glassy PVC, polystyrene, and PMMA. *Journal of Membrane Science* **1982**, *10*, 283–303.
- [46] Subramanian, A.; Tiwale, N.; Nam, C.-Y. Review of Recent Advances in Applications of Vapor-Phase Material Infiltration Based on Atomic Layer Deposition. *JOM* **2019**, *71*, 185–196.
- [47] Gregorczyk, K.; Knez, M. Hybrid nanomaterials through molecular and atomic layer deposition: Top down, bottom up, and in-between approaches to new materials. *Progress in Materials Science* **2016**, *75*, 1–37.
- [48] Lee, S.-M.; Pippel, E.; Gosele, U.; Dresbach, C.; Qin, Y.; Chandran, C. V.; Braunerger, T.; Hause, G.; Knez, M. Greatly Increased Toughness of Infiltrated Spider Silk. *Science* **2009**, *324*, 488–492.

- [49] McGuinness, E. K.; Zhang, F.; Ma, Y.; Lively, R. P.; Losego, M. D. Vapor Phase Infiltration of Metal Oxides into Nanoporous Polymers for Organic Solvent Separation Membranes. *Chemistry of Materials* **2019**, *31*, 5509–5518.
- [50] Bang, J.; Jeong, U.; Ryu, D. Y.; Russell, T. P.; Hawker, C. J. Block Copolymer Nanolithography: Translation of Molecular Level Control to Nanoscale Patterns. *Advanced Materials* **2009**, *21*, 4769–4792.
- [51] Peng, Q.; Tseng, Y.-C.; Darling, S. B.; Elam, J. W. Nanoscopic Patterned Materials with Tunable Dimensions via Atomic Layer Deposition on Block Copolymers. *Advanced Materials* **2010**, *22*, 5129–5133.
- [52] Peng, Q.; Tseng, Y.-C.; Darling, S. B.; Elam, J. W. A Route to Nanoscopic Materials via Sequential Infiltration Synthesis on Block Copolymer Templates. *ACS Nano* **2011**, *5*, 4600–4606.
- [53] Morkoç, H.; Özgür, Ü. *Zinc Oxide: Fundamentals, Materials and Device Technology*; Wiley-VCH Verlag: Weinheim, 2009.
- [54] Jagadish, C., Pearton, S., Eds. *Zinc Oxide Bulk, Thin Films and Nanostructures*; Elsevier, 2006.
- [55] Zhu, L.; Zeng, W. Room-temperature gas sensing of ZnO-based gas sensor: A review. *Sensors and Actuators A: Physical* **2017**, *267*, 242–261.
- [56] Özgür, Ü.; Alivov, Y. I.; Liu, C.; Teke, A.; Reshchikov, M. A.; Doğan, S.; Avrutin, V.; Cho, S.-J.; Morkoç, H. A comprehensive review of ZnO materials and devices. *Journal of Applied Physics* **2005**, *98*, 041301.
- [57] Wang, Z. L. Piezoelectric Nanogenerators Based on Zinc Oxide Nanowire Arrays. *Science* **2006**, *312*, 242–246.
- [58] Briscoe, J.; Dunn, S. Piezoelectric nanogenerators – a review of nanostructured piezoelectric energy harvesters. *Nano Energy* **2015**, *14*, 15–29.
- [59] Piercy, B. D.; Losego, M. D. Tree-based control software for multilevel sequencing in thin film deposition applications. *Journal of Vacuum Science & Technology B, Nanotechnology and Microelectronics: Materials, Processing, Measurement, and Phenomena* **2015**, *33*, 043201.
- [60] Cho, A.; Arthur, J. Molecular beam epitaxy. *Progress in Solid State Chemistry* **1975**, *10*, 157–191.
- [61] Oehrlein, G. S.; Metzler, D.; Li, C. Atomic Layer Etching at the Tipping Point: An Overview. *ECS Journal of Solid State Science and Technology* **2015**, *4*, N5041–N5053.

- [62] Gregorczyk, K.; Knez, M. Hybrid nanomaterials through molecular and atomic layer deposition: Top down, bottom up, and in-between approaches to new materials. *Progress in Materials Science* **2016**, *75*, 1–37.
- [63] Selvaraj, S. K.; Takoudis, C. G. Scalable control program for multiprecursor flow-type atomic layer deposition system. *Journal of Vacuum Science & Technology A: Vacuum, Surfaces, and Films* **2015**, *33*, 013201.
- [64] Langereis, E.; Heil, S. B. S.; Knoops, H. C. M.; Keuning, W.; van de Sanden, M. C. M.; Kessels, W. M. M. In situ spectroscopic ellipsometry as a versatile tool for studying atomic layer deposition. *Journal of Physics D: Applied Physics* **2009**, *42*, 073001.
- [65] Perrotta, A.; Pilz, J.; Milella, A.; Coclite, A. M. Opto-chemical control through thermal treatment of plasma enhanced atomic layer deposited ZnO: An in situ study. *Applied Surface Science* **2019**, *483*, 10–18.
- [66] Perrotta, A.; Pilz, J.; Pachmajer, S.; Milella, A.; Coclite, A. M. On the transformation of “zincone”-like into porous ZnO thin films from sub-saturated plasma enhanced atomic layer deposition. *Beilstein Journal of Nanotechnology* **2019**, *10*, 746–759.
- [67] Pilz, J.; Perrotta, A.; Leising, G.; Coclite, A. M. ZnO Thin Films Grown by Plasma-Enhanced Atomic Layer Deposition: Material Properties Within and Outside the “Atomic Layer Deposition Window”. *physica status solidi (a)* **2019**, 1900256.
- [68] Perrotta, A.; Berger, R.; Muralter, F.; Coclite, A. M. Mesoporous ZnO thin films obtained from molecular layer deposited “zincones”. *Dalton Transactions* **2019**, *48*, 14178–14188.
- [69] Groner, M. D.; Fabreguette, F. H.; Elam, J. W.; George, S. M. Low-Temperature Al₂O₃ Atomic Layer Deposition. *Chemistry of Materials* **2004**, *16*, 639–645.
- [70] Banerjee, P.; Lee, W.-J.; Bae, K.-R.; Lee, S. B.; Rubloff, G. W. Structural, electrical, and optical properties of atomic layer deposition Al-doped ZnO films. *Journal of Applied Physics* **2010**, *108*, 043504.
- [71] Szeghalmi, A.; Senz, S.; Bretschneider, M.; Gösele, U.; Knez, M. All dielectric hard x-ray mirror by atomic layer deposition. *Applied Physics Letters* **2009**, *94*, 133111.
- [72] Holme, T. P.; Lee, C.; Prinz, F. B. Atomic layer deposition of LSM cathodes for solid oxide fuel cells. *Solid State Ionics* **2008**, *179*, 1540–1544.
- [73] Fujiwara, H. *Spectroscopic Ellipsometry: Principles and Applications*; John Wiley & Sons: New York City, 2007.
- [74] Birkholz, M. *Thin Film Analysis by X-Ray Scattering*; Wiley-VCH: Weinheim, 2006.

- [75] Lausi, A.; Polentarutti, M.; Onesti, S.; Plaisier, J. R.; Busetto, E.; Bais, G.; Barba, L.; Cassetta, A.; Campi, G.; Lamba, D.; Pifferi, A.; Mande, S. C.; Sarma, D. D.; Sharma, S. M.; Paolucci, G. Status of the crystallography beamlines at Elettra. *The European Physical Journal Plus* **2015**, *130*, 43.
- [76] Bubert, H., Jenett, H., Eds. *Surface and Thin Film Analysis*; Wiley-VCH: Weinheim, 2002.
- [77] Soergel, E. Piezoresponse force microscopy (PFM). *Journal of Physics D: Applied Physics* **2011**, *44*, 464003.
- [78] Gruverman, A.; Kalinin, S. V. Piezoresponse force microscopy and recent advances in nanoscale studies of ferroelectrics. *Journal of Materials Science* **2006**, *41*, 107–116.
- [79] Curie, J.; Curie, P. Développement par compression de l'électricité polaire dans les cristaux hémihédres à faces inclinées. *Bulletin de la Société minéralogique de France* **1880**, *3*, 90–93.
- [80] Arnau Vives, A., Ed. *Piezoelectric Transducers and Applications*; Springer: Berlin, Heidelberg, 2008.
- [81] Tynell, T.; Karppinen, M. Atomic layer deposition of ZnO: a review. *Semiconductor Science and Technology* **2014**, *29*, 043001.
- [82] Law, M.; Greene, L. E.; Johnson, J. C.; Saykally, R.; Yang, P. Nanowire dye-sensitized solar cells. *Nature Materials* **2005**, *4*, 455–459.
- [83] Hau, S. K.; Yip, H.-L.; Baek, N. S.; Zou, J.; O'Malley, K.; Jen, A. K.-Y. Air-stable inverted flexible polymer solar cells using zinc oxide nanoparticles as an electron selective layer. *Applied Physics Letters* **2008**, *92*, 253301.
- [84] Beek, W. J. E.; Wienk, M. M.; Janssen, R. A. J. Efficient Hybrid Solar Cells from Zinc Oxide Nanoparticles and a Conjugated Polymer. *Advanced Materials* **2004**, *16*, 1009–1013.
- [85] Jiang, X.; Wong, F. L.; Fung, M. K.; Lee, S. T. Aluminum-doped zinc oxide films as transparent conductive electrode for organic light-emitting devices. *Applied Physics Letters* **2003**, *83*, 1875–1877.
- [86] Ellmer, K. Magnetron sputtering of transparent conductive zinc oxide: relation between the sputtering parameters and the electronic properties. *Journal of Physics D: Applied Physics* **2000**, *33*, R17–R32.

- [87] Kim, H.; Gilmore, C. M.; Horwitz, J. S.; Piqué, A.; Murata, H.; Kushto, G. P.; Schlaf, R.; Kafafi, Z. H.; Chrisey, D. B. Transparent conducting aluminum-doped zinc oxide thin films for organic light-emitting devices. *Applied Physics Letters* **2000**, *76*, 259–261.
- [88] Alam, M. J.; Cameron, D. C. Preparation and properties of transparent conductive aluminum-doped zinc oxide thin films by sol–gel process. *Journal of Vacuum Science & Technology A: Vacuum, Surfaces, and Films* **2001**, *19*, 1642–1646.
- [89] Khan, A.; Ali Abbasi, M.; Hussain, M.; Hussain Ibupoto, Z.; Wissting, J.; Nur, O.; Willander, M. Piezoelectric nanogenerator based on zinc oxide nanorods grown on textile cotton fabric. *Applied Physics Letters* **2012**, *101*, 193506.
- [90] Zhu, G.; Yang, R.; Wang, S.; Wang, Z. L. Flexible High-Output Nanogenerator Based on Lateral ZnO Nanowire Array. *Nano Letters* **2010**, *10*, 3151–3155.
- [91] Manekkathodi, A.; Lu, M.-Y.; Wang, C. W.; Chen, L.-J. Direct Growth of Aligned Zinc Oxide Nanorods on Paper Substrates for Low-Cost Flexible Electronics. *Advanced Materials* **2010**, *22*, 4059–4063.
- [92] Wang, C.; Yin, L.; Zhang, L.; Xiang, D.; Gao, R. Metal Oxide Gas Sensors: Sensitivity and Influencing Factors. *Sensors* **2010**, *10*, 2088–2106.
- [93] Pung, S.-Y.; Choy, K.-L.; Hou, X.; Shan, C. Preferential growth of ZnO thin films by the atomic layer deposition technique. *Nanotechnology* **2008**, *19*, 435609.
- [94] Singh, S. P.; Arya, S. K.; Pandey, P.; Malhotra, B. D.; Saha, S.; Sreenivas, K.; Gupta, V. Cholesterol biosensor based on rf sputtered zinc oxide nanoporous thin film. *Applied Physics Letters* **2007**, *91*, 063901.
- [95] Xu, H.; Liu, X.; Cui, D.; Li, M.; Jiang, M. A novel method for improving the performance of ZnO gas sensors. *Sensors and Actuators B: Chemical* **2006**, *114*, 301–307.
- [96] Xu, J.; Pan, Q.; Shun, Y.; Tian, Z. Grain size control and gas sensing properties of ZnO gas sensor. *Sensors and Actuators B: Chemical* **2000**, *66*, 277–279.
- [97] Park, S.-H. K.; Oh, J.; Hwang, C.-S.; Lee, J.-I.; Yang, Y. S.; Chu, H. Y. Ultrathin Film Encapsulation of an OLED by ALD. *Electrochemical and Solid-State Letters* **2005**, *8*, H21.
- [98] Langereis, E.; Creatore, M.; Heil, S. B. S.; van de Sanden, M. C. M.; Kessels, W. M. M. Plasma-assisted atomic layer deposition of Al₂O₃ moisture permeation barriers on polymers. *Applied Physics Letters* **2006**, *89*, 081915.

- [99] Knez, M.; Kadri, A.; Wege, C.; Gösele, U.; Jeske, H.; Nielsch, K. Atomic Layer Deposition on Biological Macromolecules: Metal Oxide Coating of Tobacco Mosaic Virus and Ferritin. *Nano Letters* **2006**, *6*, 1172–1177.
- [100] Hyde, G. K.; McCullen, S. D.; Jeon, S.; Stewart, S. M.; Jeon, H.; Lobo, E. G.; Parsons, G. N. Atomic layer deposition and biocompatibility of titanium nitride nano-coatings on cellulose fiber substrates. *Biomedical Materials* **2009**, *4*, 25001.
- [101] Fortunato, E. M.; Barquinha, P. M.; Pimentel, A. C.; Gonçalves, A. M.; Marques, A. J.; Martins, R. F.; Pereira, L. M. Wide-bandgap high-mobility ZnO thin-film transistors produced at room temperature. *Applied Physics Letters* **2004**, *85*, 2541–2543.
- [102] Singh, A. V.; Mehra, R. M.; Buthrath, N.; Wakahara, A.; Yoshida, A. Highly conductive and transparent aluminum-doped zinc oxide thin films prepared by pulsed laser deposition in oxygen ambient. *Journal of Applied Physics* **2001**, *90*, 5661–5665.
- [103] Kawamura, Y.; Hattori, N.; Miyatake, N.; Horita, M.; Uraoka, Y. ZnO Thin Films Fabricated by Plasma-Assisted Atomic Layer Deposition. *Japanese Journal of Applied Physics* **2011**, *50*, 04DF05.
- [104] Kim, D.; Kang, H.; Kim, J.-M.; Kim, H. The properties of plasma-enhanced atomic layer deposition (ALD) ZnO thin films and comparison with thermal ALD. *Applied Surface Science* **2011**, *257*, 3776–3779.
- [105] Jin, M.-j.; Jo, J.; Neupane, G. P.; Kim, J.; An, K.-S.; Yoo, J.-W. Tuning of undoped ZnO thin film via plasma enhanced atomic layer deposition and its application for an inverted polymer solar cell. *AIP Advances* **2013**, *3*, 102114.
- [106] Zhang, J.; Yang, H.; Zhang, Q.-l.; Dong, S.; Luo, J. Structural, optical, electrical and resistive switching properties of ZnO thin films deposited by thermal and plasma-enhanced atomic layer deposition. *Applied Surface Science* **2013**, *282*, 390–395.
- [107] Park, S.-H. K.; Hwang, C.-S.; Kwack, H.-S.; Lee, J.-H.; Chu, H. Y. Characteristics of ZnO Thin Films by Means of Plasma-Enhanced Atomic Layer Deposition. *Electrochemical and Solid-State Letters* **2006**, *9*, G299.
- [108] Sultan, S.; Clark, O.; Masaud, T.; Fang, Q.; Gunn, R.; Hakim, M.; Sun, K.; Ashburn, P.; Chong, H. Remote plasma enhanced atomic layer deposition of ZnO for thin film electronic applications. *Microelectronic Engineering* **2012**, *97*, 162–165.
- [109] Muneshwar, T.; Shoute, G.; Barlage, D.; Cadien, K. Plasma enhanced atomic layer deposition of ZnO with diethyl zinc and oxygen plasma: Effect of precursor decomposition. *Journal of Vacuum Science & Technology A: Vacuum, Surfaces, and Films* **2016**, *34*, 50605.

- [110] Rowlette, P. C.; Allen, C. G.; Bromley, O. B.; Dubetz, A. E.; Wolden, C. A. Plasma-Enhanced Atomic Layer Deposition of Semiconductor Grade ZnO Using Dimethyl Zinc. *Chemical Vapor Deposition* **2009**, *15*, 15–20.
- [111] Malm, J.; Sahramo, E.; Perälä, J.; Sajavaara, T.; Karppinen, M. Low-temperature atomic layer deposition of ZnO thin films: Control of crystallinity and orientation. *Thin Solid Films* **2011**, *519*, 5319–5322.
- [112] Thomas, M. A.; Cui, J. B. Highly Tunable Electrical Properties in Undoped ZnO Grown by Plasma Enhanced Thermal-Atomic Layer Deposition. *ACS Applied Materials & Interfaces* **2012**, *4*, 3122–3128.
- [113] Kwon, J.-D.; Lee, J.-W.; Nam, K.-S.; Kim, D.-H.; Jeong, Y.; Kwon, S.-H.; Park, J.-S. The impact on in-situ-hydrogen-plasma treatment for zinc oxide plasma enhanced atomic layer deposition. *Current Applied Physics* **2012**, *12*, S134–S138.
- [114] Mammadov, E.; Naghavi, N.; Jehl, Z.; Renou, G.; Tiwald, T.; Mamedov, N.; Lincot, D.; Guillemoles, J.-F. Dielectric function of zinc oxide thin films in a broad spectral range. *Thin Solid Films* **2014**, *571*, 593–596.
- [115] Knoops, H. C. M.; van de Loo, B. W. H.; Smit, S.; Ponomarev, M. V.; Weber, J.-W.; Sharma, K.; Kessels, W. M. M.; Creatore, M. Optical modeling of plasma-deposited ZnO films: Electron scattering at different length scales. *Journal of Vacuum Science & Technology A: Vacuum, Surfaces, and Films* **2015**, *33*, 021509.
- [116] Viezbicke, B. D.; Patel, S.; Davis, B. E.; Birnie, D. P. Evaluation of the Tauc method for optical absorption edge determination: ZnO thin films as a model system. *physica status solidi (b)* **2015**, *252*, 1700–1710.
- [117] Srikant, V.; Clarke, D. R. On the optical band gap of zinc oxide. *Journal of Applied Physics* **1998**, *83*, 5447–5451.
- [118] Kriegner, D.; Wintersberger, E.; Stangl, J. xrayutilities : a versatile tool for reciprocal space conversion of scattering data recorded with linear and area detectors. *Journal of Applied Crystallography* **2013**, *46*, 1162–1170.
- [119] Payne, B.; Biesinger, M.; McIntyre, N. X-ray photoelectron spectroscopy studies of reactions on chromium metal and chromium oxide surfaces. *Journal of Electron Spectroscopy and Related Phenomena* **2011**, *184*, 29–37.
- [120] Huang, R.; Sun, K.; Kiang, K. S.; Morgan, K. A.; de Groot, C. Forming-free resistive switching of tunable ZnO films grown by atomic layer deposition. *Microelectronic Engineering* **2016**, *161*, 7–12.

- [121] Guzewicz, E.; Godlewski, M.; Wachnicki, L.; Krajewski, T. A.; Luka, G.; Gieraltowska, S.; Jakiela, R.; Stonert, A.; Lisowski, W.; Krawczyk, M.; Sobczak, J. W.; Jablonski, A. ALD grown zinc oxide with controllable electrical properties. *Semiconductor Science and Technology* **2012**, *27*, 074011.
- [122] Jung, T.-H.; Park, J.-S.; Kim, D.-H.; Jeong, Y.; Park, S.-G.; Kwon, J.-D. Effect of in situ hydrogen plasma treatment on zinc oxide grown using low temperature atomic layer deposition. *Journal of Vacuum Science & Technology A: Vacuum, Surfaces, and Films* **2013**, *31*, 01A124.
- [123] Fan, J. C. C.; Goodenough, J. B. X-ray photoemission spectroscopy studies of Sn-doped indium-oxide films. *Journal of Applied Physics* **1977**, *48*, 3524–3531.
- [124] Pal, B.; Sharon, M. Enhanced photocatalytic activity of highly porous ZnO thin films prepared by sol–gel process. *Materials Chemistry and Physics* **2002**, *76*, 82–87.
- [125] Bond, W. L. Measurement of the refractive indices of several crystals. *Journal of Applied Physics* **1965**, *36*, 1674–1677.
- [126] Paraguay D., F.; Estrada L., W.; Acosta N., D.; Andrade, E.; Miki-Yoshida, M. Growth, structure and optical characterization of high quality ZnO thin films obtained by spray pyrolysis. *Thin Solid Films* **1999**, *350*, 192–202.
- [127] Yan, Z.; Zhou, X. Y.; Pang, G. K. H.; Zhang, T.; Liu, W. L.; Cheng, J. G.; Song, Z. T.; Feng, S. L.; Lai, L. H.; Chen, J. Z.; Wang, Y. ZnO-based film bulk acoustic resonator for high sensitivity biosensor applications. *Applied Physics Letters* **2007**, *90*, 143503.
- [128] Das, S. C.; Green, R. J.; Podder, J.; Regier, T. Z.; Chang, G. S.; Moewes, A. Band Gap Tuning in ZnO Through Ni Doping via Spray Pyrolysis. *The Journal of Physical Chemistry C* **2013**, *117*, 12745–12753.
- [129] Bhat, S. V.; Deepak, F. Tuning the bandgap of ZnO by substitution with Mn²⁺, Co²⁺ and Ni²⁺. *Solid State Communications* **2005**, *135*, 345–347.
- [130] Lee, D.-J.; Kim, H.-M.; Kwon, J.-Y.; Choi, H.; Kim, S.-H.; Kim, K.-B. Structural and Electrical Properties of Atomic Layer Deposited Al-Doped ZnO Films. *Advanced Functional Materials* **2011**, *21*, 448–455.
- [131] Chang, W.-Y.; Lai, Y.-C.; Wu, T.-B.; Wang, S.-F.; Chen, F.; Tsai, M.-J. Unipolar resistive switching characteristics of ZnO thin films for nonvolatile memory applications. *Applied Physics Letters* **2008**, *92*, 022110.
- [132] Kim, S.; Moon, H.; Gupta, D.; Yoo, S.; Choi, Y.-K. Resistive Switching Characteristics of Sol–Gel Zinc Oxide Films for Flexible Memory Applications. *IEEE Transactions on Electron Devices* **2009**, *56*, 696–699.

- [133] Wan, Q.; Li, Q. H.; Chen, Y. J.; Wang, T. H.; He, X. L.; Li, J. P.; Lin, C. L. Fabrication and ethanol sensing characteristics of ZnO nanowire gas sensors. *Applied Physics Letters* **2004**, *84*, 3654–3656.
- [134] Pilz, J.; Perrotta, A.; Christian, P.; Tazreiter, M.; Resel, R.; Leising, G.; Griesser, T.; Coclite, A. M. Tuning of material properties of ZnO thin films grown by plasma-enhanced atomic layer deposition at room temperature. *Journal of Vacuum Science & Technology A: Vacuum, Surfaces, and Films* **2018**, *36*, 01A109.
- [135] Nam, T.; Lee, C. W.; Kim, H. J.; Kim, H. Growth characteristics and properties of G-doped ZnO (GZO) thin films grown by thermal and plasma-enhanced atomic layer deposition. *Applied Surface Science* **2014**, *295*, 260–265.
- [136] Potts, S. E.; Keuning, W.; Langereis, E.; Dingemans, G.; van de Sanden, M. C. M.; Kessels, W. M. M. Low Temperature Plasma-Enhanced Atomic Layer Deposition of Metal Oxide Thin Films. *Journal of The Electrochemical Society* **2010**, *157*, P66.
- [137] Tang, Z. K.; Wong, G. K. L.; Yu, P.; Kawasaki, M.; Ohtomo, A.; Koinuma, H.; Segawa, Y. Room-temperature ultraviolet laser emission from self-assembled ZnO microcrystallite thin films. *Applied Physics Letters* **1998**, *72*, 3270–3272.
- [138] Abrahams, S. C.; Bernstein, J. L. Remeasurement of the structure of hexagonal ZnO. *Acta Crystallographica Section B Structural Crystallography and Crystal Chemistry* **1969**, *25*, 1233–1236.
- [139] Yousfi, E. B.; Fouache, J.; Lincot, D. Study of atomic layer epitaxy of zinc oxide by in-situ quartz crystal microgravimetry. *Applied Surface Science* **2000**, *153*, 223–234.
- [140] Jeon, S.; Bang, S.; Lee, S.; Kwon, S.; Jeong, W.; Jeon, H.; Chang, H. J.; Park, H.-H. Structural and Electrical Properties of ZnO Thin Films Deposited by Atomic Layer Deposition at Low Temperatures. *Journal of The Electrochemical Society* **2008**, *155*, H738.
- [141] Yuan, N.; Wang, S.; Tan, C.; Wang, X.; Chen, G.; Ding, J. The influence of deposition temperature on growth mode, optical and mechanical properties of ZnO films prepared by the ALD method. *Journal of Crystal Growth* **2013**, *366*, 43–46.
- [142] Gibaud, A.; Vignaud, G. *X-ray and Neutron Reflectivity*; Springer Berlin Heidelberg: Berlin, Heidelberg, Vol. 770; pp 85–131.
- [143] Jensen, J. M.; Oelkers, A. B.; Toivola, R.; Johnson, D. C.; Elam, J. W.; George, S. M. X-ray Reflectivity Characterization of ZnO/Al₂O₃ Multilayers Prepared by Atomic Layer Deposition. *Chemistry of Materials* **2002**, *14*, 2276–2282.

- [144] Liang, Z.; Zhang, Q.; Wiranwetchayan, O.; Xi, J.; Yang, Z.; Park, K.; Li, C.; Cao, G. Effects of the Morphology of a ZnO Buffer Layer on the Photovoltaic Performance of Inverted Polymer Solar Cells. *Advanced Functional Materials* **2012**, *22*, 2194–2201.
- [145] Muth, J. F.; Kolbas, R. M.; Sharma, A. K.; Oktyabrsky, S.; Narayan, J. Excitonic structure and absorption coefficient measurements of ZnO single crystal epitaxial films deposited by pulsed laser deposition. *Journal of Applied Physics* **1999**, *85*, 7884–7887.
- [146] Nandakumar, N.; Dielissen, B.; Garcia-Alonso, D.; Liu, Z.; Gortzen, R.; Kessels, W. M. M.; Aberle, A. G.; Hoex, B. Resistive Intrinsic ZnO Films Deposited by Ultrafast Spatial ALD for PV Applications. *IEEE Journal of Photovoltaics* **2015**, *5*, 1462–1469.
- [147] Chang, Y.-M.; Shieh, J.; Chu, P.-Y.; Lee, H.-Y.; Lin, C.-M.; Juang, J.-Y. Enhanced Free Exciton and Direct Band-Edge Emissions at Room Temperature in Ultrathin ZnO Films Grown on Si Nanopillars by Atomic Layer Deposition. *ACS Applied Materials & Interfaces* **2011**, *3*, 4415–4419.
- [148] Bagnall, D.; Chen, Y.; Shen, M.; Zhu, Z.; Goto, T.; Yao, T. Room temperature excitonic stimulated emission from zinc oxide epilayers grown by plasma-assisted MBE. *Journal of Crystal Growth* **1998**, *184-185*, 605–609.
- [149] Rai, R. C.; Guminiak, M.; Wilser, S.; Cai, B.; Nakarmi, M. L. Elevated temperature dependence of energy band gap of ZnO thin films grown by e-beam deposition. *Journal of Applied Physics* **2012**, *111*, 073511.
- [150] Tan, S.; Chen, B.; Sun, X.; Hu, X.; Zhang, X.; Chua, S. Properties of polycrystalline ZnO thin films by metal organic chemical vapor deposition. *Journal of Crystal Growth* **2005**, *281*, 571–576.
- [151] Lupan, O.; Pauporté, T.; Chow, L.; Viana, B.; Pellé, F.; Ono, L.; Roldan Cuenya, B.; Heinrich, H. Effects of annealing on properties of ZnO thin films prepared by electrochemical deposition in chloride medium. *Applied Surface Science* **2010**, *256*, 1895–1907.
- [152] Krajewski, T. A.; Terziyska, P.; Luka, G.; Lusakowska, E.; Jakiela, R.; Vlachov, E. S.; Guziewicz, E. Diversity of contributions leading to the nominally n-type behavior of ZnO films obtained by low temperature Atomic Layer Deposition. *Journal of Alloys and Compounds* **2017**, *727*, 902–911.
- [153] Krajewski, T. A.; Dybko, K.; Luka, G.; Guziewicz, E.; Nowakowski, P.; Witkowski, B. S.; Jakiela, R.; Wachnicki, L.; Kaminska, A.; Suchocki, A.; Godlewski, M. Dominant shallow donors in zinc oxide layers obtained by low-temperature atomic layer deposition: Electrical and optical investigations. *Acta Materialia* **2014**, *65*, 69–75.

- [154] Gardeniers, J. G. E.; Rittersma, Z. M.; Burger, G. J. Preferred orientation and piezoelectricity in sputtered ZnO films. *Journal of Applied Physics* **1998**, *83*, 7844–7854.
- [155] Yu, X.; Marks, T. J.; Facchetti, A. Metal oxides for optoelectronic applications. *Nature Materials* **2016**, *15*, 383–396.
- [156] Klingshirn, C.; Fallert, J.; Zhou, H.; Sartor, J.; Thiele, C.; Maier-Flaig, F.; Schneider, D.; Kalt, H. 65 years of ZnO research - old and very recent results. *physica status solidi (b)* **2010**, *247*, 1424–1447.
- [157] Arya, S. K.; Saha, S.; Ramirez-Vick, J. E.; Gupta, V.; Bhansali, S.; Singh, S. P. Recent advances in ZnO nanostructures and thin films for biosensor applications: Review. *Analytica Chimica Acta* **2012**, *737*, 1–21.
- [158] Cachoncinlle, C.; Hebert, C.; Perrière, J.; Nistor, M.; Petit, A.; Millon, E. Random lasing of ZnO thin films grown by pulsed-laser deposition. *Applied Surface Science* **2015**, *336*, 103–107.
- [159] Wu, Y.; Hermkens, P. M.; van de Loo, B. W. H.; Knoop, H. C. M.; Potts, S. E.; Verheijen, M. A.; Roozeboom, F.; Kessels, W. M. M. Electrical transport and Al doping efficiency in nanoscale ZnO films prepared by atomic layer deposition. *Journal of Applied Physics* **2013**, *114*, 024308.
- [160] Horwat, D.; Mickan, M.; Chamorro, W. New strategies for the synthesis of ZnO and Al-doped ZnO films by reactive magnetron sputtering at room temperature. *physica status solidi (c)* **2016**, *13*, 951–957.
- [161] Wisz, G.; Virt, I.; Sagan, P.; Potera, P.; Yavorskyi, R. Structural, Optical and Electrical Properties of Zinc Oxide Layers Produced by Pulsed Laser Deposition Method. *Nanoscale Research Letters* **2017**, *12*, 253.
- [162] Baitimirova, M. et al. Tuning of Structural and Optical Properties of Graphene/ZnO Nanolaminates. *The Journal of Physical Chemistry C* **2016**, *120*, 23716–23725.
- [163] Graniel, O.; Weber, M.; Balme, S.; Miele, P.; Bechelany, M. Atomic layer deposition for biosensing applications. *Biosensors and Bioelectronics* **2018**, *122*, 147–159.
- [164] Abou Chaaya, A.; Viter, R.; Bechelany, M.; Alute, Z.; Erts, D.; Zalesskaya, A.; Kovalevskis, K.; Rouessac, V.; Smyntyna, V.; Miele, P. Evolution of microstructure and related optical properties of ZnO grown by atomic layer deposition. *Beilstein Journal of Nanotechnology* **2013**, *4*, 690–698.
- [165] Oruc, F. B.; Aygun, L. E.; Donmez, I.; Biyikli, N.; Okyay, A. K.; Yu, H. Y. Low temperature atomic layer deposited ZnO photo thin film transistors. *Journal of Vacuum Science & Technology A: Vacuum, Surfaces, and Films* **2015**, *33*, 01A105.

- [166] Tereshchenko, A.; Bechelany, M.; Viter, R.; Khranovskyy, V.; Smyntyna, V.; Starodub, N.; Yakimova, R. Optical biosensors based on ZnO nanostructures: advantages and perspectives. A review. *Sensors and Actuators B: Chemical* **2016**, *229*, 664–677.
- [167] Thomas, M. A.; Cui, J. The Effects of an O₂ Plasma on the Optical Properties of Atomic Layer Deposited ZnO. *ECS Transactions* **2012**, *45*, 87–95.
- [168] Fong, D. D.; Eastman, J. A.; Kim, S. K.; Fister, T. T.; Highland, M. J.; Baldo, P. M.; Fuoss, P. H. In situ synchrotron x-ray characterization of ZnO atomic layer deposition. *Applied Physics Letters* **2010**, *97*, 191904.
- [169] Baji, Z.; Lábadi, Z.; Horváth, Z. E.; Molnár, G.; Volk, J.; Bársony, I.; Barna, P. Nucleation and Growth Modes of ALD ZnO. *Crystal Growth & Design* **2012**, *12*, 5615–5620.
- [170] Klug, J. A.; Weimer, M. S.; Emery, J. D.; Yanguas-Gil, A.; Seifert, S.; Schlepütz, C. M.; Martinson, A. B. F.; Elam, J. W.; Hock, A. S.; Proslie, T. A modular reactor design for in situ synchrotron x-ray investigation of atomic layer deposition processes. *Review of Scientific Instruments* **2015**, *86*, 113901.
- [171] Boichot, R. et al. Evolution of Crystal Structure During the Initial Stages of ZnO Atomic Layer Deposition. *Chemistry of Materials* **2016**, *28*, 592–600.
- [172] Chu, M. H.; Tian, L.; Chaker, A.; Cantelli, V.; Ouled, T.; Boichot, R.; Crisci, A.; Lay, S.; Richard, M.-I.; Thomas, O.; Deschanvres, J.-L.; Renevier, H.; Fong, D. D.; Ciatto, G. An Atomistic View of the Incipient Growth of Zinc Oxide Nanolayers. *Crystal Growth & Design* **2016**, *16*, 5339–5348.
- [173] Chu, M.-H.; Tian, L.; Chaker, A.; Skopin, E.; Cantelli, V.; Ouled, T.; Boichot, R. L.; Crisci, A.; Lay, S.; Richard, M.-I.; Thomas, O.; Deschanvres, J.-L.; Renevier, H.; Fong, D.; Ciatto, G. Evaluation of Alternative Atomistic Models for the Incipient Growth of ZnO by Atomic Layer Deposition. *Journal of Electronic Materials* **2017**, *46*, 3512–3517.
- [174] Skopin, E. V.; Rapenne, L.; Roussel, H.; Deschanvres, J.-L.; Blanquet, E.; Ciatto, G.; Fong, D. D.; Richard, M.-I.; Renevier, H. The initial stages of ZnO atomic layer deposition on atomically flat In_{0.53}Ga_{0.47}As substrates. *Nanoscale* **2018**, *10*, 11585–11596.
- [175] Skopin, E. V.; Deschanvres, J.-L.; Renevier, H. In Situ Ellipsometry Study of the Early Stage of ZnO Atomic Layer Deposition on In_{0.53}Ga_{0.47}As. *physica status solidi (a)* **2020**, 1900831.

- [176] Liao, M.-H.; Chang, L. C. Experimental demonstration for the implant-free In_{0.53}Ga_{0.47}As quantum-well metal-insulator-semiconductor field-effect transistors with ultra-low source/drain resistance. *Applied Physics Letters* **2013**, *103*, 072102.
- [177] Kim, S. H.; Joo, S. Y.; Jin, H. S.; Kim, W.-B.; Park, T. J. Ultrathin ZnS and ZnO Interfacial Passivation Layers for Atomic-Layer-Deposited HfO₂ Films on InP Substrates. *ACS Applied Materials & Interfaces* **2016**, *8*, 20880–20884.
- [178] Langereis, E.; Heil, S. B. S.; van de Sanden, M. C. M.; Kessels, W. M. M. In situ spectroscopic ellipsometry study on the growth of ultrathin TiN films by plasma-assisted atomic layer deposition. *Journal of Applied Physics* **2006**, *100*, 023534.
- [179] Dendooven, J.; Solano, E.; Minjauw, M. M.; Van de Kerckhove, K.; Coati, A.; Fonda, E.; Portale, G.; Garreau, Y.; Detavernier, C. Mobile setup for synchrotron based in situ characterization during thermal and plasma-enhanced atomic layer deposition. *Review of Scientific Instruments* **2016**, *87*, 113905.
- [180] Danauskas, S. M.; Li, D.; Meron, M.; Lin, B.; Lee, K. Y. C. Stochastic fitting of specular X-ray reflectivity data using StochFit. *Journal of Applied Crystallography* **2008**, *41*, 1187–1193.
- [181] Lausi, A.; Polentarutti, M.; Onesti, S.; Plaisier, J. R.; Busetto, E.; Bais, G.; Barba, L.; Cassetta, A.; Campi, G.; Lamba, D.; Pifferi, A.; Mande, S. C.; Sarma, D. D.; Sharma, S. M.; Paolucci, G. Status of the crystallography beamlines at Elettra. *The European Physical Journal Plus* **2015**, *130*, 43.
- [182] Schrode, B.; Pachmajer, S.; Dohr, M.; Röthel, C.; Domke, J.; Fritz, T.; Resel, R.; Werzer, O. GIDVis : a comprehensive software tool for geometry-independent grazing-incidence X-ray diffraction data analysis and pole-figure calculations. *Journal of Applied Crystallography* **2019**, *52*, 683–689.
- [183] Nečas, D.; Klapetek, P. Gwyddion: an open-source software for SPM data analysis. *Open Physics* **2012**, *10*, 181–188.
- [184] Kim, S.-W.; Peng, L.; Miller, A.; Beyer, G.; Beyne, E.; Lee, C.-S. Permanent wafer bonding in the low temperature by using various plasma enhanced chemical vapour deposition dielectrics. 2015 International 3D Systems Integration Conference (3DIC). 2015; pp TS7.2.1–TS7.2.4.
- [185] Van Bui, H.; Wiggers, F. B.; Gupta, A.; Nguyen, M. D.; Aarnink, A. A. I.; de Jong, M. P.; Kovalgin, A. Y. Initial growth, refractive index, and crystallinity of thermal and plasma-enhanced atomic layer deposition AlN films. *Journal of Vacuum Science & Technology A: Vacuum, Surfaces, and Films* **2015**, *33*, 01A111.

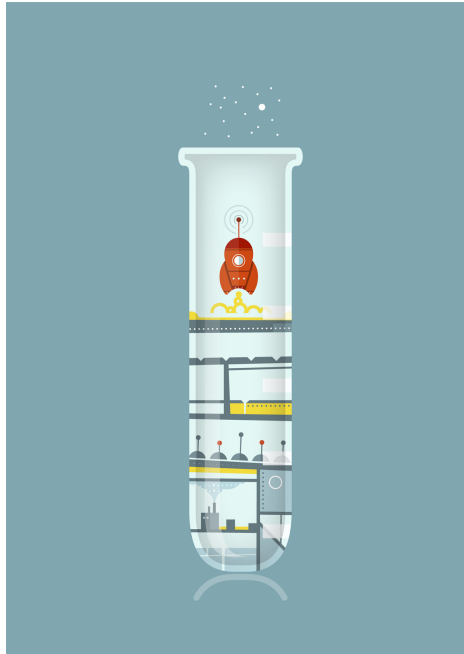
- [186] Napari, M.; Lahtinen, M.; Veselov, A.; Julin, J.; Østreg, E.; Sajavaara, T. Room-temperature plasma-enhanced atomic layer deposition of ZnO: Film growth dependence on the PEALD reactor configuration. *Surface and Coatings Technology* **2017**, *326*, 281–290.
- [187] Koch, M. H.; Hartmann, A. J.; Lamb, R. N.; Neuber, M.; Grunze, M. Self-Texture in the Initial Stages of ZnO Film Growth. *The Journal of Physical Chemistry B* **1997**, *101*, 8231–8236.
- [188] Kajikawa, Y. Texture development of non-epitaxial polycrystalline ZnO films. *Journal of Crystal Growth* **2006**, *289*, 387–394.
- [189] Huang, H.-W.; Chang, W.-C.; Lin, S.-J.; Chueh, Y.-L. Growth of controllable ZnO film by atomic layer deposition technique via inductively coupled plasma treatment. *Journal of Applied Physics* **2012**, *112*, 124102.
- [190] Lu, Y.; Emanetoglu, N. W.; Chen, Y. *Zinc Oxide Bulk, Thin Films and Nanostructures*; Elsevier: Amsterdam, 2006; pp 443–489.
- [191] Park, K.; Lee, D.-K.; Kim, B.-S.; Jeon, H.; Lee, N.-E.; Whang, D.; Lee, H.-J.; Kim, Y. J.; Ahn, J.-H. Stretchable, Transparent Zinc Oxide Thin Film Transistors. *Advanced Functional Materials* **2010**, *20*, 3577–3582.
- [192] Liang, H. K.; Yu, S. F.; Yang, H. Y. ZnO random laser diode arrays for stable single-mode operation at high power. *Applied Physics Letters* **2010**, *97*, 241107.
- [193] Hsiao, C.-C.; Huang, K.-Y.; Hu, Y.-C. Fabrication of a ZnO Pyroelectric Sensor. *Sensors* **2008**, *8*, 185–192.
- [194] Chen, J.; He, X.; Wang, W.; Xuan, W.; Zhou, J.; Wang, X.; Dong, S. R.; Garner, S.; Cimo, P.; Luo, J. K. Bendable transparent ZnO thin film surface acoustic wave strain sensors on ultra-thin flexible glass substrates. *J. Mater. Chem. C* **2014**, *2*, 9109–9114.
- [195] Bdikin, I. K.; Gracio, J.; Ayouchi, R.; Schwarz, R.; Kholkin, A. L. Local piezoelectric properties of ZnO thin films prepared by RF-plasma-assisted pulsed-laser deposition method. *Nanotechnology* **2010**, *21*, 235703.
- [196] D'Agostino, D.; Di Giorgio, C.; Di Trolio, A.; Guarino, A.; Cucolo, A. M.; Vecchione, A.; Bobba, F. Piezoelectricity and charge trapping in ZnO and Co-doped ZnO thin films. *AIP Advances* **2017**, *7*, 055010.
- [197] Qin, W.; Li, T.; Li, Y.; Qiu, J.; Ma, X.; Chen, X.; Hu, X.; Zhang, W. A high power ZnO thin film piezoelectric generator. *Applied Surface Science* **2016**, *364*, 670–675.

- [198] Laurenti, M.; Stassi, S.; Lorenzoni, M.; Fontana, M.; Canavese, G.; Cauda, V.; Pirri, C. F. Evaluation of the piezoelectric properties and voltage generation of flexible zinc oxide thin films. *Nanotechnology* **2015**, *26*, 215704.
- [199] Yang, Y. C.; Song, C.; Wang, X. H.; Zeng, F.; Pan, F. Giant piezoelectric d_{33} coefficient in ferroelectric vanadium doped ZnO films. *Applied Physics Letters* **2008**, *92*, 012907.
- [200] Kratzer, M.; Lasnik, M.; Röhrig, S.; Teichert, C.; Deluca, M. Reconstruction of the domain orientation distribution function of polycrystalline PZT ceramics using vector piezoresponse force microscopy. *Scientific Reports* **2018**, *8*, 422.
- [201] Kolosov, O. Kolosov Replies. *Physical Review Letters* **1996**, *76*, 4292–4292.
- [202] Blagoev, B. S.; Aleksandrova, M.; Terziyska, P.; Tzvetkov, P.; Kovacheva, D.; Kolev, G.; Mehandzhiev, V.; Denishev, K.; Dimitrov, D. Investigation of the structural, optical and piezoelectric properties of ALD ZnO films on PEN substrates. *Journal of Physics: Conference Series* **2018**, *992*, 012027.
- [203] Liu, B.; Wang, M.; Chen, M.; Wang, J.; Liu, J.; Hu, D.; Liu, S.; Yao, X.; Yang, H. Effect of TC(002) on the Output Current of a ZnO Thin-Film Nanogenerator and a New Piezoelectricity Mechanism at the Atomic Level. *ACS Applied Materials & Interfaces* **2019**, *11*, 12656–12665.
- [204] Blumenstein, N. J.; Streb, F.; Walheim, S.; Schimmel, T.; Burghard, Z.; Bill, J. Template-controlled piezoactivity of ZnO thin films grown via a bioinspired approach. *Beilstein Journal of Nanotechnology* **2017**, *8*, 296–303.
- [205] Kang, S. J.; Joung, Y. H. Influence of substrate temperature on the optical and piezoelectric properties of ZnO thin films deposited by rf magnetron sputtering. *Applied Surface Science* **2007**, *253*, 7330–7335.
- [206] Park, S.; Kim, H.; Vosgueritchian, M.; Cheon, S.; Kim, H.; Koo, J. H.; Kim, T. R.; Lee, S.; Schwartz, G.; Chang, H.; Bao, Z. Stretchable Energy-Harvesting Tactile Electronic Skin Capable of Differentiating Multiple Mechanical Stimuli Modes. *Advanced Materials* **2014**, *26*, 7324–7332.
- [207] Yan, X.; Ren, W.; Xin, H.; Shi, P.; Chen, X.; Wu, X. Influence of substrate deformation on piezoelectric displacement measurement of piezoelectric film. *Ceramics International* **2013**, *39*, S583–S586.
- [208] Leighton, G. J. T.; Huang, Z. Accurate measurement of the piezoelectric coefficient of thin films by eliminating the substrate bending effect using spatial scanning laser vibrometry. *Smart Materials and Structures* **2010**, *19*, 065011.

- [209] Rodriguez, B. J.; Callahan, C.; Kalinin, S. V.; Proksch, R. Dual-frequency resonance-tracking atomic force microscopy. *Nanotechnology* **2007**, *18*, 475504.
- [210] Morton, M. *Rubber Technology*, 3rd ed.; Van Nostrand Reinhold Company Inc: New York, 1987.
- [211] Roy, K.; Debnath, S. C.; Potiyaraj, P. A critical review on the utilization of various reinforcement modifiers in filled rubber composites. *Journal of Elastomers & Plastics* **2020**, *52*, 167–193.
- [212] Mostoni, S.; Milana, P.; Credico, B. D.; D'Arienzo, M.; Scotti, R. Zinc-Based Curing Activators: New Trends for Reducing Zinc Content in Rubber Vulcanization Process. *Catalysts* **2019**, *9*, 664.
- [213] Heideman, G.; Datta, R. N.; Noordermeer, J. W. M.; van Baarle, B. Influence of zinc oxide during different stages of sulfur vulcanization. Elucidated by model compound studies. *Journal of Applied Polymer Science* **2005**, *95*, 1388–1404.
- [214] Knite, M.; Teteris, V.; Kiploka, A.; Kaupuzs, J. Polyisoprene-carbon black nanocomposites as tensile strain and pressure sensor materials. *Sensors and Actuators A: Physical* **2004**, *110*, 142–149.
- [215] Ikeda, Y.; Kohjiya, S. In situ formed silica particles in rubber vulcanizate by the sol-gel method. *Polymer* **1997**, *38*, 4417–4423.
- [216] Raman, V. S.; Das, A.; Stöckelhuber, K. W.; Eshwaran, S. B.; Chanda, J.; Malanin, M.; Reuter, U.; Leuteritz, A.; Boldt, R.; Wießner, S.; Heinrich, G. Improvement of mechanical performance of solution styrene butadiene rubber by controlling the concentration and the size of in situ derived sol-gel silica particles. *RSC Advances* **2016**, *6*, 33643–33655.
- [217] McGuinness, E. K.; Leng, C. Z.; Losego, M. D. Increased Chemical Stability of Vapor-Phase Infiltrated AlO_x-Poly(methyl methacrylate) Hybrid Materials. *ACS Applied Polymer Materials* **2020**, *2*, 1335–1344.
- [218] Padbury, R. P.; Jur, J. S. Temperature-Dependent Infiltration of Polymers during Sequential Exposures to Trimethylaluminum. *Langmuir* **2014**, *30*, 9228–9238.
- [219] Akyildiz, H. I.; Padbury, R. P.; Parsons, G. N.; Jur, J. S. Temperature and Exposure Dependence of Hybrid Organic-Inorganic Layer Formation by Sequential Vapor Infiltration into Polymer Fibers. *Langmuir* **2012**, *28*, 15697–15704.
- [220] Wang, W.; Yang, F.; Chen, C.; Zhang, L.; Qin, Y.; Knez, M. Tuning the Conductivity of Polyaniline through Doping by Means of Single Precursor Vapor Phase Infiltration. *Advanced Materials Interfaces* **2017**, *4*, 1600806.

- [221] Yi, D. H.; Nam, C.-Y.; Doerk, G.; Black, C. T.; Grubbs, R. B. Infiltration Synthesis of Diverse Metal Oxide Nanostructures from Epoxidized Diene–Styrene Block Copolymer Templates. *ACS Applied Polymer Materials* **2019**, *1*, 672–683.
- [222] Burfield, D. R.; Lim, K. L. Differential scanning calorimetry analysis of natural rubber and related polyisoprenes. Measurement of the glass transition temperature. *Macromolecules* **1983**, *16*, 1170–1175.
- [223] dos Santos, K.; Suarez, P.; Rubim, J. Photo-degradation of synthetic and natural polyisoprenes at specific UV radiations. *Polymer Degradation and Stability* **2005**, *90*, 34–43.
- [224] Saunders, R. A.; Smith, D. C. Infra-Red Spectra and Structure of Hevea and Gutta Elastomers. *Journal of Applied Physics* **1949**, *20*, 953–965.
- [225] Colin, X.; Audouin, L.; Verdu, J. Kinetic modelling of the thermal oxidation of polyisoprene elastomers. Part 1: Unvulcanized unstabilized polyisoprene. *Polymer Degradation and Stability* **2007**, *92*, 886–897.
- [226] Morand, J. L. Chain Scission in the Oxidation of Polyisoprene. *Rubber Chemistry and Technology* **1977**, *50*, 373–396.
- [227] Zaghdoudi, M.; Kömmling, A.; Jaunich, M.; Wolff, D. Scission, Cross-Linking, and Physical Relaxation during Thermal Degradation of Elastomers. *Polymers* **2019**, *11*, 1280.
- [228] Sato, T.; Sakota, K.; Egami, M.; Shirano, K.; Okaya, T. Oxidation behavior of isoprene polymers and butadiene polymers. *Journal of Applied Polymer Science* **1977**, *21*, 981–988.
- [229] Li, G.-Y.; Koenig, J. L. A Review of Rubber Oxidation. *Rubber Chemistry and Technology* **2005**, *78*, 355–390.
- [230] Li, Y.; Kröger, M.; Liu, W. K. Primitive chain network study on uncrosslinked and crosslinked cis-polyisoprene polymers. *Polymer* **2011**, *52*, 5867–5878.
- [231] Van Amerongen, G. J. Influence of Structure of Elastomers on Their Permeability to Gases. *Rubber Chemistry and Technology* **1951**, *24*, 109–131.
- [232] Cianci, E.; Nazzari, D.; Seguini, G.; Perego, M. Trimethylaluminum Diffusion in PMMA Thin Films during Sequential Infiltration Synthesis: In Situ Dynamic Spectroscopic Ellipsometric Investigation. *Advanced Materials Interfaces* **2018**, *5*, 1801016.

- [233] Xie, W.; Khan, S.; Rojas, O. J.; Parsons, G. N. Control of Micro- and Mesopores in Carbon Nanofibers and Hollow Carbon Nanofibers Derived from Cellulose Diacetate via Vapor Phase Infiltration of Diethyl Zinc. *ACS Sustainable Chemistry & Engineering* **2018**, *6*, 13844–13853.
- [234] Hill, G. T.; Lee, D. T.; Williams, P. S.; Needham, C. D.; Dandley, E. C.; Oldham, C. J.; Parsons, G. N. Insight on the Sequential Vapor Infiltration Mechanisms of Trimethylaluminum with Poly(methyl methacrylate), Poly(vinylpyrrolidone), and Poly(acrylic acid). *The Journal of Physical Chemistry C* **2019**, *123*, 16146–16152.
- [235] Dandley, E. C.; Needham, C. D.; Williams, P. S.; Brozena, A. H.; Oldham, C. J.; Parsons, G. N. Temperature-dependent reaction between trimethylaluminum and poly(methyl methacrylate) during sequential vapor infiltration: experimental and ab initio analysis. *J. Mater. Chem. C* **2014**, *2*, 9416–9424.



THIS THESIS WAS TYPESET using \LaTeX , originally developed by Leslie Lamport and based on Donald Knuth's \TeX . The body text is set in 11 point Egenolff-Berner Garamond, a revival of Claude Garamont's humanist typeface. The above illustration, *Science Experiment 02*, was created by Ben Schlitter and released under CC BY-NC-ND 3.0. A template that can be used to format a PhD dissertation with this look & feel has been released under the permissive AGPL license, and can be found online at github.com/suchow/Dissertate or from its lead author, Jordan Suchow, at suchow@post.harvard.edu.